



**Universitat Autònoma
de Barcelona**

DOCTORAL THESIS

**Design and development of a
self-powered electrochromic biosensor**

Miguel Aller Pellitero

Supervised by

Dr. FRANCISCO JAVIER DEL CAMPO GARCÍA

Tutored by

Prof. ILUMINADA GALLARDO GARCÍA

Department of Chemistry

Faculty of Science

PhD in Electrochemistry. Science and Technology

March, 2019



Dr. Francisco Javier del Campo García, Tenured Scientist at Instituto de Microelectrónica de Barcelona IMB-CNM (CSIC), and Prof. Iluminada Gallardo García, Professor at Universitat Autònoma de Barcelona, certify that the thesis entitled *Design and development of a self-powered electrochromic biosensor* was carried out under their supervision within the IMB-CNM (CSIC).

Dr. Fco. Javier del Campo García
(Supervisor)

Prof. Iluminada Gallardo García
(Tutor)

Bellaterra, March 2019

A los que sin
estar, están

Acknowledgements

Hace cuatro años salía de Asturias con un objetivo, y tras este tiempo ha habido muchas personas que me han ayudado en este camino y a las que me gustaría agradecerse.

En primer lugar, por supuesto, a mi director Javier del Campo. Sinceramente, no encuentro palabras de agradecimiento que hagan justicia a lo mucho que me has ayudado, lo mucho que he aprendido y lo bien que me lo he pasado estos años trabajando junto a ti. Creo que una de las cosas que más voy a echar de menos son esas habituales largas conversaciones en el despacho en las que se nos ocurrían muchas ideas locas, otras no tanto, y que siempre acababan igual, con los dos lamentándonos de no tener recursos para llevarlas a cabo.

Agradecer también a toda esa gente que ha ayudado directamente con su trabajo a sacar adelante esta tesis. Jean-Yves, Boris y todos los fantásticos estudiantes que han venido desde Besançon. Maria, con quien compartí mis dos primeros años en el CNM. Gonzalo, Sara y toda esa gente de la UAB con la que he compartido nuestras reuniones semanales y a la que he molestado en mis diversas visitas a sus laboratorios. Ignasi (Inkzar), Quim (Arista SG), Fernando (Paymsar) y Francesc (Quimóvil), porque su ayuda y sus consejos estos dos últimos años nos ha dado un empujón clave para avanzar con el proyecto.

Por supuesto, a la gente del CNM. No puedo nombraros a todos porque, por suerte, sois demasiada la gente de la que me acuerdo y a la que querría agradecer haber estado a mi lado estos cuatro años. Creo que una de las peores cosas que tiene la investigación es que la buena gente que conoces, y los amigos que haces, están ligados a la temporalidad de nuestros contratos. Ojalá podamos cruzar caminos de nuevo en el futuro.

Y por último, a mi familia. Aunque estemos cada uno en un lugar del mundo, y aunque solo os veo cada 2 o 3 meses, siempre habéis estado ahí, apoyando y animando. De corazón, gracias.

Contents

| | |
|---|-----------|
| Summary | xi |
| Motivation and objectives | xiii |
| Abbreviations and symbols | xv |
| 1 Introduction | 1 |
| 1.1 Electrochemistry fundamentals | 2 |
| 1.1.1 Electrode kinetics | 2 |
| 1.1.2 Mass transport | 5 |
| 1.1.3 Potential-controlled electrochemical techniques | 7 |
| 1.1.4 UV-Vis Spectroelectrochemistry | 10 |
| 1.2 Electrochemical biosensors | 11 |
| 1.2.1 Enzymatic biosensors | 12 |
| 1.2.2 Enzyme kinetics | 14 |
| 1.3 Enzymatic fuel cells | 16 |
| 1.3.1 Electrochemical characterization of fuel cells | 17 |
| 1.3.2 Self-powered biosensors | 19 |
| 1.4 Electrochromic sensors | 20 |
| 1.4.1 Electrochromic materials | 21 |
| 1.4.2 Power sources in electrochromic sensors | 24 |
| 1.4.3 Device construction | 25 |
| References | 27 |
| 2 Methods | 37 |
| 2.1 Rapid prototyping | 38 |
| 2.1.1 Cutting techniques | 38 |
| 2.1.2 Printing techniques | 39 |
| 2.2 Numerical simulation | 42 |
| 2.2.1 Finite element method | 42 |

| | | |
|----------|---|-----------|
| 2.2.2 | COMSOL Multiphysics overview | 44 |
| | References | 45 |
| 3 | A self-powered electrochromic biosensor | 49 |
| 3.1 | Introduction | 50 |
| 3.2 | Experimental | 51 |
| 3.2.1 | Reagents and materials | 51 |
| 3.2.2 | Electrode fabrication | 52 |
| 3.2.3 | Glucose biosensor construction | 54 |
| 3.3 | Results and discussion | 54 |
| 3.3.1 | Electrochemical characterization | 55 |
| 3.3.2 | Amperometric detection of glucose | 56 |
| 3.3.3 | Horizontal electrochromic displays | 58 |
| 3.3.4 | Self-powered electrochromic biosensor | 59 |
| 3.4 | Conclusions | 63 |
| | References | 64 |
| 4 | <i>iR</i> Drop effects in self-powered electrochromic biosensors | 67 |
| 4.1 | Introduction | 68 |
| 4.2 | Theory | 68 |
| 4.2.1 | Enzyme kinetics | 69 |
| 4.2.2 | Mass transport | 70 |
| 4.2.3 | Electrode processes | 70 |
| 4.2.4 | Electrolyte conductivity and ionic current | 72 |
| 4.3 | Computational procedure and model geometry | 73 |
| 4.4 | Results and discussion | 74 |
| 4.4.1 | Glucose biosensor / Anode | 74 |
| 4.4.2 | Electrochromic display / Cathode | 75 |
| 4.4.3 | Self-powered electrochromic biosensor | 80 |
| 4.4.4 | Design aspects in self-powered devices | 82 |
| 4.5 | Conclusions | 85 |
| | References | 87 |
| 5 | Screen-printed Prussian Blue electrodes | 91 |
| 5.1 | Introduction | 92 |
| 5.2 | Experimental | 94 |
| 5.2.1 | Reagents and materials | 94 |
| 5.2.2 | Instrumentation | 94 |
| 5.2.3 | Electrochromic Prussian Blue pastes | 94 |

| | | |
|----------|--|------------|
| 5.2.4 | Electrode fabrication | 95 |
| 5.3 | Results and discussion | 95 |
| 5.3.1 | Electrochemical characterization | 96 |
| 5.3.2 | Spectroelectrochemical characterization | 100 |
| 5.4 | Conclusions | 103 |
| | References | 105 |
| 6 | A fully printed self-powered electrochromic biosensor | 109 |
| 6.1 | Introduction | 110 |
| 6.2 | Experimental | 111 |
| 6.2.1 | Reagents and materials | 111 |
| 6.2.2 | Instrumentation | 111 |
| 6.2.3 | Electrode fabrication | 112 |
| 6.2.4 | Glucose biosensor construction | 113 |
| 6.2.5 | Gel polymer electrolyte | 113 |
| 6.3 | Results and discussion | 113 |
| 6.3.1 | Printed coplanar display | 113 |
| 6.3.2 | Gel polymer electrolyte characterization | 116 |
| 6.3.3 | Fully printed self-powered sensor | 118 |
| 6.4 | Conclusions | 124 |
| | References | 126 |
| 7 | Conclusions and outlook | 129 |
| 7.1 | Conclusions | 130 |
| 7.2 | Outlook | 132 |
| | References | 136 |
| | List of publications | 137 |
| | Annex 1 | 139 |
| | Annex 2 | 141 |
| | References | 143 |

Summary

Current trends in analytical chemistry aim at developing simpler and more affordable sensing devices. Electrochromic materials enable the fabrication of electrochemical sensors that exploit colour changes as a means to reduce instrumentation requirements. Although many chemical compounds used in electroanalysis exhibit electrochromic properties, the inclusion of these materials in the construction of electrochromic analytical sensors has begun to emerge only recently.

This thesis focuses on the development of a new type of analytical devices relying on the use of electrochromic materials, reducing to a minimum the required components, and removing the need for silicon-based electronics.

First, the working principle of self-powered electrochromic sensors is presented, demonstrating how with the appropriate geometry it is possible to obtain a sensing platform capable of providing a quantitative readout of the analyte concentration. The experimental data obtained are combined with the use of numerical simulations to develop a mathematical model that helps to have a further understanding of the behaviour of the device. Moreover, these simulations were used as a design tool to improve the performance of future electrochromic devices.

New materials in the form of screen-printing pastes have also been formulated to substitute certain components of the device such as the electrochromic material or the electrolyte. These materials were used in the last part of the thesis to manufacture a fully printed electrochromic sensor able to provide quantitative results without the aid of an external signaling device.

Motivation and objectives

The objective of this thesis is the design and fabrication of a self-powered electrochemical biosensor relying on the use of an electrochromic material. The advantage of using self-powered biosensors compared to other conventional electroanalytical devices is that the energy to power the system is harvested directly from the sample, removing the need for external power sources, which simplifies their miniaturization. This is achieved by integrating the power source and the sensing function into one component, instead of the traditional heterogeneous integration of most common analytical devices (Figure 1A). However, self-powered sensors still require the use of an external signaling device powered by the sensor itself. Because of this, current approaches aim at increasing the typically low energy output generated by these cells to either power electronics that actuate on a display (Figure 1B), or to directly actuate on the display (Figure 1C).

The approach demonstrated in this thesis relies on the integration of the three necessary components/functions of any analytical device, namely sensing, power generation, and information display under the same electrochemical cell (Figure 1D), so that power is no longer a limiting factor. This is achieved by modifying one of the electrodes of the cell with an electrochromic material that not only acts as a power source but it also serves as a display. Although the use of electrochromic materials in the fabrication of sensing devices has been previously reported, and particularly during the past few years, all of the described systems rely on the use of external colour readers to quantify the colour conversion of the electrochromic material to relate it with the amount of analyte present in the sample. This thesis describes how, with the appropriate materials and configuration, it is possible to turn the electric current generated by the biosensor into quantitative information in the form of a progressive discolouration of the electrochromic display.

With this approach the need for any additional electronic equipment is completely removed, which opens the door for mass production of analytical devices using printing technologies, drastically reducing the manufacturing costs.

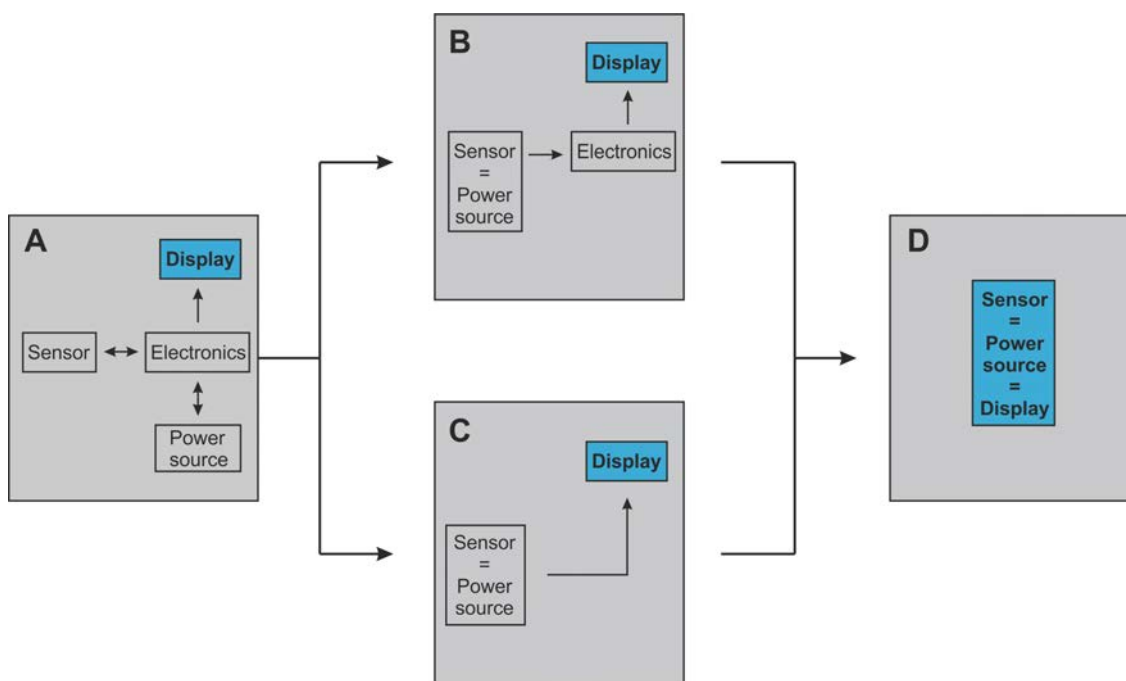


Figure 1: Schematic representation of the different components in analytical devices. (A) Heterogeneous integration of discrete components. (B)-(C) Power source and sensing functions integrated in the same component. (D) All functions integrated in one single component.

Abbreviations and symbols

| | |
|----------------------|--|
| ATO | Antimony tin oxide |
| BPE | Bipolar electrode |
| DET | Direct electron transfer |
| EMIM-Tf | 1-Ethyl-3-methylimidazolium trifluoromethanesulfonate |
| FEM | Finite element method |
| FTO | Fluorine tin oxide |
| GAc | Gluconic acid |
| GOx | Glucose oxidase |
| ITO | Indium tin oxide |
| MEMS | Micro electromechanical systems |
| MG | Methylene green |
| MV | Methyl viologen |
| NiO | Nickel oxide |
| OCV | Open circuit voltage |
| Os-PVI ₁₅ | [Os(4,4'-dimethyl-2,2'-bipyridine) ₂ (poly-vinylimidazole) ₁₅ Cl] ⁺ |
| PANI | Polyaniline |
| PB | Prussian Blue |
| PDE | Partial differential equations |
| PEC | Photoelectrochemical cell |
| PEDOT:PSS | Poly(3,4-ethylenedioxythiophene) polystyrene sulfonate |
| PEGDGE | Poly(ethylene glycol) diglycidyl ether |
| PET | Polyethylene terephthalate |
| PMS | Phenazine methosulfate |
| POC | Point-of-care |
| PPy | Polypyrrole |
| PSA | Pressure sensitive adhesive |
| PVDF-HFP | Poly(vinylidene fluoride-co-hexafluoropropylene) |
| PVI | Poly(1-vinylimidazole) |
| PW | Prussian White |
| SEM | Scanning electron microscopy |
| SPE | Screen-printed electrode |

| | |
|-----------------|--|
| TMPD | N,N,N',N'-Tetramethyl-p-Phenylenediamine |
| UA | Uric acid |
| UAB | Universitat Autònoma de Barcelona |
| UV | Ultraviolet |
| WO ₃ | Tungsten trioxide |

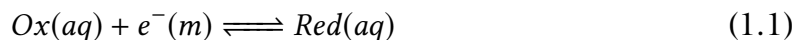
1

Introduction

This chapter presents the background behind the experimental work carried out in this thesis. First, a brief introduction to the field of electrochemistry is given, including the electrochemical techniques employed. A brief introduction to electrochemical biosensors is provided which focuses on enzymatic biosensors and their application in the field of self-powered devices. The chapter closes with an overview of electrochromic systems and their emerging applications in electroanalysis.

1.1 Electrochemistry fundamentals

Electrochemistry studies charge transfer processes at the interface between two phases. The most common case is the solid-liquid interface, formed by a solid electronic conductor (electrode) and an ionic conductor in solution (electrolyte).¹ However, it is possible to find other interfaces such as liquid-liquid² or gas-solid³ at which electrochemical processes occur. The charge transfer process can be either spontaneous or deliberately generated to bring about a chemical reaction in the interface. Redox processes occurring at an electrode-solution interface⁴ are generally expressed as:



where the subscript m represents the metal electrode, and Ox and Red represent the two oxidation states of an electroactive species. The concentrations of both species in equilibrium are related to the electrode potential, E , by the Nernst equation:

$$E = E^{0'} + \frac{RT}{F} \ln \frac{[\text{Ox}]}{[\text{Red}]} \quad (1.2)$$

where $E^{0'}$ represents the formal potential of the redox couple, that includes the standard potential, E^0 , plus the effects of ionic strength and parallel reactions of the species involved in the electrochemical process.⁵ R is the gas ideal constant ($8.314 \text{ J K}^{-1} \text{ mol}^{-1}$), T is the absolute temperature (K), and F is the Faraday constant (96485 C mol^{-1}). The electrode potential can be externally controlled by a power supply, which modifies the equilibrium in equation 1.1 and creates a flow of electrons between the electrode and the electroactive species in the solution. As described below, if the electrode potential is lower than the formal potential of the redox couple, then electrons flow from the electrode towards the solution, causing the reduction of the electroactive species. This electrode is termed “cathode”. On the other hand, an oxidation would take place if the applied potential is higher than the formal potential, and the electrode is then termed “anode”.

The overall process of electron transfer between the solution and the electrode is rather complex, and may be controlled by the rate of one of the following four different processes:¹ mass transport from the solution to the surface of the electrode and vice versa, electron transfer at the surface of the electrode, surface reactions at the electrode, and coupled chemical reactions of the electroactive species (Figure 1.1).

Because of their relevance to this thesis, electron transfer and mass transport phenomena will be further described in the following sections.

1.1.1 Electrode kinetics

Electrode potential determines whether a particular electrode reaction takes place or not. Moreover, the rate of that reaction depends on the magnitude of that potential. For this, it

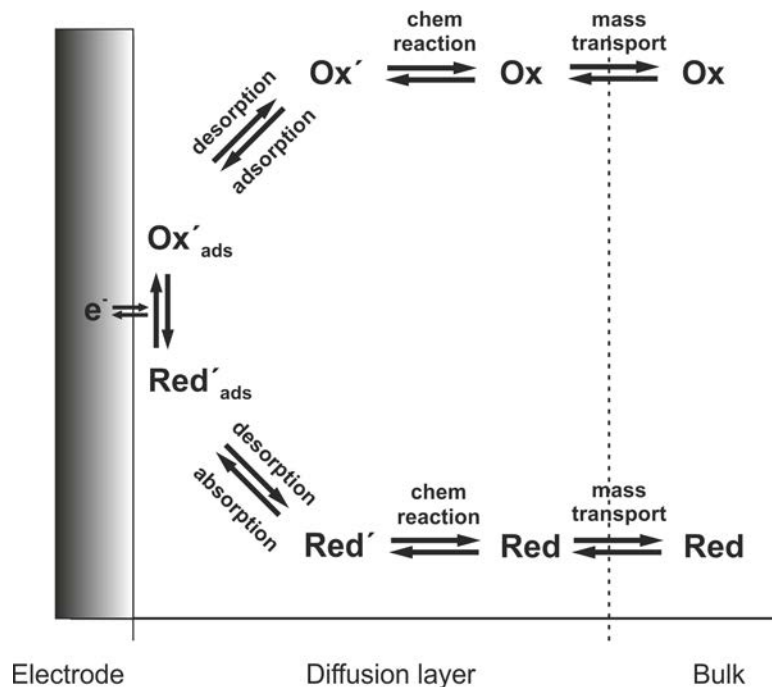


Figure 1.1: Schematic of the processes that may take place at the electrode-solution interface.

is necessary to develop a mathematical model that accounts for that potential-dependence of the reaction rate. Consider the usual redox system:



where k_{red} and k_{ox} are the rate constants for the reduction and the oxidation process, respectively. The rate of both forward and backward reactions can be written as follows:

$$v_{red} = k_{red}C_{Ox} \quad (1.4)$$

$$v_{ox} = k_{ox}C_{Red} \quad (1.5)$$

so the net reaction rate is:

$$v = k_{red}C_{Ox} - k_{ox}C_{Red} \quad (1.6)$$

In combination with Faraday's laws,¹ the general expression for the reaction rate is then obtained:

$$i = i_{red} - i_{ox} = nFA(k_{red}[Ox]_0 - k_{ox}[Red]_0) \quad (1.7)$$

where A represents the area of the electrode, n the number of electrons involved in the redox process, and the subscripts 0 next to the concentration terms refer to the concentration of Red and Ox at the electrode surface.

It has been experimentally observed that the electric potential of the electrode affects considerably the rate of the chemical reactions taking place on its surface. Figure 1.2

4 Design and development of a self-powered electrochromic biosensor

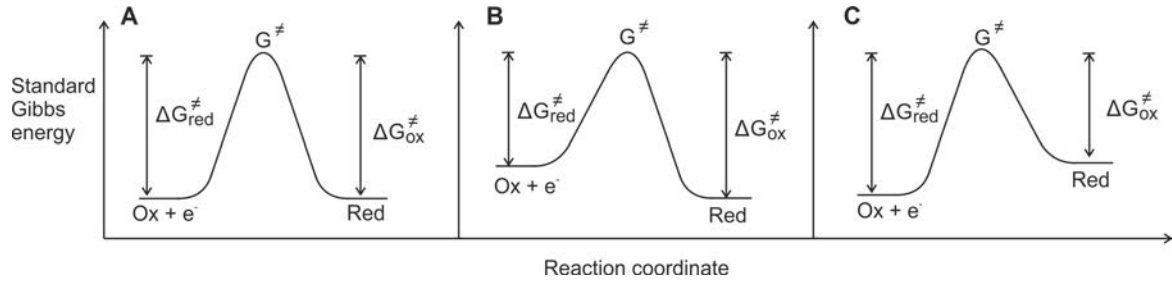


Figure 1.2: Diagrams showing the free energy evolution in an electrochemical process at three different applied potentials. (A) Electrode potential at equilibrium. (B) Electrode potential more negative than equilibrium value. (C) Electrode potential more positive than equilibrium value.

shows three free energy diagrams for an electrochemical process, which have a certain potential-dependent energy barrier. Taking into account the Arrhenius equation for rate constants:⁶

$$k = A \exp\left(\frac{-\Delta G}{RT}\right) \quad (1.8)$$

where R is the universal gas constant, T the absolute temperature, and A the frequency factor of collisions of the reacting species in solution with the electrode surface, it is shown that the electron transfer rate constant depends on the electric potential. When the electric potential is changed, the free energy in the curves in Figure 1.2 also changes, as follows:

$$\Delta G_{red}^{\ddagger} = \Delta G_{red,0}^{\ddagger} + \alpha F(E - E^{0'}) \quad (1.9)$$

$$\Delta G_{ox}^{\ddagger} = \Delta G_{ox,0}^{\ddagger} - (1 - \alpha)F(E - E^{0'}) \quad (1.10)$$

where $0 < \alpha < 1$. α represents the charge transfer coefficient for the electrochemical process, and it is usually assumed to be 0.5, which means that the transition state is placed exactly mid-way between reactants and products.^{1,6,7} Substituting these expressions in the Arrhenius equation leads to a relation between the applied potential E and the electron transfer rate constant k for each species:

$$\begin{aligned} k_{red} &= A_{red} \exp\left(\frac{-\Delta G_{red,0}^{\ddagger}}{RT}\right) \exp\left[-\alpha \frac{F}{RT}(E - E^{0'})\right] \\ k_{ox} &= A_{ox} \exp\left(\frac{-\Delta G_{ox,0}^{\ddagger}}{RT}\right) \exp\left[(1 - \alpha) \frac{F}{RT}(E - E^{0'})\right] \end{aligned} \quad (1.11)$$

where A represents probabilistic factors describing the frequency of the collisions of the reacting species in solution with the electrode.⁸

A valid kinetic model must also apply at any given experimental conditions, that also includes the equilibrium situation where the concentration of both electroactive species Ox and Red is equal, and thus $E = E^{0'}$. In this situation, both anodic and cathodic currents are compensated, given a net current flux of zero, and from equation 1.7 it is obtained

that $k_{red} = k_{ox}$. This value of the rate constant, which is independent from the potential, is called the *standard rate constant*, k^0 , and allows the simplification of rate constant equations:

$$\begin{aligned} k_{red} &= k^0 \exp[-\alpha f(E - E^{0'})] \\ k_{ox} &= k^0 \exp[(1 - \alpha)f(E - E^{0'})] \end{aligned} \quad (1.12)$$

where $f = F/RT$. Combining these expressions with equation 1.7, leads to the Butler-Volmer equation:

$$i = F A k^0 \left([Ox]_0 \exp\left[-\alpha f(E - E^{0'})\right] - [Red]_0 \exp\left[(1 - \alpha)f(E - E^{0'})\right] \right) \quad (1.13)$$

which relates the electrochemical potential with the electric current flowing through the system.

This kinetic model tells us that the electron transfer rate constant not only depends on the applied electrode potential but that this dependence is exponential, which implies that the electric current should always increase exponentially with the applied potential. This is not the case in actual electrochemical experiments as mass transport effects limit the kinetic predictions of the Butler-Volmer model, as shown in following sections.

The Butler-Volmer model applies only at a macroscopic scale. Marcus' model,^{9,10} later extended by Hush,^{11,12} supersedes this with a microscopic model that separates the total Gibbs energy of activation into two terms:⁷

$$\Delta G^\ddagger = \Delta G_i^\ddagger + \Delta G_0^\ddagger = \frac{1}{4}(\lambda_i + \delta_0) \quad (1.14)$$

where ΔG_i^\ddagger represents the activation energy related to the bond length and angle changes in the electroactive molecule in the transition state during the electron transfer, and ΔG_0^\ddagger the activation energy related to the rearrangement of the solvent molecules around the transition state.

For the work carried out in this thesis, the microscopic model was not used, and electron transfer in the electrochemical reactions considered has been treated according to the Butler-Volmer model only.

1.1.2 Mass transport

When electron transfer is sufficiently fast, mass transport usually becomes rate limiting.

There are three main modes of mass transport,¹³ namely diffusion, migration, and convection; so the net current density of a mass transport controlled process can be described by:

$$j_{mass\ transport} = j_{diffusion} + j_{migration} + j_{convection} \quad (1.15)$$

Diffusion

Diffusion involves the microscopic random movement of species due to concentration gradients. The flux of substance is mathematically described by Fick's laws.¹⁴ The first of Fick's laws relates the concentration gradient with the position as:

$$j = -D\nabla C \quad (1.16)$$

where D is the diffusion coefficient of the substance in solution, and C its concentration. The negative sign implies that the flux of material takes places from high to low concentrations.

Fick's second law describes the flux at a given position as a function of time:

$$\frac{\partial C}{\partial t} = D\nabla^2 C \quad (1.17)$$

Fick's equations are of extreme importance to electrochemists as generally the final approach electroactive species to the electrode surface is by diffusion.⁷

Migration

Migration is the microscopic movement of charged chemical species inside an electric field. Migrational flux is described by:

$$j = -\frac{zF}{RT}DC\nabla\phi \quad (1.18)$$

where z is the charge of the species, C its concentration, D the diffusion coefficient, and ϕ the electric potential. It is common practice in electroanalysis to use solutions with an excess of an inert salt, also known as supporting electrolyte, that minimizes the contribution of the electroactive analytes to the migration component in equation 1.15.

Convection

The convective mode of mass transport implies the macroscopic movement of "packets" of solution either by natural or forced means. There are two forms of convection: natural and forced convection. Examples of natural convection would be the movements arising from large gradients in density, pressure or temperature. Forced convection, on the other hand, is induced by external forces such as stirring, pumping or capillary forces.¹⁵ Convective mass transfer is mathematically described by:

$$j = Cv \quad (1.19)$$

where v represents the velocity of the liquid, and C the concentration of the species.

The combination of the three different contributions to the global mass transport in an electrochemical system is then defined as:

$$j = -D\nabla C - \frac{zF}{RT}DC\nabla\phi + Cv \quad (1.20)$$

Equation 1.20 is known as the Nernst-Planck equation, and will be of special interest in the discussion of the mathematical model presented in Chapter 4.

In the absence of migration and convection, diffusion becomes the only mass transport process, which facilitates considerably the interpretation of the experimental data.¹⁶

1.1.3 Potential-controlled electrochemical techniques

An important set of electrochemical techniques relies on the measurement of the current response of a system following a controlled change in electrode potential. As explained above, the application of an electric potential to an electrochemical system may bring about a change in the oxidation state of the electroactive species, generating a flux of electric current. By analyzing this current response, electrochemists can extract valuable information of their system, both qualitative and quantitative.¹⁷ This section summarizes the two main electroanalytical techniques used in this thesis: chronoamperometry and cyclic voltammetry.

Chronoamperometry

Chronoamperometry is one of the simplest electroanalytical techniques, yet it can provide very valuable information about the studied electrochemical system. It consists of the application of a potential step from a value where no reaction occurs, and hence no current is observed, to another at which the reduction or the oxidation of the species under study takes place, and thus an electric current is generated (Figure 1.3A). Within the first milliseconds after the potential jump, the concentration of the electroactive species at the surface of the electrode drops to zero, producing a concentration gradient in the surroundings of the electrode, and resulting in a transient current as seen in Figure 1.3B. In a system where the other mass transport phenomena —migration and convection— can be neglected, the current transient response is described by the Cottrell equation:¹⁸

$$I(t) = nFAC\sqrt{\frac{D}{\pi t}} \quad (1.21)$$

where n represents the number of electrons exchanged, A the area of the electrode, C the concentration of the electroactive species, and D its diffusion coefficient. The usefulness of this equation in electroanalysis is clear, as it allows to relate the registered current of an experiment with the concentration of the electroactive substance and with its diffusion

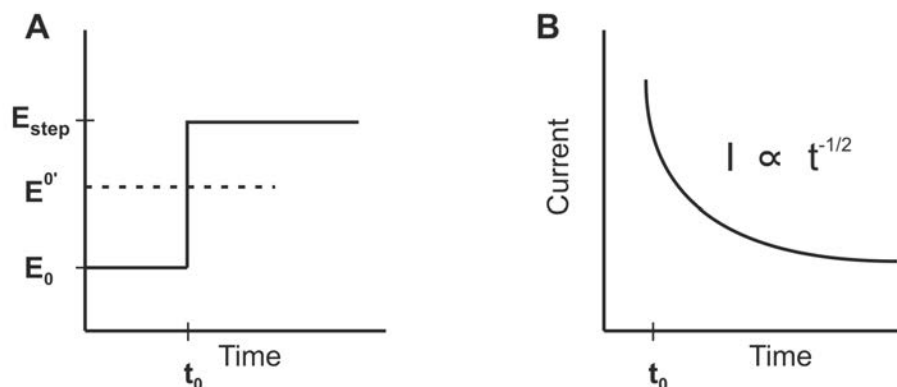


Figure 1.3: (A) Plot of the potential step function applied on the electrode. (B) Transient current registered for an amperometric experiments.

coefficient. This equation also shows the inverse relation of the electric current with $t^{1/2}$, representing the behaviour of a purely diffusion-controlled regime. As the electrolysis progresses, the electrode converts the analyte in the surroundings creating a depletion zone known as the diffusion layer (δ)⁷ that increases according to:

$$\delta \approx \sqrt{Dt} \quad (1.22)$$

Cyclic voltammetry

Another important and well-known technique is cyclic voltammetry.^{19,20} In this case, a triangular potential wave is applied to the electrode, as depicted in Figure 1.4A. Cyclic voltammograms result from plotting the current response against the applied potential (Figure 1.4B). The potential sweep is usually started at a potential where no electric current is observed. As the applied potential approaches the formal potential of the electroactive species present, the electric current increases exponentially, as predicted by the Butler-Volmer model (eq. 1.13). Because the slope of this increase will depend on the rate of the electron transfer, steeper slopes are indicative of faster electron transfer. The rate of the electron transfer defines the electrochemical reversibility of a redox system, observing three situations: reversible, irreversible, and quasi-reversible systems.

During the voltammetric experiment of Figure 1.4, the potential is swept starting at a potential lower than $E^{0'}$, so no faradaic current is observed. As the electrode potential approaches $E^{0'}$, the oxidation of the species begins, and an anodic current is generated. As the electrolysis progresses, the concentration of the reduced species decays, and diffusion sets in, carrying the species from the bulk to the electrode surface. When the rate of mass transport is not enough to replace the depleted material at the electrode surface, the system switches from a kinetic to a diffusion control regime, observing a peak in the voltammogram ($I_{p,a}$). Another peak ($I_{p,c}$) appears when the potential is swept back to the

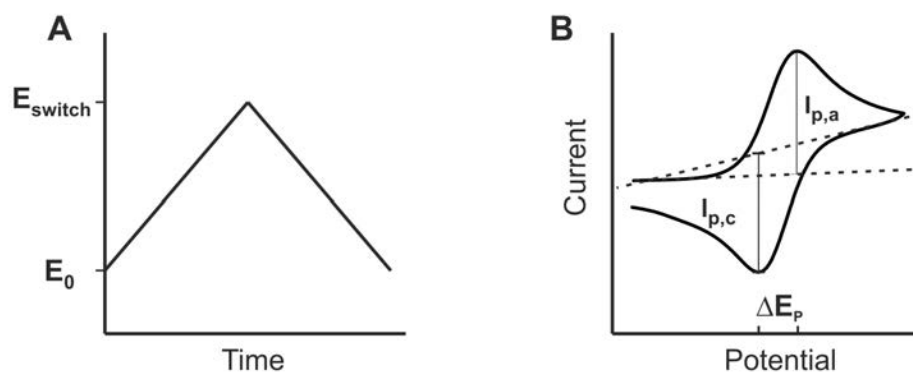


Figure 1.4: (A) Representation of the triangular potential function applied in cyclic voltammetric experiments. (B) Typical cyclic voltammogram obtained upon application of a triangular potential sweep.

initial value. The subscripts ‘a’ and ‘c’ refer to the anodic and cathodic currents, following IUPAC’s (International Union for Pure and Applied Chemistry) recommendations for sign convention. Each of the observed peaks appears at a certain voltage, $E_{p,a}$ and $E_{p,c}$ for the anodic and cathodic process, respectively, and allow the determination of the formal potential of an electroactive species:

$$E^{0'} = \frac{E_{p,a} + E_{p,c}}{2} \quad (1.23)$$

The position of the current peaks also allows to have an estimation of the electrochemical reversibility of the redox system as fast electron transfers reach a lower limit of 59 mV.¹ As the electron transfer becomes more sluggish, this separation increases, observing, in certain cases, the vanishing of one of the two peaks.^{21,22}

The true potential of voltammetric techniques lies in the amount of information that they can provide of the electrochemical system by analyzing the magnitudes of the peak currents, their position, and their time dependence. For instance, different methods have been proposed to determine the electron transfer rate constant by plotting the peak-to-peak separation against the scan rate,^{21,23,24} making it possible to classify electrochemical processes as reversible, irreversible or quasi-reversible.⁷

In a similar way, peak currents can also be used to provide information about the nature of the electrochemical system. The magnitude of the peak current is characteristic of each electrochemical system, and depends on different variables as illustrated by the Randles-Ševčík equation:

$$I_p = \psi nFAC \sqrt{\frac{nFD\nu}{RT}} \quad (1.24)$$

where ν represents the scan rate of the electric potential, ψ is the dimensionless current that is function of the electron transfer rate,²⁴ and takes values between 0.3507 to 0.4463

for irreversible to fully reversible systems, respectively.⁸ Two important details can be read from equation 1.24: (i) that a linear dependence is predicted between the peak current of a voltammogram and the concentration of the electroactive species in solution, which allows the use of cyclic voltammetry as a quantitative technique for analysis, and (ii) that a linear relation between the peak current and the square root of the scan rate can be expected. This last point is particularly interesting since it makes it possible to know if an electrochemical process is diffusion-controlled or if, on the other hand, the analyte experiences surface-controlled phenomena, in which case the relation between peak current and scan rate should be linear.²⁵

1.1.4 UV-Vis Spectroelectrochemistry

Electrochemical techniques such as voltammetry or chronoamperometry provide valuable information regarding the concentration of electroactive species, energy data and kinetic parameters of electrochemical reactions. However, they are not able to provide structural information about the species formed as intermediates or products in a redox reaction²⁶ or in mixtures of reactants.^{8,27}

Spectroelectrochemical methods couple electrochemical and spectroscopic techniques, which allows to obtain information regarding the electronic or vibrational transitions of a particular molecule undergoing an electrochemical process.²⁸ In this sense, typical spectroscopic methods used in spectroelectrochemistry include absorption spectroscopy in the visible/ultraviolet region (UV-vis)²⁹ or in the infrared region (NIR/IR).³⁰ Other spectroscopic methods involve Raman scattering spectroscopy,³¹ nuclear magnetic resonance (NMR)³² or X-ray absorption spectroscopy.³³

As explained below, the work carried out in this thesis relies on the used of electroactive species which display colour changes as a function of their redox state upon application of an electric potential. This colour change is associated with a modification in the electronic configuration of the molecule, which was studied by visible absorption spectroscopy. The coupling of an absorption spectroscopic method can be done in two modes: transmission or reflection. Transmission mode is preferred when the electroactive species is in solution, and requires the use of optically transparent electrodes. On the other hand, when the analyte is present in the form of a solid layer on the electrode surface, the reflection mode is more convenient.⁸ In this thesis, reflectance spectroelectrochemical methods were used to characterize the solid and coloured electroactive materials developed.

An example of the potential of combining electrochemical and spectroscopic techniques is depicted in Figure 1.5. A cyclic voltammogram of an electroactive species can be registered, and, simultaneously, changes produced in its absorbance intensity at a fixed wavelength can be recorded to obtain its voltabsortogram (Figure 1.5A). The power of combining both analytical techniques is in how the two techniques complement each

other. A clear example of this is observed when the derivative of the voltabsortogram is obtained (Figure 1.5B). The spectroscopic detection is only sensitive to changes in the colour of the electroactive species generated by the faradaic current flowing through the electrodes, and, in contrast to cyclic voltammetry, is not affected by capacitive currents, which results in a much lower background signal. The application of these UV-Vis spectroelectrochemical techniques will be described in Chapter 5.

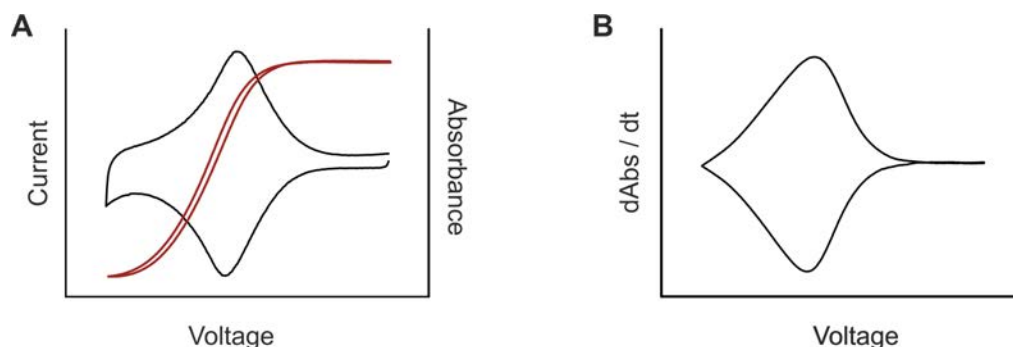


Figure 1.5: (A) Typical cyclic voltammogram of a reversible electroactive species (black line) and the corresponding voltabsortogram for a fixed wavelength (red line). (B) Derivative of the corresponding voltabsortogram.

1.2 Electrochemical biosensors

Electrochemistry is not only a powerful tool to study electroactive species, but it can also be used for the study of coupled chemical phenomena.³⁴ As seen in section 1.1, different physical and chemical phenomena may affect the electrode process and, consequently, the potential or the current registered during the electrochemical measurement. Coupling chemical reactions to electroactive species is a very common way to detect/quantify substances that would otherwise be electrochemically invisible.³⁵ Such reactions can take place either in the solution bulk or they can be confined to a very small region in the vicinity of the electrode, e.g. a reaction of the analyte with a product of an electrochemical reaction at the surface of the electrode.³⁶ A very common approach to the latter is the chemical modification of the electrode surface so that not only does the reaction occur close to it, but it also does so selectively to a certain analyte. This is the working principle of most electrochemical (bio)sensors.

Biosensors are analytical devices that generate a measurable signal upon reaction with a specific analyte.³⁷ They rely on the use of biorecognition elements such as enzymes, nucleic acids, antibodies or cells for the modification of the transducer, thus leading to enzymatic biosensors, genosensors, immunosensors or cytosensors, respectively.³⁸ These biomolecules, immobilized on a transducer surface, selectively recognize the analyte, and

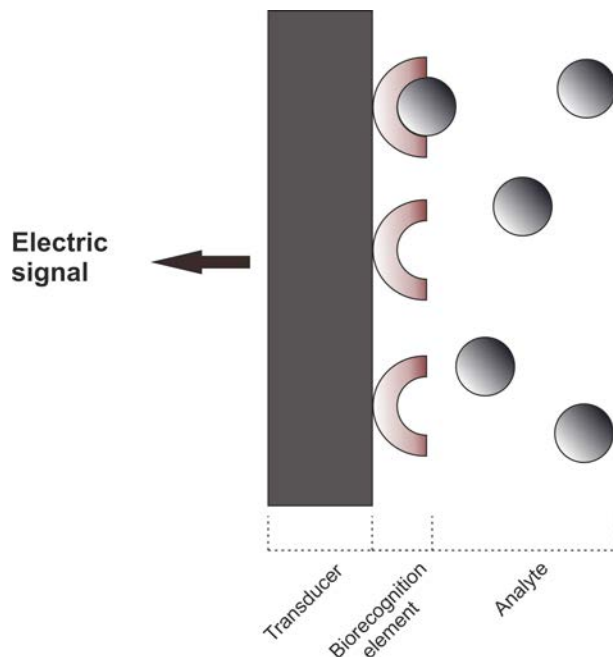


Figure 1.6: Diagram of the different components integrating an electrochemical biosensor.

bring about the chemical reaction that generates a quantitative signal. In the case of amperometric biosensors, where the transducer is the surface of an electrode, an electric current flows upon the recognition reaction (Figure 1.6). The biosensors presented in this thesis rely on an amperometric transduction system.

Electrochemical glucose biosensors were selected to carry out the experimental work. Diabetes mellitus is a metabolic disorder which results in high blood glucose levels, and that has become a major public health problem. It is estimated that this disease affects approximately 150 million people around the world, and the tendency is that this number may be double by 2025.³⁹ To prevent the possible complications of the disease, such as kidney failure, foot ulcers or strokes, it is important to have a rigorous control of blood glucose levels during the day. For this, a lot of research has been carried out to develop more stable and reliable glucose biosensors. These biosensors are, by far, the best-known and characterized in the bibliography, accounting for about 85% of the entire biosensor market.^{40,41} Because of their importance and maturity, glucose biosensors have been used throughout this work, which has allowed to have a reliable system to demonstrate the proof of concept presented in this thesis.

1.2.1 Enzymatic biosensors

Enzymatic biosensors rely on the catalytic activity of enzymes towards their natural substrates. The reaction between the enzyme and the substrate brings about an electrochemical response that can be registered with different electrochemical techniques, leading to

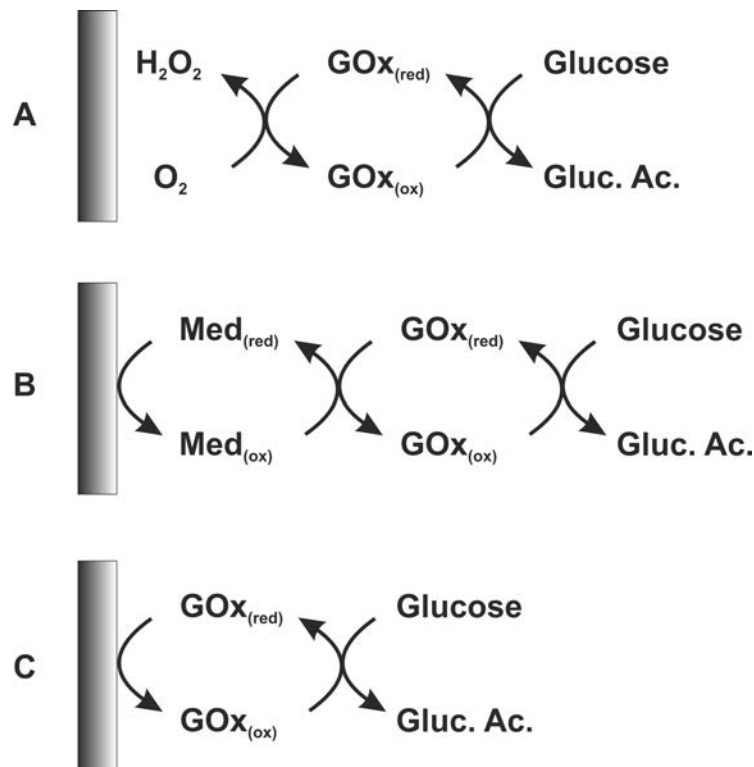


Figure 1.7: Schematic representation of the different generations of amperometric glucose biosensors. (A) First, (B) second, and (C) third generation.

amperometric, potentiometric or impedimetric biosensors.^{42,43} The glucose biosensor selected in this thesis relies on the use of the oxidoreductase enzyme glucose oxidase (GOx) to catalyze the oxidation of glucose to gluconic acid.⁴⁴

The catalytic activity of the enzyme can be measured by controlling the evolution of the different chemical species present in the biosensor. Enzymatic biosensors have evolved through three “generations” (Figure 1.7):

First generation biosensors⁴⁵ measure the variation in the amount of oxygen or hydrogen peroxide during the enzymatic reaction. As seen in Figure 1.7A, the glucose oxidase accepts electrons from glucose, converting it into gluconic acid, and changing its own redox state in the process. These electrons are then transferred to dissolved oxygen present in solution, generating hydrogen peroxide, and returning glucose oxidase to its oxidized state so that the enzymatic reaction can continue. By applying a sufficiently high potential, -0.6 V (vs Ag/AgCl)⁴⁶ for the reduction of oxygen or $+0.6\text{ V}$ (vs Ag/AgCl)⁴¹ for the oxidation of hydrogen peroxide, the concentration of glucose can be related to the magnitude of the recorded amperometric signal. The biggest drawback of these type of biosensors is the need to apply relatively high potentials to register an amperometric response to oxygen or hydrogen peroxide, which often leads to interference from other substances present in real samples, such as ascorbic or uric acid.⁴¹

Second-generation biosensors eliminate these drawbacks by using low-potential redox mediators.⁴⁷ These compounds interact directly with the active sites of the enzymes, accepting electrons after the enzymatic reaction, and shuttling them to/from the electrode surface in a process known as *mediated electron transfer* (MET).⁴⁸ After electrons are transferred to the electrode, the mediator turns back to its original redox state and continues the shuttling of electrons (Figure 1.7B). These redox mediators must fulfill certain important requirements in order to be considered for the fabrication of enzymatic biosensors such as fast electrode kinetics, reversibility in the reaction with the enzyme, high stability or low toxicity among others.⁴⁹

Last, **third-generation** biosensors are based on the direct electron transfer between the active site of the enzyme and the electrode, in a mechanism known as *direct electron transfer* (DET).⁴⁸ Most enzymes, and particularly glucose oxidase, present a deeply buried active site, so the electron transfer is highly hindered and a modification of the electrode, usually with nanomaterials,⁵⁰ is necessary to enable DET.⁵¹

For these reasons, the most common approach in the bibliography, and also the one chosen in this thesis, is the use of second-generation biosensors.

When building second-generation biosensors, it is preferred to have immobilized on the surface of the electrode all the necessary components to carry out the electrochemical measurement without the addition of extra substances to the sample.^{43,52} Some critical aspects to bear in mind during the fabrication of the biosensor are: (i) to keep an intimate contact between the active site of the enzyme and the redox mediator, (ii) to have a high stability of the enzymes present in the biosensor, preventing their denaturation, (iii) to obtain an adequate immobilization of the redox mediator, avoiding its leakage to the sample, and (iv) to block the access of possible interfering compounds.⁵³

A number of different strategies exist in the bibliography to immobilize the components of a biosensor, distinguishing the following five:⁵⁴ (i) entrapment in a three-dimensional matrix, (ii) physical adsorption on the electrode surface, (iii) cross-linking between the components to form a matrix adhered to the electrode, (iv) covalent-binding upon chemical components and the (un)modified surface, and (v) affinity of an activated electrode surface to a specific group present in a protein or DNA molecule. Each immobilization method offers certain advantages and disadvantages that one must consider when designing an electrochemical biosensor. The two glucose biosensors described in this thesis make use of a combination of the first three methods, since they allow for a fast modification of the electrode surface while showing good stability and robustness.

1.2.2 Enzyme kinetics

Enzymatic biosensors monitor the activity of the immobilized enzymes through measurements of concentration changes of either a substrate or a product of the reaction. The

first studies on enzymatic activity date from the latter half of the nineteenth century,⁵⁵ but it wasn't until the work of Michaelis and Menten a few decades later that a fully described mechanism for enzymatic reactions was presented.⁵⁶ The enzymatic reactions proposed are as follows:



where E represents the enzyme, S is the enzyme substrate, ES an enzyme-substrate complex, and P the product resulting from the reaction. By using the steady-state approximation on the enzyme-substrate complex,⁵⁷ that is its concentration can be considered constant with time, the general Michaelis-Menten expression can be extracted:

$$v = \frac{d[P]}{dt} = k_{cat}[E]_0 \frac{[S]}{K_M + [S]} \quad (1.26)$$

where $[E]_0$ represents the initial concentration of enzyme ($[E]_0 = [E] + [ES]$), and $K_M = (k_{-1} + k_{cat})/k_1$ is the Michaelis-Menten rate constant. As seen in Figure 1.8A, the velocity of the enzymatic reaction increases linearly with the concentration of substrate, until it reaches a plateau where an increment of substrate concentration does not turn into higher reaction rates, observing then the situation where $[S] \gg K_M$, and thus $v = v_{max} = k_{cat}[E]_0$. As seen also in Figure 1.8A, the value of the Michaelis-Menten constant can be obtained from the plot, at the point where $v = v_{max}/2$

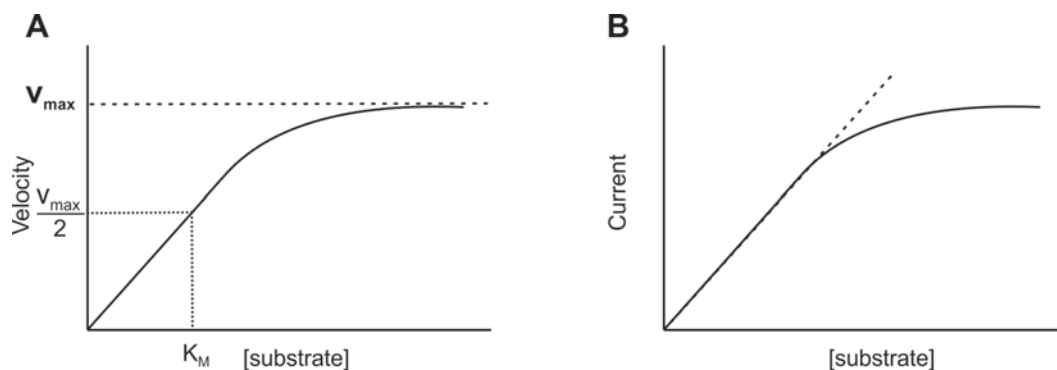
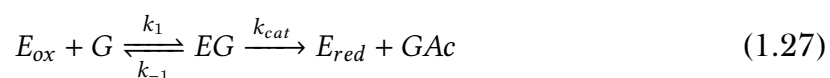


Figure 1.8: (A) Plot of the velocity of the enzymatic reaction against the substrate concentration. (B) Plot of the electric current response against the concentration of analyte.

These concepts are of great importance as the kinetic parameters of an enzymatic system can be experimentally extracted.

When an oxidase such as the glucose oxidase employed in this thesis reacts with glucose present in the sample, the following electrochemical reactions take place:



where G and GAc represent glucose and gluconic acid respectively. The oxidation of glucose also brings about the change in the redox state of the enzyme, and it is the electrode

that, upon application of an electric potential, accepts the electrons gained by the enzyme so it can be reoxidized and its enzymatic activity reinstated.

Considering that the velocity of the enzymatic reaction can also be expressed as $v = d[E]/dt$, and bearing in mind equations 1.6 and 1.7, the velocity of an enzymatic reaction can be related to a measurable parameter: current intensity (Figure 1.8B). The region where a linear behaviour is observed is usually chosen to perform the calibration plots in any electroanalytical experiment, as it presents the highest sensitivity.

The described situation represents a general case where the enzyme is capable of interacting with the electrode (direct electron transfer). However, as mentioned above, this is rather uncommon, and the inclusion of a redox-mediator is often necessary. A slight variation in the mathematical treatment of the enzymatic reaction must be made to take into account the effect of the redox mediator in the overall reaction rate. The interaction between the enzyme and the mediator is described by:



Electrons are removed from the enzyme, regenerating its active state, and the mediator diffuses to the electrode where is reoxidized by action of the applied electric potential, so the catalytic cycle is established as in Figure 1.7B. The rate of the enzymatic reactions 1.27 and 1.28 is then given by:⁵⁸

$$v = \frac{k_{cat}[E]_{tot}}{1 + \frac{K_M}{[G]} + \frac{K_0}{[O]}} \quad (1.29)$$

where $K_0 = k_{cat}/k$ and $E_{tot} = E_{ox} + E_{red} + EG$.

1.3 Enzymatic fuel cells

The electroanalytical devices presented in this thesis rely on the use of enzymatic fuel cells as a means to power the sensing reaction of glucose.

A fuel cell is an electrochemical system capable of generating electric energy from a chemical reaction occurring between its anode and its cathode.^{59,60} The cell voltage, the amount of electric current, and the power output generated depend on a number of factors such as electron transfer and reaction rates, internal resistance inside the cell, or cell geometric design.^{61–63}

The same principles of electrode modification used in the fabrication of electrochemical biosensors can be applied to fuel cells, so electrode reactions take place when a specific substance or “fuel” is present.

Understanding the catalytic behaviour of enzymes led to their inclusion in the design of fuel cells. Enzymatic fuel cells rely of the modification of both anode and cathode, or

just one of the couple, with enzymes so an electric current is generated the substrate is present (Figure 1.9).⁶⁴

The energy generated by enzymatic fuel cells has been exploited over the last two decades, and remarkable advances have been made in fields like implantable power sources to develop devices such as battery-less pacemakers,⁶⁵ energy sources to replace conventional batteries in small electronic devices,⁶⁶ or self-powered sensors that permit to detect/quantify an analyte without the use of conventional electronic equipment.⁶⁷ All of these advances have had an extraordinary impact on the development of point-of-care personalized healthcare instrumentation⁶⁸ and particularly for the development of wearable and implantable sensing devices.⁶⁹

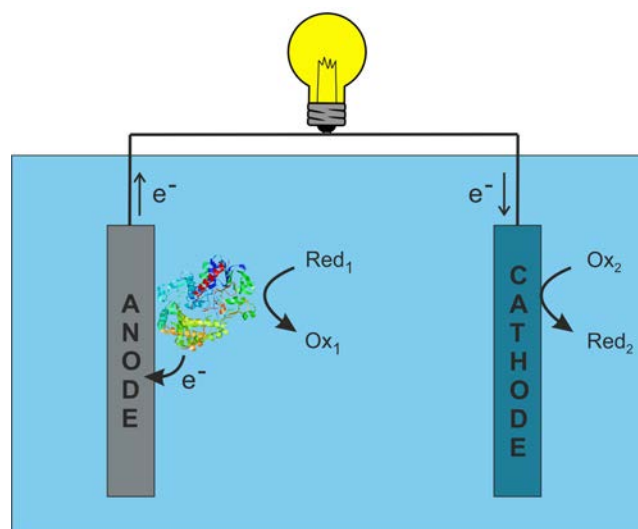


Figure 1.9: Schematic representation of a common enzymatic fuel cell where the anode has been modified with an oxidase enzyme.

1.3.1 Electrochemical characterization of fuel cells

A first approach in the characterization of any fuel cell is to evaluate the behavior of the redox mediator(s) used. Cyclic voltammetry is the most common technique employed for this characterization since valuable information can be extracted regarding its electrochemical performance such as the formal potential ($E^{0'}$), kinetic parameters or its stability under a continuous oxidation-reduction cycling regime.⁷⁰ Cyclic voltammetry can also be used to evaluate the catalytic activity of the enzyme(s) used.

As Figure 1.10A shows, for the case where the electrode acts as anode, when no enzymatic substrate is present in the solution the voltammogram presents its classical shape where both cathodic and anodic peaks are observed (Curve 1). As the amount of substrate is increased in the solution, the amount of redox mediator in its reduced state also increases, observing higher anodic currents (Curve 2). If the voltammograms of both anode

and cathode are superposed as in Figure 1.10B, a global overview of the performance of the fuel cell can be extracted. First, the open circuit voltage (OCV) is defined as the potential difference between both electrode processes when no electric current is flowing through the system. It represents the maximum voltage output that a cell can deliver, and it provides a first estimation of the amount of energy that can be extracted from it. As explained in following chapters, it is useful to know the cell voltage not only when no electric current is flowing but also when the system is working and an electric current is being generated between anode a cathode. This cell voltage is defined as:

$$\Delta E_{cell} = E_{cat} - E_{an} - iR \quad (1.30)$$

where E_{cat} and E_{an} represent the potential of the redox species at the cathode and the anode, respectively, and iR represents the ohmic drop between the two poles. This equation is of great interest as it allows to evaluate if an electrochemical process is thermodynamically favorable ($\Delta E_{cell} > 0$) or not ($\Delta E_{cell} < 0$), or whether the system lies in an equilibrium state ($\Delta E_{cell} = 0$).

The overall electrochemical cell performance is limited by one of its two electrodes. In a sensing device, it is important to ensure that the sensor is always limiting.⁷¹

It is also important to note the effect that the ionic conductivity of the supporting electrolyte and the geometric design of the cell may have on its electrochemical behavior. As described in Chapter 4, both parameters markedly affect the internal resistance of the enzymatic cell, which diminishes the cell voltage (equation 1.30) and thus the overall electrochemical performance of the system.

A complete evaluation of the fuel cell performance is achieved by extracting its polarization curves and the corresponding power curves.⁷² Polarization curves are obtained by applying a variable potential ranging from the OCV to the short circuit potential (0 V) and recording the current generated by the system. The potential is swept at very low scan rates ($<1 \text{ mV s}^{-1}$) so the system always lies close to its equilibrium-state, thus minimizing possible alterations arising from the potential sweep. As seen in Figure 1.10C, the amount of electric current progressively increases as the applied potential goes from OCV, where no redox reaction takes places, to the short circuit, where the enzymatic reaction at the anode reaches its maximum rate. Deviations in the polarization curves from its ideal behaviour may arise as a consequence of different phenomena such as slow electrode kinetics, ohmic losses due to electrolyte resistance or concentration effects due to mass-transfer limitations.⁷²

Power curves, such as those in Figure 1.10D, can be obtained from the polarization plots, by multiplying the cell voltage by the current density:

$$P_{cell} = V_{cell} \cdot j \quad (1.31)$$

Power curves offer a direct measure of the optimal operational conditions of a fuel cell,

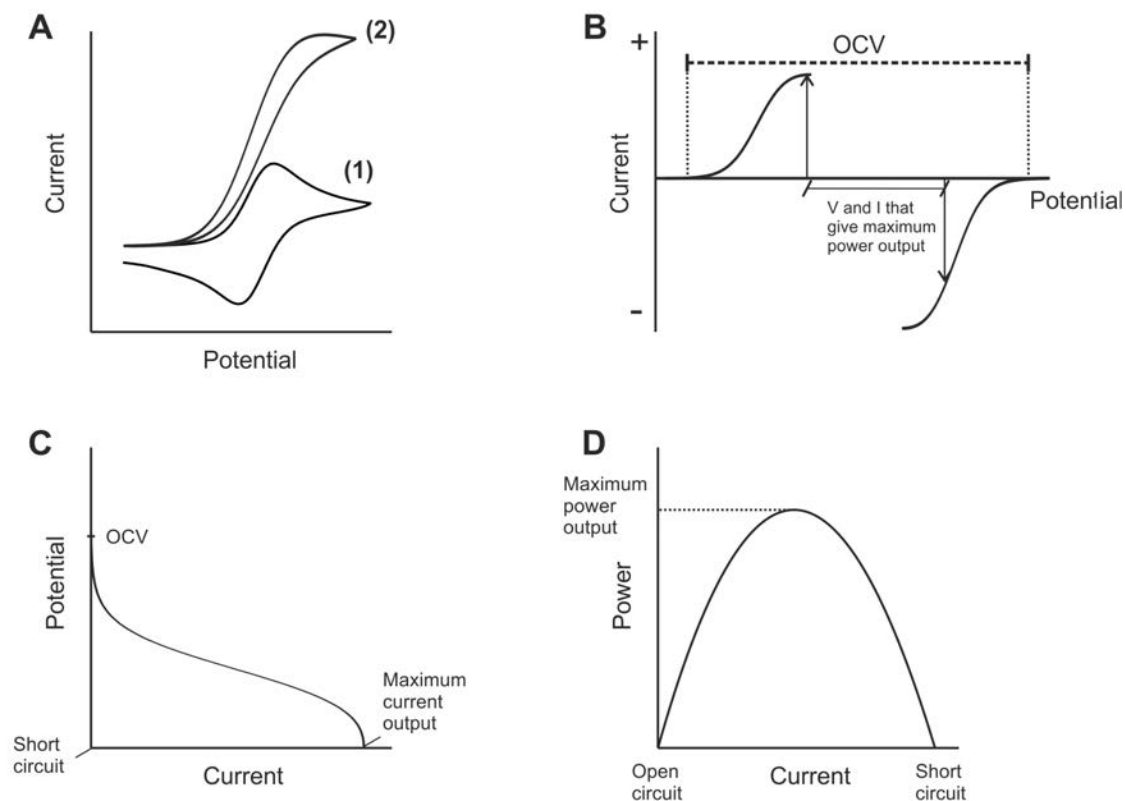


Figure 1.10: Examples of the plots obtained in a voltammetric characterization of the enzymatic fuel cell. (A) Cyclic voltammograms obtained for a biosensor under substrate saturation and non-saturation conditions. (B) Linear voltammograms of an operating anode and cathode. (C) Polarization curves of a fuel cell starting at OCV and ending at short circuit. (D) Power curve derived from the polarization sweep.

defined by the voltage and current extracted at maximum power. However, enzymatic fuel cells rarely operate at these optimal conditions.⁷²

1.3.2 Self-powered biosensors

Enzymatic fuel cells are not only capable of generating a power output upon reaction with the analyte or fuel, but they also do so proportionally to the amount of fuel present in the solution.⁷³ On the one hand, an increase in the OCV is observed for higher analyte concentrations as the rate of the enzymatic reaction at the anode increases and with that the amount of reduced redox mediator—in the case of a second-generation glucose biosensor—which shifts the redox potential of the half cell toward lower values. And, on the other hand, larger currents are generated, also as a consequence of the higher enzymatic reaction. This is the working principle of self-powered biosensors, which no longer require the use of external power sources to trigger the enzymatic reactions that quantify

the concentration of an analyte.⁷⁴

Self-powered sensors may no longer need a potentiostat, but some form of instrumentation must be implemented for signal processing in order to have a quantitative result of the analyte concentration. Current electronic devices require voltages at least around 0.4–0.5 V to operate, a requirement that the first self-powered devices were not able to achieve. Most efforts done in the field of self-powered electrochemical biosensors have focused on achieving larger OCVs and electric currents that are also sustainable in time by optimizing the design of the electrochemical cells, biosensors, and materials.⁷⁵

In this thesis, the required signal processing instrumentation is substituted by an electrochromic material that has a double role. On the one hand, it acts as power source or cathode, enabling the enzymatic reaction at the anode. On the other hand, thanks to the geometry of both electrodes, it can also act as a visual readout, giving quantitative information about the concentration of the analyte/fuel present in the system. This approach represents a breakthrough for self-powered sensors, extending the application of electrochromic materials beyond smart windows⁷⁶ and displays,⁷⁷ into sensing and quantification.

1.4 Electrochromic sensors

When an electroactive species undergoes electrochemical reaction, the ensuing electron exchange is necessarily accompanied by a change in spectral properties, due to the electron promotion between different energetic states in the molecule or atom. If these spectroscopic changes occur in the region of wavelengths that falls in the visible range, a colour change is observed in a phenomenon known as *electrochromism*.⁷⁸

Electrochromic materials have the ability to present different optical properties as a function of the electrochemical potential (Figure 1.11).⁷⁹ The majority of their applications are in the construction of smart glasses, anti-glare mirrors, and low-power displays.⁸⁰ However, their impact in electroanalysis has been limited despite the fact that electrochromic materials are already at the heart of many electroanalytical works. This can be explained on the grounds that developing electrochromic sensors requires the use of spectroelectrochemical equipment which, compared to the potentiostats used in most electroanalytical methods, are relatively more costly and complex. Nevertheless, current mobile phones have made spectrophotometric instrumentation much more accessible, transforming the landscape of point-of-care devices.⁸¹ As discussed below, one key advantage of electrochromic sensors is the possibility to have an optical readout directly out of the sensor, without physical interfaces between the sensing unit and the data processing unit, which leads to a considerable simplification in the construction of the analytical device.

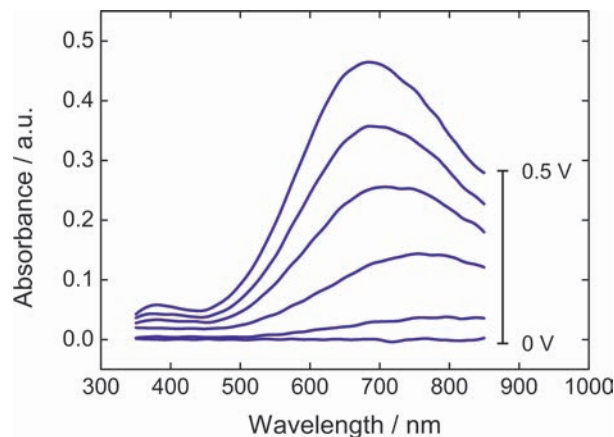


Figure 1.11: Spectroelectrochemical behavior of an electrochromic film in the visible range for different applied electric potentials. The oxidized state is coloured while the reduced state is bleached.

1.4.1 Electrochromic materials

As explained above, many electroactive species exhibit a change in the absorption band as a consequence of a redox reaction where they undergo oxidation or reduction.⁸² This includes, among others, redox mediators typically used in biosensing applications (ferrocyanide, TMPD, PMS...),⁴⁹ conducting polymers such as PEDOT, PANI and PPy which are often used as entrapment matrices for various bioreceptors,⁸³ or metal oxides as WO_3 and NiO, widely used in the construction of gas sensors.⁸⁴

Electrochromic materials can be classified according to their chemical nature,⁸⁵ however, from a device fabrication point of view, it is preferred to classify them based on the solubility of their redox states:^{80,86}

Type I materials. Include those that are soluble in both the reduced and the oxidized state, e.g. methyl viologen (MV), ferro/ferricyanide...

Type II materials. Include those that are soluble only in one redox state, but form a solid film on the surface of an electrode following electron transfer, e.g. heptyl viologen (HV).

Type III materials. Include those that are solid in all redox states, e.g. Prussian Blue, WO_3 , conjugated conducting polymers...

Depending on the application of the electrochrome, some particular performance characteristics will be required. However, in most situations it is required that the materials display a high colour intensity (*contrast ratio*), a fast change between the bleached and colour states (*response time*), a high amount of colour formed with the consumed charge (*colouration efficiency*), or a high stability under a switching regime (*cycle life*).⁸⁰ This parameters will be further discussed in Chapter 5.

Current electroanalytical devices aim at being low-cost and portable devices which should also be built with a reagent-less design. Therefore, type III electrochromic materials seem most suitable for the development of these devices, something reflected in most of the works described in the literature (see Table 1.1).

| Construction | Power source | Display | Electrochrome | Analyte |
|--------------|------------------|-----------------|------------------|---|
| Sandwich | Potentiostat | Colour tone | WO ₃ | Na ⁺ ⁸⁷ |
| Sandwich | Potentiostat | Colour tone | PANI | NH ₄ ⁺ ⁸⁸ |
| Sandwich | Potentiostat | Colour tone | PANI | Ascorbic acid ⁸⁹ |
| Sandwich-BPE | Potentiostat | Colour tone | PB | Ascorbic-Glucose ⁹⁰ |
| Sandwich-BPE | Potentiostat | Colour tone | MV | Lactate-Glucose-Uric acid ⁹¹ |
| Sandwich-BPE | Battery | Colour tone | MV | Various analytes ⁹² |
| Sandwich | Battery | Colour tone | PB | Glucose/H ₂ O ₂ ⁹³ |
| Sandwich | Battery | Colour tone | PB | Lactate ⁹⁴ |
| Sandwich | Self-powered | Colour tone | PB | AFP ⁹⁵ |
| Sandwich | Self-powered | Colour tone | PB | Ascorbic acid ⁹⁶ |
| Sandwich | Self-powered PEC | Colour tone | PB | Glucose ⁹⁷ |
| Sandwich | Self-powered PEC | Colour tone | PB | Glycoprotein (RNase B) ⁹⁸ |
| Sandwich | Self-powered PEC | Colour tone | PB | S ²⁻ ⁹⁹ |
| Sandwich | Self-powered PEC | Colour tone | PB | Phosphate ¹⁰⁰ |
| Sandwich | Self-powered PEC | Colour tone | WO ₃ | Phosphosphate ¹⁰¹ |
| Coplanar | Potentiostat | Colour tone | IrO _x | Chlorpyrifos ¹⁰² |
| Coplanar | Potentiostat | Colour tone | PANI | Cu ²⁺ ¹⁰³ |
| Coplanar-BPE | Potentiostat | Colour tone | PB | CEA ¹⁰⁴ |
| Coplanar | Potentiostat | Colour gradient | PB/PANI | iR drop ¹⁰⁵ |
| Coplanar | Battery | Colour gradient | PB/PANI | pH ¹⁰⁶ |
| Coplanar | Self-powered | Colour tone | MG | Glucose ¹⁰⁷ |
| Coplanar-BPE | Self-powered | Colour tone | PB | Glucose ¹⁰⁸ |

Table 1.1: Main recent works featuring electrochromic sensors.

1.4.2 Power sources in electrochromic sensors

Because electrochromism is a potential dependent phenomenon, electrochromic sensors can be driven by a simple power source, which considerably simplifies its construction. Two main categories of electrochromic sensors can be distinguished depending on the power source used: sensors powered externally, and self-powered sensors.

Externally powered sensors

The obvious way to control an electrochromic sensor is by using a potentiostat,¹⁰² but examples can also be found where the sensor relies on the use of batteries⁹³ and fuel cells.¹⁰⁷

In this first group of sensors, the electrochrome acts as a reporter of the sensing reaction taking place at the electrochemical cell, providing a "yes/no" type of answer if the analyte is present in the sample,^{93,97} or a quantitative response that can be read by either the naked eye¹⁰⁶ or may require the use of an external detection system that can analyze the change in the colour tone of the electrochromic material.^{107,108}

The use of an independent power source as a potentiostat makes the sensor more robust, and allows to have a better control on the performance of the electrochrome, e.g. electrochromic species with more than one coloured state in a short potential window may require an accurate control of the applied potential. However, as seen in Table 1.1, this is not the case for most electrochromes used in analytical devices, which rely on electrochromic materials as metal oxides⁷⁶ or Prussian Blue,¹⁰⁹ which exhibit only two coloured states in a wide potential window. For this, most recent works simplify the construction of the devices by using integrated batteries or fuel cells as power sources along the sensor.

A particular case of externally powered sensors are those based on the use of bipolar electrodes (BPE).¹¹⁰ BPEs are able to maintain a potential difference over their surface, enabling the coexistence of different reactions at its ends. The more traditional set up requires the use of three electrodes,⁹² in which two electrodes generate the potential difference required by the BPE, which is placed in the electric field between them and in contact with the electrolyte. However, this construction can be further simplified to a single-electrode cell where the potential difference is applied directly at the ends of the bipolar electrode.¹¹¹

Self-powered sensors

A higher degree of integration is obtained when the functions of power-source, sensing unit, and display are integrated in a single electrochemical cell.

Self-powered electrochromic sensors rely on the use of electrochromic materials not

only as a reporting agent, but also a power source of the sensing reaction.⁹⁶ The difference in potential between the electrochromic material and a chemical species in the sensing electrode, e.g. redox mediator or the active site of an enzyme, leads to a positive cell voltage, thus triggering the sensing reaction.

BPEs can also lead to self-powered systems.¹⁰⁸ This can be achieved by chemically modifying each end of the bipolar electrode so no external driving potential is needed to trigger the reactions, showing how simple the construction of an electrochromic sensor can be.

One last type of self-powered electrochromic sensors are those based on photoelectrochemical systems (PEC) that rely on the photoreaction of the analyte at one electrode that is powered by an electrochromic material placed at the other electrode.^{97,100}

An interesting feature of these self-powered electrochromic sensors is that, even though the power generated is quite low, in the range of $\mu\text{W cm}^{-2}$, compared to current electrochemical self-powered devices,⁷⁵ the system can still work and provide a result as long as the electric potential of the electrochrome is adequate, as will be discussed in the following chapters. The benefits of having a system able to deliver higher power levels come in the form of faster response times, and the ability, perhaps, to power additional electric components

1.4.3 Device construction

The construction of electrochromic sensors is similar to that of common electrochromic devices. Two main setups can be used to construct these electrochromic devices. The first one, and also most common, known as “sandwich” or “parallel-plate” configuration, consists of two electrodes facing each other, with at least one of them being a transparent electrode fabricated with materials such as PEDOT:PSS,¹¹² tin-oxide derivatives as ITO or FTO,¹¹³ or thin layers of carbon or metallic nanostructures¹¹⁴ (Figure 1.12A). In addition to the electrochromic material, the device should also incorporate an electrolyte that acts as an ionic conductor transporting the electric charge between the two electrodes, and a charge storage layer, that can also be a second electrochrome,¹¹⁵ used to compensate the unbalanced charges when an electric potential is being applied. The second possible arrangement, known as “coplanar” or “interdigitated” configuration,¹¹⁶ consists also of two electrodes, but in this case they are placed in the same horizontal plane, as depicted in Figure 1.12B.

The transition from electrochromic devices to electrochromic sensors is quite simple as the same components must be used, with the exception of the charge storage layer, that is substituted by the (bio)sensing layer which, not only helps balance the charge distribution inside the cell, but also reacts selectively with the analyte.

Conventional electrochromic devices seem to prefer the sandwich configuration since,

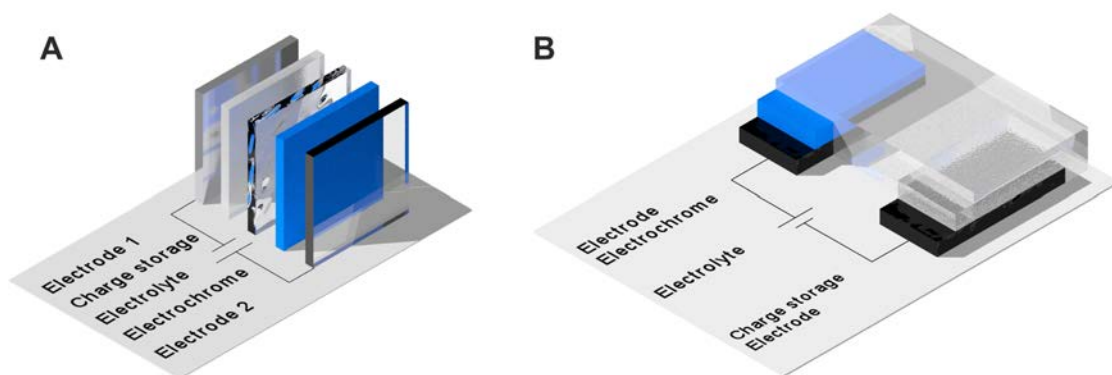


Figure 1.12: Schematic representation of the two main architectures used in the construction of electrochromic devices. (A) Sandwich or parallel-plate. (B) Coplanar or interdigitated.

due to the small gap of roughly a few microns between electrodes, ohmic losses are minimized, and fast and homogeneous colour switches are observed. Nevertheless, reported electrochromic sensors tend to present an equal distribution between sandwich and coplanar arrangements (Table 1.1).

Information display

The main difference between sandwich and coplanar configurations refers to how the colour change takes place. As explained above, the sandwich configuration minimizes the internal resistance between the two electrodes, so a homogeneous and fast switch of the electrochromic display is observed. When a sensing reaction is coupled, a uniform discolouration is observed in the electrochromic display. This variation in the colour tone can be analyzed with the aid of an external reader, and related to the amount of analyte present in the sample. However, in coplanar geometries the internal resistance is not minimized and, depending on the design of the cell and the selected supporting electrolyte, can lead to gradients in the colour switch of the display instead of presenting a homogeneous discolouration as in the case of sandwich electrodes. This colour gradient can be used as a metering bar to quantify the charge that is flowing through the electrochromic material,¹⁰⁵ and can also be related to the analyte concentration in a sample when coupled to an enzymatic biosensor.

Although detection can be made by the naked eye in both display arrangements, only the use of coplanar electrodes allows to obtain a naked eye semi-quantitative measurement of the analyte concentration. As shown in Table 1.1, the use of coplanar electrodes to develop a colour gradient has been essentially neglected in all electrochromic sensing devices reported in the literature. This principle has been exploited throughout this thesis to develop the experimental work.

Bibliography

- [1] Bard, A. J.; Faulkner, L. R. *Electrochemical methods: fundamentals and applications*; John Wiley & Sons, New York, 2001.
- [2] Banks, C. E.; Davies, T. J.; Evans, R. G.; Hignett, G.; Wain, A. J.; Lawrence, N. S.; Wadhawan, J. D.; Marken, F.; Compton, R. G. Electrochemistry of immobilised redox droplets: Concepts and applications. *Phys. Chem. Chem. Phys.* **2003**, *5*, 4053–4069.
- [3] Heinze, J. Ultramicroelectrodes in electrochemistry. *Angew. Chem. Int. Ed.* **1993**, *32*, 1268–1288.
- [4] Marcus, R. A.; Sutin, N. Electron transfers in chemistry and biology. *Biochim. Biophys. Acta* **1985**, *811*, 265–322.
- [5] Inzelt, G.; Lewenstam, A.; Scholz, F. *Handbook of reference electrodes*; Springer, New York, 2013.
- [6] Albery, J. W. *Electrode kinetics*; Oxford University Press, Oxford, 1975; Vol. 14.
- [7] Compton, R. G.; Banks, C. E. *Understanding voltammetry*; Imperial College Press, London, 2011.
- [8] Scholz, F. *Electroanalytical methods*; Springer, Berlin, 2010.
- [9] Marcus, R. A. On the theory of oxidation-reduction reactions involving electron transfer. i. *J. Chem. Phys.* **1956**, *24*, 966–978.
- [10] Marcus, R. A. Electron transfer at electrodes and in solution: comparison of theory and experiment. *Electrochim. Acta* **1968**, *13*, 995–1004.
- [11] Hush, N. S. Adiabatic rate processes at electrodes. I. Energy-charge relationships. *J. Chem. Phys.* **1958**, *28*, 962–972.
- [12] Hush, N. S. Homogeneous and heterogeneous optical and thermal electron transfer. *Electrochim. Acta* **1968**, *13*, 1005–1023.
- [13] Newman, J.; Thomas-Alyea, K. E. *Electrochemical systems*; John Wiley & Sons, New Jersey, 2004.
- [14] Fick, A. Uber diffusion. *Journal of Science* **1855**, *16*.
- [15] Selman, J. R.; Tobias, C. W. *Mass-transfer measurements by the limiting-current technique*; Elsevier, Amsterdam, 1978; Vol. 10; pp 211–318.

- [16] Dickinson, E. J. F.; Limon-Petersen, J. G.; Rees, N. V.; Compton, R. G. How much supporting electrolyte is required to make a cyclic voltammetry experiment quantitatively “diffusional”? A theoretical and experimental investigation. *J. Phys. Chem. C* **2009**, *113*, 11157–11171.
- [17] Wang, J. *Analytical electrochemistry*; John Wiley & Sons, New Jersey, 2006.
- [18] Cottrell, F. G. Residual current in galvanic polarization regarded as a diffusion problem. *Z. Phys. Chem* **1903**, *42*, 385–431.
- [19] Elgrishi, N.; Rountree, K. J.; McCarthy, B. D.; Rountree, E. S.; Eisenhart, T. T.; Dempsey, J. L. A practical beginner’s guide to cyclic voltammetry. *J. Chem. Educ.* **2017**, *95*, 197–206.
- [20] Kissinger, P. T.; Heineman, W. R. Cyclic voltammetry. *J. Chem. Educ.* **1983**, *60*, 702–706.
- [21] Nicholson, R. S. Theory and application of cyclic voltammetry for measurement of electrode reaction kinetics. *Anal. Chem.* **1965**, *37*, 1351–1355.
- [22] Savéant, J.; Tessier, D. Convolution potential sweep voltammetry Part IV. Homogeneous follow-up chemical reactions. *J. Electroanal. Chem.* **1975**, *61*, 251–263.
- [23] Lavagnini, I.; Antiochia, R.; Magno, F. An extended method for the practical evaluation of the standard rate constant from cyclic voltammetric data. *Electroanalysis* **2004**, *16*, 505–506.
- [24] Matsuda, H.; Ayabe, Y. Zur theorie der Randles-Sevčičschen kathodenstrahlpolarographie. *Z. Electrochem* **1955**, *59*, 494–503.
- [25] Laviron, E. The use of linear potential sweep voltammetry and of a.c. voltammetry for the study of the surface electrochemical reaction of strongly adsorbed systems and of redox modified electrodes. *J. Electroanal. Chem. Interfacial Electrochem.* **1979**, *100*, 263–270.
- [26] Kaim, W.; Fiedler, J. Spectroelectrochemistry: the best of two worlds. *Chem. Soc. Rev.* **2009**, *38*, 3373–3382.
- [27] Garoz-Ruiz, J.; Guillen-Posteguillo, C.; Colina, A.; Heras, A. Application of spectroelectroanalysis for the quantitative determination of mixtures of compounds with highly overlapping signals. *Talanta* **2019**, *195*, 815–821.
- [28] Zhai, Y.; Zhu, Z.; Zhou, S.; Zhu, C.; Dong, S. Recent advances in spectroelectrochemistry. *Nanoscale* **2018**, *10*, 3089–3111.

- [29] Ashley, K.; Pons, S. Recent advances in UV-visible reflectance spectroelectrochemistry. *Trends in Analytical Chemistry* **1986**, *5*, 263–268.
- [30] Ash, P. A.; Vincent, K. A. Spectroscopic analysis of immobilised redox enzymes under direct electrochemical control. *ChemComm* **2012**, *48*, 1400–1409.
- [31] Ibañez, D.; Santidrian, A.; Heras, A.; Kalbáč, M.; Colina, A. Study of adenine and guanine oxidation mechanism by surface-enhanced Raman spectroelectrochemistry. *J. Phys. Chem. C* **2015**, *119*, 8191–8198.
- [32] Bussy, U.; Giraudeau, P.; Silvestre, V.; Jaunet-Lahary, T.; Ferchaud-Roucher, V.; Krempf, M.; Akoka, S.; Tea, I.; Boujtita, M. In situ NMR spectroelectrochemistry for the structure elucidation of unstable intermediate metabolites. *Anal. Bioanal. Chem.* **2013**, *405*, 5817–5824.
- [33] Farley, N.; Gurman, S.; Hillman, A. Simple cell for in situ X-ray absorption spectroelectrochemistry. *Electrochem. Comm.* **1999**, *1*, 449–452.
- [34] Zhang, X.; Jun, H.; Wang, J. *Electrochemical sensors, biosensors and their biomedical applications*; Academic Press, London, 2007.
- [35] Skoog, D. A.; Holler, F. J.; Nieman, T. A. *Principles of instrumental analysis*; McGraw-Hill, New York, 2000.
- [36] Amatore, C.; Savéant, J.; Thiebault, A. Electrochemically induced chemical reactions kinetics of competition with electron transfer. *J. Electroanal. Chem.* **1979**, *103*, 303–320.
- [37] Janata, J. *Principles of chemical sensors*; Springer, London, 2009.
- [38] Zhu, C.; Yang, G.; Li, H.; Du, D.; Lin, Y. Electrochemical sensors and biosensors based on nanomaterials and nanostructures. *Anal. Chem.* **2015**, *87*, 230–249.
- [39] Organization, W. H. <https://www.who.int/mediacentre/factsheets/fs138/en/>.
- [40] Wang, J. Glucose biosensors: 40 years of advances and challenges. *Electroanalysis* **2001**, *13*, 983–988.
- [41] Wang, J. Electrochemical glucose biosensors. *Chem. Rev.* **2008**, *108*, 814–825.
- [42] Turner, A.; Karube, I.; Wilson, G. *Biosensors. Fundamentals and applications*; Oxford University Press, New York, 1987.
- [43] Ronkainen, N. J.; Halsall, H. B.; Heineman, W. R. Electrochemical biosensors. *Chem. Soc. Rev.* **2010**, *39*, 1747–1763.

- [44] Wilson, R.; Turner, A. P. F. Glucose oxidase: an ideal enzyme. *Biosens. Bioelectron.* **1992**, *7*, 165–185.
- [45] Clark, L. C.; Lyons, C. Electrode systems for continuous monitoring in cardiovascular surgery. *Ann. N. Y. Acad. Sci.* **1962**, *102*, 29–45.
- [46] Gamburzev, S.; Atanasov, P.; Wilkins, E. Performance of glucose biosensor based on oxygen electrode in physiological fluids and at body temperature. *Sens. Actuators B Chem.* **1996**, *30*, 179–183.
- [47] Schläpfer, P.; Mindt, W.; Racine, P. H. Electrochemical measurement of glucose using various electron acceptors. *Clin. Chim. Acta* **1974**, *57*, 283–289.
- [48] Habermüller, K.; Mosbach, M.; Schuhmann, W. Electron-transfer mechanisms in amperometric biosensors. *Fresenius J. Anal. Chem.* **2000**, *366*, 560–568.
- [49] Kausaite-Minkstimiene, A.; Mazeiko, V.; Ramanaviciene, A.; Oztekin, Y.; Solak, A. O.; Ramanavicius, A. Evaluation of some redox mediators in the design of reagentless amperometric glucose biosensor. *Electroanalysis* **2014**, *26*, 1528–1535.
- [50] Pumera, M.; Sánchez, S.; Ichinose, I.; Tang, J. Electrochemical nanobiosensors. *Sens. Actuators B Chem.* **2007**, *123*, 1195–1205.
- [51] Lötzbeyer, T.; Schuhmann, W.; Schmidt, H.-L. Electron transfer principles in amperometric biosensors: direct electron transfer between enzymes and electrode surface. *Sens. Actuators B Chem.* **1996**, *33*, 50–54.
- [52] Grieshaber, D.; MacKenzie, R.; Vörös, J.; Reimhult, E. Electrochemical biosensors - Sensor principles and architectures. *Sensors* **2008**, *8*, 1400–1458.
- [53] Minteer, S. D. *Enzyme stabilization and immobilization. Methods and protocols*; Springer, New York, 2017.
- [54] Sassolas, A.; Blum, L. J.; Leca-Bouvier, B. D. Immobilization strategies to develop enzymatic biosensors. *Biotechnol. Adv.* **2012**, *30*, 489–511.
- [55] O’Sullivan, C.; Tompson, F. W. Invertase: a contribution to the history of an enzyme or unorganised ferment. *J. Chem. Soc., Trans.* **1890**, *57*, 834–931.
- [56] Michaelis, L.; Menten, M. L. Die kinetik der invertinwirkung. *Biochem. Z.* **1913**, *49*, 333–369.
- [57] Briggs, G. E.; Haldane, J. B. S. A note on the kinetics of enzyme action. *Biochem. J.* **1925**, *19*, 338–339.

- [58] Battaglini, F.; Calvo, E. J. Digital simulation of homogeneous enzyme kinetics for amperometric redox-enzyme electrodes. *Anal. Chim. Acta* **1992**, *258*, 151–160.
- [59] Grove, W. On voltaic series and the combination of gases by platinum. *Phil. Mag. J. Sci.* **1836**, *14*, 127–130.
- [60] Schoenbein, C. F. On the voltaic polarization of certain solid and fluid substances. *Phil. Mag.* **1839**, *14*, 43–45.
- [61] Steele, B. C. H.; Heinzl, A. Materials for fuel-cell technologies. *Nature* **2001**, *414*, 345–352.
- [62] Minteer, S. D.; Liaw, B. Y.; Cooney, M. J. Enzyme-based biofuel cells. *Curr. Opin. Biotechnol.* **2007**, *18*, 228–234.
- [63] Cracknell, J. A.; Vincent, K. A.; Armstrong, F. A. Enzymes as working or inspirational electrocatalysts for fuel cells and electrolysis. *Chem. Rev.* **2008**, *108*, 2439–2461.
- [64] Yahiro, A. T.; Lee, S. M.; Kimble, D. O. Bioelectrochemistry: I. Enzyme utilizing bio-fuel cell studies. *Biochim. Biophys. Acta* **1964**, *88*, 375–383.
- [65] Katz, E.; MacVittie, K. Implanted biofuel cells operating in vivo – methods, applications and perspectives – feature article. *Energy Environ. Sci.* **2013**, *6*, 2791–2803.
- [66] Falk, M.; Andoralov, V.; Blum, Z.; Sotres, J.; Suyatin, D. B.; Ruzgas, T.; Arnebrant, T.; Shleev, S. Biofuel cell as a power source for electronic contact lenses. *Biosens. Bioelectron.* **2012**, *37*, 38–45.
- [67] Meredith, M. T.; Minteer, S. D. Biofuel cells: enhanced enzymatic bioelectrocatalysis. *Annu. Rev. Anal. Chem.* **2012**, *5*, 157–179.
- [68] Gonzalez-Solino, C.; Lorenzo, M. Enzymatic fuel cells: towards self-powered implantable and wearable diagnostics. *Biosensors* **2018**, *8*, 11–29.
- [69] Bandodkar, A. J. Review—Wearable biofuel cells: past, present and future. *J. Electrochem. Soc.* **2017**, *164*, H3007–H3014.
- [70] Cooney, M. J.; Svoboda, V.; Lau, C.; Martin, G.; Minteer, S. D. Enzyme catalysed biofuel cells. *Energy Environ. Sci.* **2008**, *1*, 320–337.
- [71] Mano, N.; de Poulpiquet, A. O₂ reduction in enzymatic biofuel cells. *Chem. Rev.* **2018**, *118*, 2392–2468.

- [72] Luckarift, H. R.; Atanassov, P. B.; Johnson, G. R. *Enzymatic fuel cells. From fundamentals to applications*; John Wiley & Sons, New Jersey, 2014.
- [73] Katz, E.; Bückmann, A. F.; Willner, I. Self-powered enzyme-based biosensors. *J. Am. Chem. Soc.* **2001**, *123*, 10752–10753.
- [74] Conzuelo, F.; Ruff, A.; Schuhmann, W. Self-powered bioelectrochemical devices. *Curr. Opin. Electrochem.* **2018**, <https://doi.org/10.1016/j.coelec.2018.05.010>.
- [75] Grattieri, M.; Minter, S. D. Self-powered biosensors. *ACS Sens.* **2018**, *3*, 44–53.
- [76] Granqvist, C. G. Electrochromics for smart windows: oxide-based thin films and devices. *Thin Solid Films* **2014**, *564*, 1–38.
- [77] Mortimer, R. J.; Dyer, A. L.; Reynolds, J. R. Electrochromic organic and polymeric materials for display applications. *Displays* **2006**, *27*, 2–18.
- [78] Platt, J. R. Electrochromism, a possible change of color producible in dyes by an electric field. *J. Chem. Phys.* **1961**, *34*, 862–863.
- [79] Mortimer, R. J.; Rosseinsky, D. R.; Monk, P. M. *Electrochromic materials and devices*; Wiley-VCH, Weinheim, 2015.
- [80] Mortimer, R. J. Electrochromic materials. *Annu. Rev. Mater. Res.* **2011**, *41*, 241–268.
- [81] Xu, X.; Akay, A.; Wei, H.; Wang, S.; Pinguan-Murphy, B.; Erlandsson, B.-E.; Li, X.; Lee, W.; Hu, J.; Wang, L.; Xu, F. Advances in smartphone-based point-of-care diagnostics. *Proc. IEEE* **2015**, *103*, 236–247.
- [82] Monk, P. M.; Mortimer, R. J.; Rosseinsky, D. R. *Electrochromism: fundamentals and applications*; VCH, Weinheim, 1995.
- [83] Cosnier, S. Biomolecule immobilization on electrode surfaces by entrapment or attachment to electrochemically polymerized films. A review. *Biosensors and Bioelectronics* **1999**, *14*, 443–456.
- [84] Wang, C.; Yin, L.; Zhang, L.; Xiang, D.; Gao, R. Metal oxide gas sensors: sensitivity and influencing factors. *Sensors* **2010**, *10*, 2088–2106.
- [85] Mortimer, R. J. Electrochromic materials. *Chem. Soc. Rev.* **1997**, *26*, 147–156.
- [86] Chang, I.; Gilbert, B.; Sun, T. Electrochemichromic systems for display applications. *J. Electrochem. Soc.* **1975**, *122*, 955–962.

- [87] De Matteis, V.; Cannavale, A.; Blasi, L.; Quarta, A.; Gigli, G. Chromogenic device for cystic fibrosis precocious diagnosis: A “point of care” tool for sweat test. *Sens. Actuators B Chem.* **2016**, *225*, 474–480.
- [88] Virbickas, P.; Valiūnienė, A.; Ramanavičius, A. Towards electrochromic ammonium ion sensors. *Electrochem. Comm.* **2018**, *94*, 41–44.
- [89] Porcel-Valenzuela, M.; Ballesta-Claver, J.; de Orbe-Payá, I.; Montilla, F.; Capitan-Vallvey, L. F. Disposable electrochromic polyaniline sensor based on a redox response using a conventional camera: a first approach to handheld analysis. *J. Electroanal. Chem.* **2015**, *738*, 162–169.
- [90] Yu, X.; Liang, J.; Yang, T.; Gong, M.; Xi, D.; Liu, H. A resettable and reprogrammable keypad lock based on electrochromic Prussian Blue films and biocatalysis of immobilized glucose oxidase in a bipolar electrode system. *Biosens. Bioelectron.* **2018**, *99*, 163–169.
- [91] Xu, W.; Fu, K.; Bohn, P. W. Electrochromic sensor for multiplex detection of metabolites enabled by closed bipolar electrode coupling. *ACS Sensors* **2017**, *2*, 1020–1026.
- [92] Xu, W.; Fu, K.; Ma, C.; Bohn, P. W. Closed bipolar electrode-enabled dual-cell electrochromic detectors for chemical sensing. *Analyst* **2016**, *141*, 6018–6024.
- [93] Liu, H.; Crooks, R. M. Paper-based electrochemical sensing platform with integral battery and electrochromic read-out. *Anal. chem.* **2012**, *84*, 2528–2532.
- [94] Zhang, F.; Cai, T.; Ma, L.; Zhan, L.; Liu, H. A paper-based electrochromic array for visualized electrochemical sensing. *Sensors* **2017**, *17*, 276.
- [95] Yu, Z.; Cai, G.; Ren, R.; Tang, D. A new enzyme immunoassay for alpha-fetoprotein in a separate setup coupling an aluminium/Prussian blue-based self-powered electrochromic display with a digital multimeter readout. *Analyst* **2018**, *143*, 2992–2996.
- [96] Zloczewska, A.; Celebanska, A.; Szot, K.; Tomaszewska, D.; Opallo, M.; Jönsson-Niedziolka, M. Self-powered biosensor for ascorbic acid with a Prussian blue electrochromic display. *Biosens. Bioelectron.* **2014**, *54*, 455–461.
- [97] Peimanifard, Z.; Rashid-Nadimi, S. Light-powered cell for detection of glucose with the naked eye. *Electrochem. Comm.* **2017**, *79*, 37–40.

- [98] Gao, C.; Wang, Y.; Yuan, S.; Xue, J.; Cao, B.; Yu, J. Engineering anatase hierarchically cactus-like TiO₂ arrays for photoelectrochemical and visualized sensing platform. *Biosens. Bioelectron.* **2017**, *90*, 336–342.
- [99] Wang, Y.; Ge, S.; Zhang, L.; Yu, J.; Yan, M.; Huang, J. Visible photoelectrochemical sensing platform by in situ generated CdS quantum dots decorated branched-TiO₂ nanorods equipped with Prussian blue electrochromic display. *Biosens. Bioelectron.* **2017**, *89*, 859–865.
- [100] Wang, Y.; Zhang, L.; Cui, K.; Xu, C.; Li, H.; Liu, H.; Yu, J. Solar driven electrochromic photoelectrochemical fuel cells for simultaneous energy conversion, storage and self-powered sensing. *Nanoscale* **2018**, *10*, 3421–3428.
- [101] Yang, Q.; Hao, Q.; Lei, J.; Ju, H. Portable photoelectrochemical device integrated with self-powered electrochromic tablet for visual analysis. *Anal. Chem.* **2018**, *90*, 3703–3707.
- [102] Capoferri, D.; Álvarez Diduk, R.; Carlo, M. D.; Compagnone, D.; Merkoçi, A. Electrochromic molecular imprinting sensor for visual and smartphone-based detections. *Anal. Chem.* **2018**, *90*, 5850–5856.
- [103] Deshmukh, M. A.; Gicevicius, M.; Ramanaviciene, A.; Shirsat, M. D.; Viter, R.; Ramanavicius, A. Hybrid electrochemical/electrochromic Cu(II) ion sensor prototype based on PANI/ITO-electrode. *Sens. Actuators B Chem.* **2017**, *248*, 527–535.
- [104] Zhai, Q.; Zhang, X.; Xia, Y.; Li, J.; Wang, E. Electrochromic sensing platform based on steric hindrance effects for CEA detection. *Analyst* **2016**, *141*, 3985–3988.
- [105] Liana, D. D.; Raguse, B.; Gooding, J. J.; Chow, E. Toward paper-based sensors: turning electrical signals into an optical readout system. *ACS Appl. Mater. Interfaces* **2015**, *7*, 19201–19209.
- [106] Chow, E.; Liana, D. D.; Raguse, B.; Gooding, J. J. A potentiometric sensor for pH monitoring with an integrated electrochromic readout on paper. *Aust. J. Chem.* **2017**, *70*, 979.
- [107] Pinyou, P.; Conzuelo, F.; Sliozberg, K.; Vivekananthan, J.; Contin, A.; Pöller, S.; Plumeré, N.; Schuhmann, W. Coupling of an enzymatic biofuel cell to an electrochemical cell for self-powered glucose sensing with optical readout. *Bioelectrochem.* **2015**, *106*, 22–27.

- [108] Zhang, X.; Zhang, L.; Zhai, Q.; Gu, W.; Li, J.; Wang, E. Self-powered bipolar electrochromic electrode arrays for direct displaying applications. *Anal. Chem.* **2016**, *88*, 2543–2547.
- [109] Karyakin, A. A. Prussian blue and its analogues: electrochemistry and analytical applications. *Electroanalysis* **2001**, *13*, 813–819.
- [110] Fosdick, S. E.; Knust, K. N.; Scida, K.; Crooks, R. M. Bipolar electrochemistry. *Angew. Chem. Int. Ed.* **2013**, *52*, 10438–10456.
- [111] Zhang, X.; Shang, C.; Gu, W.; Xia, Y.; Li, J.; Wang, E. A renewable display platform based on the bipolar electrochromic electrode. *ChemElectroChem* **2016**, *3*, 383–386.
- [112] Singh, R.; Tharion, J.; Murugan, S.; Kumar, A. ITO-free solution-processed flexible electrochromic devices based on PEDOT: PSS as transparent conducting electrode. *ACS Appl. Mater. Interfaces* **2016**, *9*, 19427–19435.
- [113] Kumar, A.; Zhou, C. The race to replace tin-doped indium oxide: which material will win? *ACS Nano* **2010**, *4*, 11–14.
- [114] Hecht, D. S.; Hu, L.; Irvin, G. Emerging transparent electrodes based on thin films of carbon nanotubes, graphene, and metallic nanostructures. *Adv. Mater.* **2011**, *23*, 1482–1513.
- [115] Monk, P.; Mortimer, R.; Rosseinsky, D. *Electrochromism and electrochromic materials*; Cambridge University Press, Cambridge, 2007.
- [116] Coleman, J. P.; Lynch, A. T.; Madhukar, P.; Wagenknecht, J. H. Printed, flexible electrochromic displays using interdigitated electrodes. *Sol. Energy Mater. Sol. Cells* **1999**, *56*, 395–418.

2

Methods

This chapter presents the main approaches and experimental methods used in this thesis. First, a brief introduction to rapid prototyping is given, focusing on the techniques applied to the fabrication of the electrochemical devices used. Next, an overview is given of the finite element method and the software used to simulate the electrochromic devices presented in this thesis.

2.1 Rapid prototyping

Some of the recent advances in the development of electroanalytical devices, and particularly in the fields of enzymatic fuel cells and self-powered systems, have been enabled by miniaturization techniques¹⁻³ Disposable and low-cost analytical devices contributing to the decentralization of chemical analysis from traditional laboratories through Point-of-care diagnosis (POC)⁴ are a clear example.

The increasing interest in developing low-cost and miniaturized analytical systems based on microfluidics and microelectromechanics (MEMS) has expanded the use of polymeric materials, leaving behind classic materials such as glass or silicon due to the high-costs and complexity of their processing.⁵

The use of prototyping techniques allows to construct models of a device in an iterative process (Figure 2.1), identifying design flaws, and thus reducing fabrication costs in production.⁶

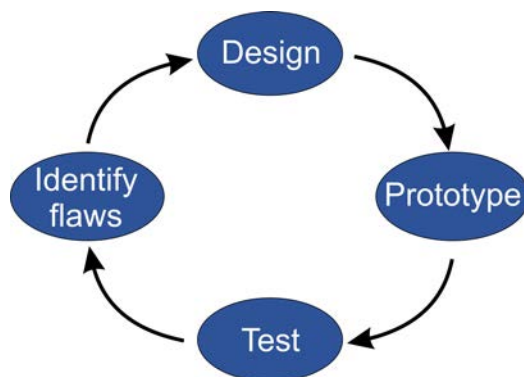


Figure 2.1: Diagram of the iterative process followed in the design of a prototype.

Rapid prototyping techniques include, among others, micromolding,⁷ micromilling,⁸ stereolithography,⁹ embossing,¹⁰ cutting,^{11,12} and printing.¹³ The use of these techniques enables fast modifications in the design of miniaturized analytical devices in order to optimize their performance. The selection of the most adequate prototyping technique is determined by the specific requirements of the device as well as by the materials selected. The analytical devices used here were fabricated using cutting and printing techniques.

2.1.1 Cutting techniques

To design and manufacture the elements of the electrochemical devices, two of the best-known cutting techniques used in rapid prototyping were employed: xurography and laser ablation.

Xurography, or blade cutting,¹¹ has been widely used as a fabrication technique for



(a) Plotter cutter.

(b) CO₂ Laser engraver.

Figure 2.2: Captures of the two different cutting equipment used in the fabrication of the electrochemical devices.

microfluidic analytical devices for the last 10-20 years thanks to its low cost and high operating speed (Figure 2.2A). It consists of a plotter fitted with a razor instead of a pen. The movement of this razor following a certain pattern creates the desired cut on the substrate. The regulation of the applied pressure and motion speed, as well as the selection of the appropriate blade, allows the fabrication of microstructures that, in some cases, can be of up to a few microns,^{11,14} depending on the thickness and hardness of the materials employed, and the blade angle.

Laser ablation¹² on the other hand, relies on the combustion or sublimation of material by action of a CO₂ laser beam in order to create the desired patterns (Figure 2.2B). Similar to xurography, the power and speed of the laser pass can be controlled to produce cuts in the material of different width and depth. However, the minimum line width that can be achieved is limited in our case to around 150-200 μm , a size slightly larger than the laser beam itself (Figure 2.3). Also, a worse definition of the cut line is obtained.¹⁵ The ablation of the material generates an important amount of vapours that must be removed by an extraction system which, added to the more expensive cost of the laser equipment, increases the overall size. Nevertheless, much faster processing speeds are obtained with laser cutting.

2.1.2 Printing techniques

The implementation of printing techniques in the field of electrochemistry back in the 1980s¹⁶ has made screen-printed electrodes (SPEs) an essential tool in a wide variety of electroanalytical laboratories.¹⁷ This is due to the broad availability of conducting and dielectric pastes and inks, as well as the possibility of fabricating and printing virtually any material, which results in very low manufacturing costs. The fabrication of electrodes by

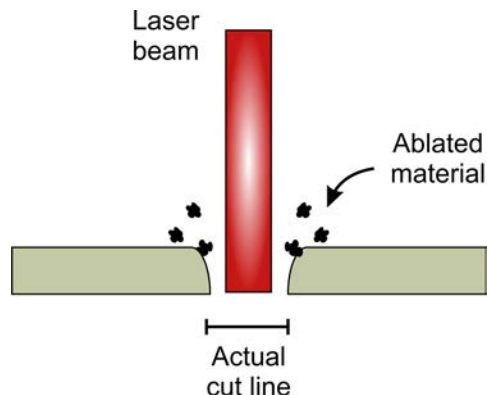


Figure 2.3: Schematic representation of the laser ablation process.

ink-jet printing,^{18,19} on the other hand, is something relatively newer in research environments and it is still quite limited because of the high costs of the required equipment as well as by the limitations in availability and processability of the inks.²⁰ For these reasons, the electrochemical devices presented in this thesis are fabricated using screen rather than ink-jet printing.

Screen-printing techniques are based of forcing a paste through a physical screen. Depending on the nature of that screen, we may distinguish between stencil-printing and (mesh) screen-printing.

Stencil-printed electrodes

One approach to print electrodes is making use of stencils. The stencil, with a predefined cut, is placed on top of the substrate in direct contact with it, allowing the pass of a paste through it. A variety of materials such as paper, wood or metals are used to fabricate stencils, however, the use of plastic materials is predominant above others, and particularly adhesive plastic materials such as PSA or vinyl. In this thesis, PSA was selected to fabricate the stencils, and was cut with a desired pattern using both cutting techniques described above. Figure 2.4 shows a scheme of the fabrication process of the electrodes where a precut in the liner above the adhesive of the PSA was done to define the printing area, and thus transforming the liner of the PSA into a stencil. After applying the conducting material with a squeegee, the rest of the liner is removed so other plastic layers can be assembled.

Thick layers of material are deposited, roughly 50 to 100 μm , and lateral resolutions also within that range can be achieved, as defined by the thickness of the stencil as well as by the width of the cut done in the cutting step.

Stencil-printed electrodes in combination with cutting techniques offer the possibility of manufacturing electrochemical devices in a very accessible manner, with a simple workflow and affordable equipment.



Figure 2.4: Representation of the stencil-printing procedure used with PSA substrates. First, the precut liner is removed, exposing the adhesive layer. Second, the conducting paste is applied with the use of a squeegee. The protecting liner is then removed, revealing the printed surface which is then cured in an oven.

Screen-printed electrodes

An alternative to stencils is the use of meshed screens. These screens consist of a mesh of synthetic fibers that are coated with a negative photocurable emulsion which, after a photolithographic step, reveals the pattern to be printed (Figure 2.5).

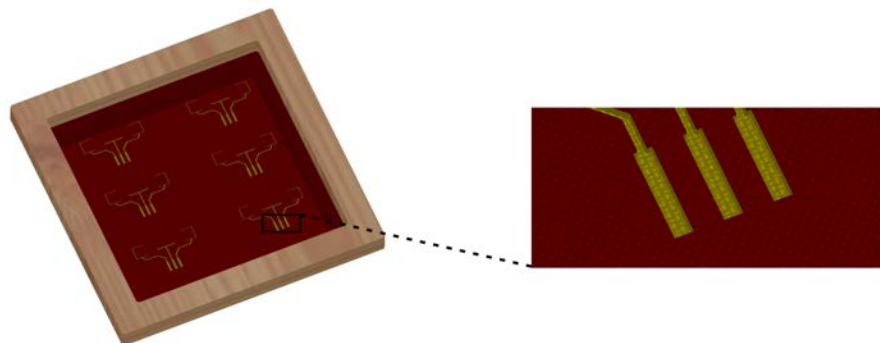


Figure 2.5: Figure of a typical screen with a printing pattern. In the enlarged figure it can be observed the mesh of the screen that the paste goes through.

In contrast to the printing method using stencils, which need to contact the substrate, the screen is not necessarily in contact with it. The distance between the screen and the substrate is known as “snap-off” distance or, simply, “snap-off”. Only when a sufficiently high pressure is applied on it with the squeegee, the mesh of the screen bends to touch the substrate, and the printing material is then deposited, bending back to its original position after the applied pressure is removed. Parameters such as the snap-off distance, applied pressure, squeegee speed or the number of threads per inch in the mesh, may affect the width and thickness of the printed layers, and must be adjusted depending on the nature of the paste to achieve the desired results.²¹ Higher resolutions can be achieved with the use of screens compared to stencil-printed electrodes, as the thickness of the printed layer is roughly between 5 and 10 μm , and also thinner widths down to tens of microns are also

possible changing the material of the threads to a more expensive metallic screen.^{22,23}

In contrast to the stencil-printing where the whole process can be carried out in any available laboratory, the screen-printing process often requires the outsourcing of the fabrication of the screens and the photolithographic step. However, a much higher performance is usually accomplished in terms of manufacturing speed and reusability of the materials.

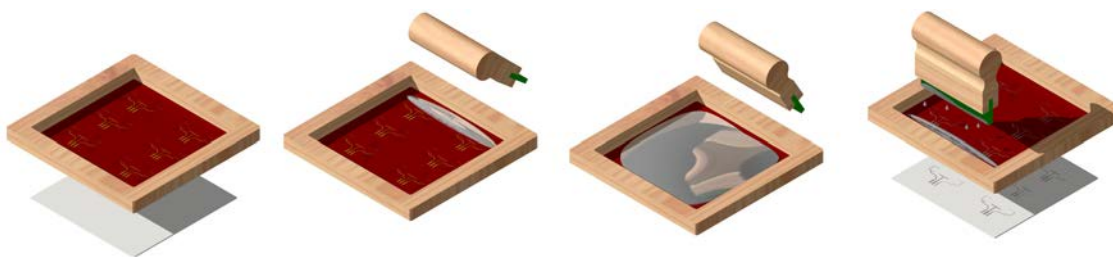


Figure 2.6: Schematic representation of the steps in the printing process. The substrate is placed beneath the screen, with a small snap-off distance. The paste is spread over the screen, filling the cavities of the mesh. Upon application of pressure, the paste is printed on the surface of the substrate.

2.2 Numerical simulation

Numerical simulations are a powerful tool to understand, validate, and predict experimental results. Simulations can help to explore the limitations of an electroanalytical device and also improve its design and performance. Simulations carried out in this thesis involve the resolution of the mass transport equations of electroactive and non-electroactive species in a geometric and time domain representing particular experiments. Mass transport phenomena are described by partial differential equations (PDE) which, in most cases, do not present an analytical solution, and require the use of computational methods.²⁴

In this thesis, commercially available software COMSOL Multiphysics was used to solve the mass transport equations.²⁵ This interface uses the *finite element method* (FEM) as a mathematical solver for the differential equations.²⁶

2.2.1 Finite element method

In order to obtain an approximate solution to the PDE, discrete methods must be implemented by using model equations, which can be solved using numerical methods.²⁷ COMSOL Multiphysics relies of the use of finite element method to solve these PDE.²⁵ FEM consists in the subdivision of a system or domain inside a defined geometry into small parts called finite elements. The numerical model equations of these elements are

solved and then combined to obtain the approximate solution of the whole system. The set of elements in which a domain is subdivided is defined as ‘mesh’. There are different types of elements depending on the space dimensions of the system to be studied, with the most fundamental elements being linear segments for 1D geometries, triangles for 2D geometries or tetrahedrons for 3D geometries.²⁸ The mathematical simulations carried out here were implemented in 2D geometries, which were subdivided into triangular elements. Figure 2.7 shows a typical discretized domain of a solution in contact with an electrode. As seen, the size of the triangular elements varies, becoming smaller in the regions prone to present acute gradients in mass, current or potential, and particularly in the boundary electrode-insulating material.²⁹

The idea of using a discretization method is to approximate the solution of a certain function, u , by another function, u_h , which is composed by a combination of linear basis functions:

$$u_h = \sum_i u_i \psi_i \quad (2.1)$$

where ψ_i represent the basis functions and u_i are the coefficients or degrees of freedom of those functions. The coefficients u_i are the solution values at each vertex of the triangular elements, or ‘nodes’. Each linear basis function take a value of 1 at the nodes of the mesh and 0 at the rest of the points. As the number of elements at the domain increases, also does the number of basis functions, and a more accurate solution is obtained, however, the number of calculations that must be done also increases, and with that the calculation time. For this reason, a good distribution of the elements in the domain becomes essential to optimized the calculation time but maintaining the accuracy of the solution.

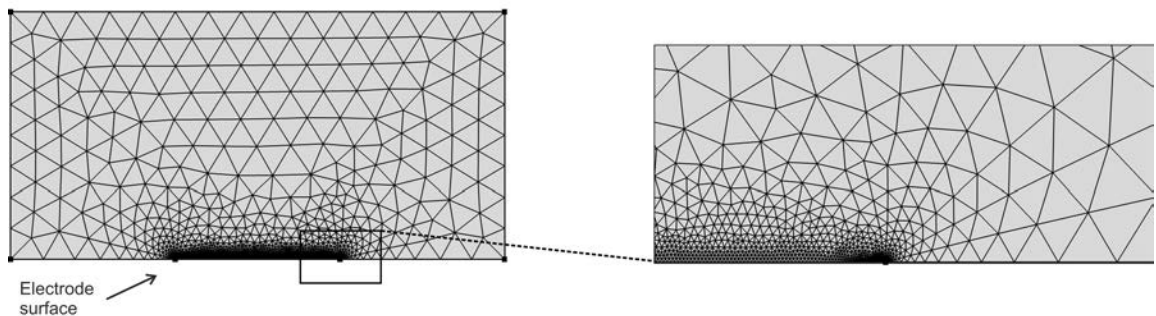


Figure 2.7: Representation of a typical mesh used for a 2D domain. The inset shows the electrode-insulating material boundary where the triangular elements must be markedly smaller than in other regions of the simulated domain.

2.2.2 COMSOL Multiphysics overview

COMSOL Multiphysics is a commercial available software based of finite element methods that is used as a simulation solver.

COMSOL is structured in different modules, depending on the specific application of the simulation. Each module includes the particular ‘physics’, which is how the software defines the partial differential equations required to describe physical phenomena. The user-friendly interface of the software makes unnecessary to introduce manually the mathematical equations, and also allows to solve more than one physics or PDE in the same model.

The software also allows to easily create the mesh that will be used to implement the FEM. For this, a predefined mesh can be automatically drawn by the software depending on the size of the domains and the physics to be studied, or it can be manually defined allowing to refine it into smaller elements in those regions prone to suffer from acute gradients, as explained above.

Last, depending on the modules used in the simulation for the study to be solved, different types of analysis can be included such as ‘Time dependent’ or ‘Stationary’, which evaluate the evolution of the desired variable under transient or stationary conditions respectively. Also, among other interesting features, a ‘Parametric sweep’ of different independent variables is of great use since it allows to solve the simulation under different conditions in the same calculation.

Bibliography

- [1] Rios, A.; Escarpa, A.; Simonet, B. *Miniaturization in analytical chemistry*; John Wiley & Sons, New Jersey, 2009.
- [2] Leech, D.; Kavanagh, P.; Schuhmann, W. Enzymatic fuel cells: recent progress. *Electrochim. Acta* **2012**, *84*, 223–234.
- [3] Luckarift, H. R.; Atanassov, P. B.; Johnson, G. R. *Enzymatic fuel cells. From fundamentals to applications*; John Wiley & Sons, New Jersey, 2014.
- [4] Yetisen, A. K.; Akram, M. S.; Lowe, C. R. Paper-based microfluidic point-of-care diagnostic devices. *Lab. Chip* **2013**, *13*, 2210–2251.
- [5] Liu, C. Recent Developments in Polymer MEMS. *Adv. Mater.* **2007**, *19*, 3783–3790.
- [6] Hallgrímsson, B. *Prototyping and modelmaking for product design*; Promopress, 2012.
- [7] Jo, B.-H.; Lerberghe, L. M. V.; Motsegood, K. M.; Beebe, D. J. Three-dimensional micro-channel fabrication in polydimethylsiloxane (PDMS) elastomer. *J. Microelectromech. Syst.* **2000**, *9*, 76–81.
- [8] Friedrich, C. R.; Vasile, M. J. Development of the micromilling process for high-aspect-ratio microstructures. *J. Microelectromech. Syst.* **1996**, *5*, 33–38.
- [9] Bertsch, A.; Jiguet, S.; Renaud, P. Microfabrication of ceramic components by microstereolithography. *J. Micromech. Microeng.* **2004**, *14*, 197–203.
- [10] Folch, A.; Ayon, A.; Hurtado, O.; Schmidt, M.; Toner, A. Molding of deep polydimethylsiloxane microstructures for microfluidics and biological applications. *J. Biomech. Eng.* **1999**, *121*, 28–34.
- [11] Bartholomeusz, D.; Boutté, R.; Andrade, J. Xurography: rapid prototyping of microstructures using a cutting plotter. *J. Microelectromech. Syst.* **2005**, *14*, 1364–1374.
- [12] Snakenborg, D.; Klank, H.; Kutter, J. P. Microstructure fabrication with a CO₂ laser system. *J. Micromech. Microeng.* **2004**, *14*, 182–189.
- [13] Gonzalez-Macia, L.; Morrin, A.; Smyth, M. R.; Killard, A. J. Advanced printing and deposition methodologies for the fabrication of biosensors and biodevices. *Analyst* **2010**, *135*, 845–867.

- [14] Greer, J.; Sundberg, S. O.; Wittwer, C. T.; Gale, B. K. Comparison of glass etching to xurography prototyping of microfluidic channels for DNA melting analysis. *J. Micromech. Microeng.* **2007**, *17*, 2407–2413.
- [15] Toossi, A.; Daneshmand, M.; Sameoto, D. A low-cost rapid prototyping method for metal electrode fabrication using a CO₂ laser cutter. *J. Micromech. Microeng.* **2013**, *23*, 047001–047010.
- [16] Nakayama, N.; Matsumoto, H.; Nakano, A.; Ikegami, S.; Uda, H.; Yamashita, T. Screen printed thin film CdS/CdTe solar cell. *Jpn. J. Appl. Phys.* **1980**, *19*, 703–712.
- [17] Metters, J. P.; Kadara, R. O.; Banks, C. E. New directions in screen printed electro-analytical sensors: an overview of recent developments. *Analyst* **2011**, *136*, 1067–1076.
- [18] Komuro, N.; Takaki, S.; Suzuki, K.; Citterio, D. Inkjet printed (bio)chemical sensing devices. *Anal. Bioanal.Chem.* **2013**, *405*, 5785–5805.
- [19] Moya, A.; Gabriel, G.; Villa, R.; del Campo, F. J. Inkjet-printed electrochemical sensors. *Curr. Opi. Electrochem.* **2017**, *3*, 29–39.
- [20] Pellitero, M. A.; Kitsara, M.; Eibensteiner, F.; del Campo, F. J. Rapid prototyping of electrochemical lateral flow devices: stencilled electrodes. *Analyst* **2015**, *141*, 2515–2522.
- [21] Banks, C. E.; Foster, C. W.; Kadara, R. O. *Screen-printing electrochemical architectures*; Springer, New York, 2016.
- [22] Kuroda-Electric, <http://www.kuroda-electric.eu/screen-mesh>.
- [23] Asada-Mesh, <https://asada-mesh.co.jp/en/products/>.
- [24] Compton, R. G.; Laborda, E.; Ward, K. R. *Understanding voltammetry: simulation of electrode processes*; Imperial College Press, London, 2014.
- [25] Dickinson, E. J. F.; Ekström, H.; Fontes, E. COMSOL Multiphysics®: Finite element software for electrochemical analysis. A mini-review. *Electrochem. Comm.* **2014**, *40*, 71–74.
- [26] Cutress, I. J.; Dickinson, E. J. F.; Compton, R. G. Analysis of commercial general engineering finite element software in electrochemical simulations. *J. Electroanal. Chem.* **2010**, *638*, 76–83.

- [27] COMSOL, <https://www.comsol.com/multiphysics/finite-element-method>.
- [28] Zimmerman, W. B. J. *Process modelling and simulation with finite element methods*; World Scientific, Singapore, 2004.
- [29] Gavaghan, D. J. An exponentially expanding mesh ideally suited to the fast and efficient simulation of diffusion processes at microdisc electrodes. 2. Application to chronoamperometry. *J. Electroanal. Chem.* **1998**, 456, 13–23.

3

A self-powered electrochromic biosensor

This chapter demonstrates proof-of-concept of the self-powered electrochromic devices presented in this thesis. First, a lateral flow electroanalytical device was fabricated using rapid-prototyping techniques, and was tested using a low working potential glucose biosensor.

The designed electroanalytical cell was then combined with an electrochromic Prussian Blue electrode that serves as a power source for the glucose biosensor. The geometric combination of the two electrodes comprising the device turns the Prussian Blue reaction at the electrode into a display giving a direct readout of the glucose concentration. This is due to the path that the electric current follows inside the cell, which brings about a progressive colour switch that is proportional to the analyte concentration.

The content of this chapter has been previously published in the following articles:

- Pellitero, M.A., Kitsara, M., Eibensteiner, F., del Campo, F.J.; *Rapid prototyping of electrochemical lateral flow devices: stencilled electrodes*, **Analyst**, 2016, 141, 2515–2522.
- Pellitero, M.A., Guimerà, A., Kitsara, M., Villa, R., Rubio, C., Lakard, B., Douche, M-L., Hihn, J-Y., del Campo, F.J.; *Quantitative self-powered electrochromic biosensors*, **Chemical Science**, 2017, 8, 1995–2002.

3.1 Introduction

Self-powered biosensors, first introduced by Katz and Willner in 2001,¹ are analytical tools in which energy output is proportional to the concentration of a target analyte. Some advantages of this kind of systems are that they are highly specific, and that the sensor consists only of two electrodes without external voltage being applied to them. Their main drawback, though, is that due to their typically low energy production, these systems require some form of control instrumentation to quantify the sensor output. This increases their cost and complexity, and explains why, after over a decade, their development level remains so low.

The commonest approach to developing self-powered and self-contained analytical devices consists in the miniaturization through integration of different components into the same package,^{2,3} relying on the use of silicon-based electronics, which are seemingly crucial to all known self-powered devices.⁴

Electrochromic materials^{5,6} can overcome this dependence on silicon-based electronics and their inherent limitations in self-powered chemical sensors. The use of electrochromic materials in the construction of self-powered displays is hardly new,^{7,8} but their application in stand-alone quantitative analytical devices is. Materials such as Prussian Blue^{9,10} have been recently introduced in the construction of self-powered devices with minimal instrumentation needs, so that detection reactions can be monitored directly by the naked eye.¹¹

Of all the existing electrochromic devices, none of them allow the direct quantification of the analyte, as they rely on optical readers to translate the colour change into analyte concentration values.¹²⁻¹⁵ This may be just a minor inconvenience, given the widespread availability of smartphones with massive processing capabilities and increasingly better cameras.¹⁶ However, in line with other recent studies using externally powered electrochromic readouts,¹⁷ the results presented here demonstrate that no reader other than the user's eye may be needed to obtain a quantitative result directly.

The approach presented in this chapter couples an electrochromic display to a biosensor so that they form a galvanic system. The novelty of this system arises from the geometric combination of its components. Instead of the sandwich construction of conventional electrochromic displays^{18,19} where anode and cathode face each other to minimize internal resistance, a coplanar configuration was used instead. The use of a coplanar display allows to control the current path through the device, and use internal resistance to its advantage, as the display first changes its colour in the region closer to the anode through the path of least resistance (Figure 3.1).

The results presented here demonstrate that controlling the current path in electrochromic devices enables the construction of simple and yet powerful electroanalytical devices.

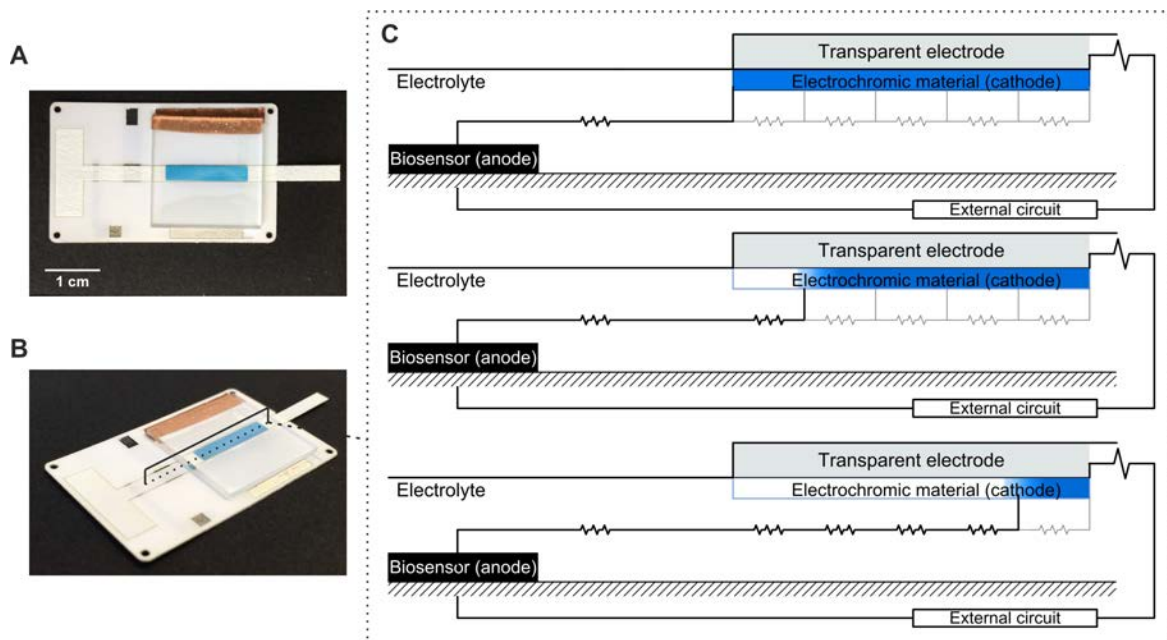


Figure 3.1: Electrochromic biosensor and its operating principle. (A and B) Photographs of the actual electrochromic device. (C) Schematic representation of the device side view, with the biosensor (anode) placed to the left of the electrochromic display (cathode). As the analyte concentration or reaction time increases, the charge consumed at the cathode also increases, resulting in a gradual colour change along the electrode length, following the path of least resistance.

3.2 Experimental

3.2.1 Reagents and materials

The devices presented here were designed using Vectorworks 2015, Student Edition (Teclimits, ES). A CAMM1-GX24 Servo cutter plotter (Roland DG Ibérica, ES) and a 30 W Epilog Mini24 CO₂ laser engraver (Laser Project, ES) were used to cut pieces of ARcare® 8259 and 8939 (Adhesive Research Ltd, IE) pressure sensitive adhesive (PSA) as well as Whatman Fusion 5 and Whatman 1 (GE Healthcare, FR) lateral flow membranes. Ag/AgCl (C61003P7) and carbon (C2030519P4) screen printing pastes (Gwent Electronic Materials Ltd, UK) were used to make the electrodes.

Indium tin oxide (ITO) on 1.1 mm float glass wafers (CEC020S, Präzisions Glas & Optik, GmbH) was etched through a vinyl mask in a hydrochloric acid and nitric acid bath (Sigma-Aldrich, 37 % and 69 % w/w respectively). Isopropanol (Honeywell, 99.5 %), acetone (99.5 %) and ammonia (Panreac, 30 %) were used to clean the ITO electrodes.

A 0.05 M phosphate buffer (Fluka) and 0.1 M potassium chloride (Sigma-Aldrich) solution at pH=7 were used as supporting electrolyte for all the measurements. Glucose oxidase, GOx (Sekisui Diagnostics, EC 1.1.3.4, 236 U mg⁻¹), glutaraldehyde solution, GA (Sigma-Aldrich, 50 % w/w), bovine serum albumin, BSA (Sigma-Aldrich), alco-

holic Nafion® solution (Sigma-Aldrich, 20 % w/w), N,N,N',N'-tetramethyl-p-phenylenediamine, TMPD (Sigma-Aldrich) and ethanol (Panreac, 96 %) were used to fabricate the glucose biosensor.

Electrochemical measurements were carried out using a μ -Autolab III potentiostat (Metrohm) controlled by a PC running GPES 4.1 software.

Carbon electrodes were activated with potential steps from 0 V to -1.5 V in 0.5 M KNO_3 to improve the electrode kinetics.^{20,21}

3.2.2 Electrode fabrication

Two electroanalytical devices were fabricated. The first one consisted of a lateral flow electrochemical cell that was used to carry out the amperometric experiments to characterize the designed glucose biosensor. Figure 3.2 shows the approach followed to fabricate this cell, which comprised the fabrication of stencils *in situ* on PSA films by a simple cutting operation. The overall fabrication process can be divided into three steps: (i) cutting the PSA sheets and lateral flow membranes, (ii) application and curing of conducting pastes, and (iii) device assembly. PSA sheets and lateral flow membranes could both be cut using

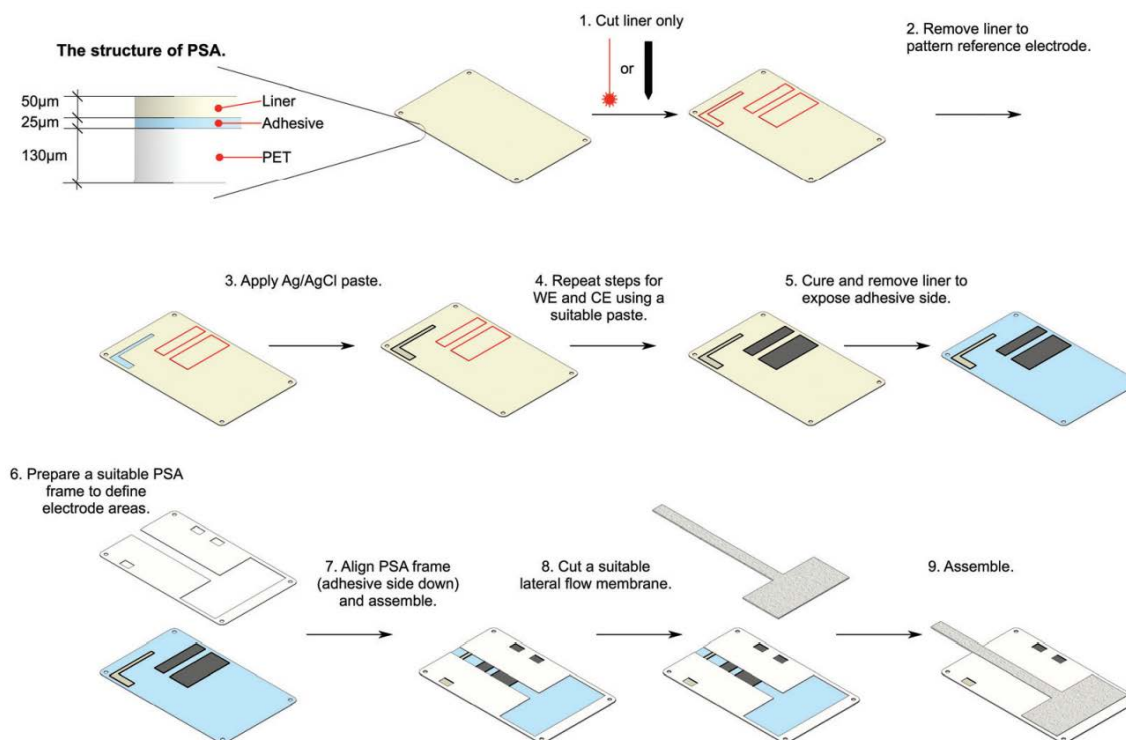


Figure 3.2: Schematic representation showing the fabrication of the electrochemical cells for detection in lateral flow devices using rapid prototyping techniques. The liner of a pressure sensitive adhesive sheet is pre-cut and selectively removed, which transforms it into a stencil. Laser or blade cutting can be used interchangeably.

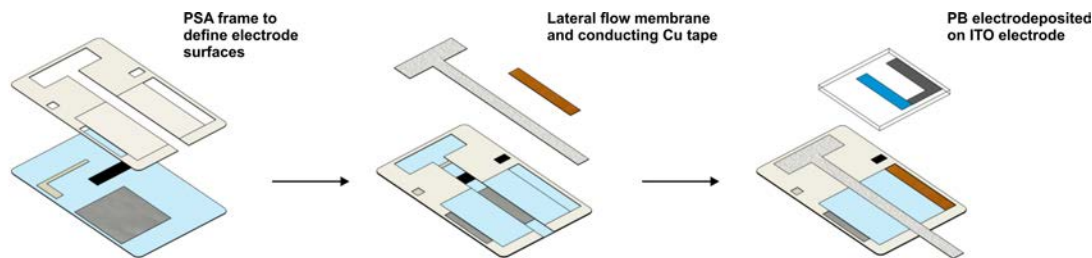


Figure 3.3: Schematic representation of the self-powered device assembly.

the cutter plotter or the laser engraver. The technique is easier to implement with the cutter plotter, however, laser cutting affords much faster processing speeds.

The stencils were made by cutting through the 50 μm -thick siliconized polyester liner protecting the adhesive layer of the PSA. After the removal of the liner, each printing material was applied as depicted in Figure 3.2. To improve electrode performance, and also to prevent the appearance of cracks in the carbon electrodes, up to three paste layers could be applied followed by the corresponding curing steps.

In order to define the active electrode areas and contacts, a second PSA layer was cut. Once the electrodes are adequately sealed, a lateral flow membrane was fitted into the socket left by the PSA cover.

The second electroanalytical cell, which had a similar fabrication process as seen in Figure 3.3, was used to carry out the experiments with the self-powered biosensor. A two-side PSA was used instead, in order to assemble the transparent ITO electrode with the electrodeposited Prussian Blue layer. Also, the electrodes were reconfigured to improve the performance while using the device as a self-powered system.

For the fabrication of the electrochromic display ITO electrodes were first shaped using an etching protocol. For this, an adhesive vinyl cut to a desired shape was fixed on the surface of the ITO substrate, leaving exposed the surface of the conducting material to be removed. The electrodes were immersed in a $\text{HCl} : \text{HNO}_3 : \text{H}_2\text{O}$ solution (4:1:1) for one hour. ITO electrodes were cleaned after the etching using a 10% ammonia solution, isopropanol and acetone, employing ultrasonication for 10 minutes in each cleaning step. The synthesis of the cathode/electrochromic display was done electrochemically.²² For this, 10 mL of 0.02 M aqueous solutions of potassium hexacyanoferrate (III) and iron(III) nitrate nonahydrate were mixed with 4 mL of 1 M hydrochloric acid and 0.1 M potassium chloride to a final volume of 40 mL. A homogeneous Prussian Blue film was achieved by applying a potential of 0.4 V vs Ag/AgCl (KCl 3M) for 20 seconds under constant stirring. The ITO electrode was then rinsed with deionized water and dried in air. Electrochemical activation of the electrochromic coating was required so ions in the supporting electrolyte could enter the crystal structure of the Prussian Blue and thus obtaining electrochemically reversible films (Figure 3.4A). Highly reproducible and re-

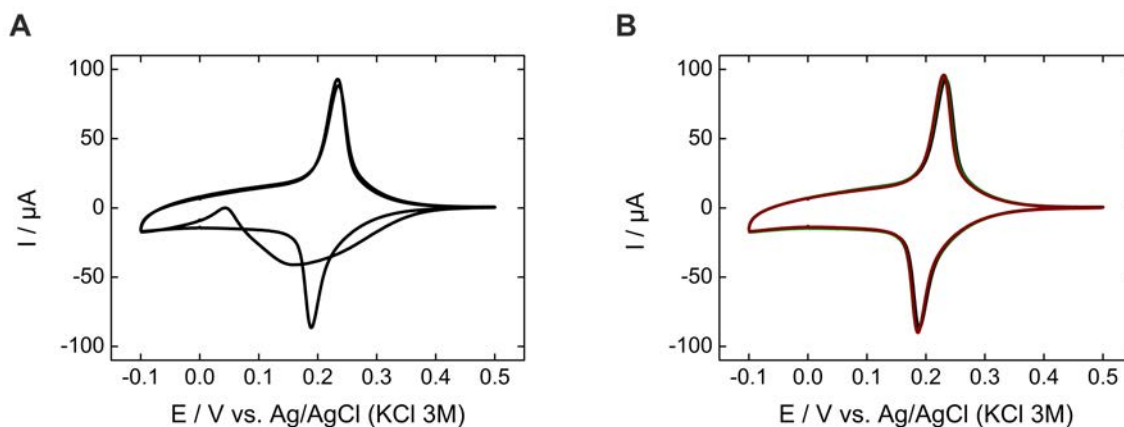


Figure 3.4: (A) Two consecutive voltammograms of an electrodeposited Prussian Blue film on a ITO electrode. (B) Voltammograms of three different PB/ITO electrodes. Scan rates of 5 mV s^{-1} .

versible films were obtained using this method (Figure 3.4B).

3.2.3 Glucose biosensor construction

Glucose biosensors were constructed on $3 \times 3 \text{ mm}$ carbon electrodes as follows: $10 \mu\text{L}$ of a 25 mM TMPD solution prepared in ethanol (96 %) were carefully spread on the surface of the working electrode and allowed to dry at room temperature. Next, $50 \mu\text{L}$ of a solution containing 30 mg mL^{-1} GOx, 0.3 % (w/w) glutaraldehyde, and 1.2 mg mL^{-1} BSA prepared in the supporting electrolyte were mixed with $50 \mu\text{L}$ of an alcoholic 1 % (w/w) Nafion solution and vigorously stirred. $5 \mu\text{L}$ of this solution were cast on the TMPD film and dried overnight at 4°C in darkness. The electrode was thoroughly rinsed with deionized water, and then polarized at 0.2 V vs Ag/AgCl for 10 minutes in the supporting electrolyte until a low, and stable background current was observed.

3.3 Results and discussion

This section demonstrates the feasibility of the designed self-powered electrochromic device. First, the stencil-printed electrochemical cell is characterized, and a glucose biosensor with a low working potential is used to validate its performance. Then, an electrochromic display is mounted on the electrochemical cell to study its behavior as a visual coulometer in a coplanar electrode arrangement. Last, the glucose biosensor is combined with the horizontal electrochromic display to obtain a self-powered system able to provide quantitative glucose concentration information.

3.3.1 Electrochemical characterization

The performance of the stencil-printed electrodes was analyzed. For this, the dependence of both peak current (I_p) and peak-to-peak separation (ΔE_p) with the scan rate (ν) was evaluated in the range from 5 mV s^{-1} to 2 V s^{-1} . Figure 3.5 shows the voltammograms and the representation of I_p vs $\nu^{1/2}$ for a typical stencil printed electrode with 3 layers of deposited carbon material. The data present a linear region consistent with a planar diffusion controlled system up to *ca.* 200 mV s^{-1} . The current deviates significantly at higher scan rates, indicating sluggish electron transfer kinetics. The electron transfer rate constant was calculated from the $\Delta E_p - \log(\nu)$ dependence using the methods of Matsuda-Ayabe²³ and the more recent by Lavagnini *et al.*,²⁴ leading both methods to comparable results, $5.04 \cdot 10^{-3} \text{ cm s}^{-1}$ and $5.2 \cdot 10^{-3} \text{ cm s}^{-1}$ respectively. The results indicate that, despite their quasi-reversible kinetics, the presented stencil-printed electrodes may be suitable for electroanalytical work.

The effect that the amount of printed layers had on the physical and electrochemical properties of the electrodes was also evaluated. As shown in Table 3.1, the oxidation and reduction peak-to-peak separation decreases, and the electron transfer rate constant improves as the number of layers increases from one to three. From the peak-to-peak separations observed, the electron transfer rate constant was estimated to be between $6 \cdot 10^{-4} \text{ cm s}^{-1}$ and $3 \cdot 10^{-3} \text{ cm s}^{-1}$ for electrodes made of one or three carbon paste layers respectively. This improvement in the electrochemical response when more carbon paste is applied is also likely related to a decrease in electrode resistance. As the data show, resistance along a $5 \times 3 \text{ mm}$ track decreases with increasing thickness. Also, a decrease in the water contact angle measurements is observed for increasing amounts of

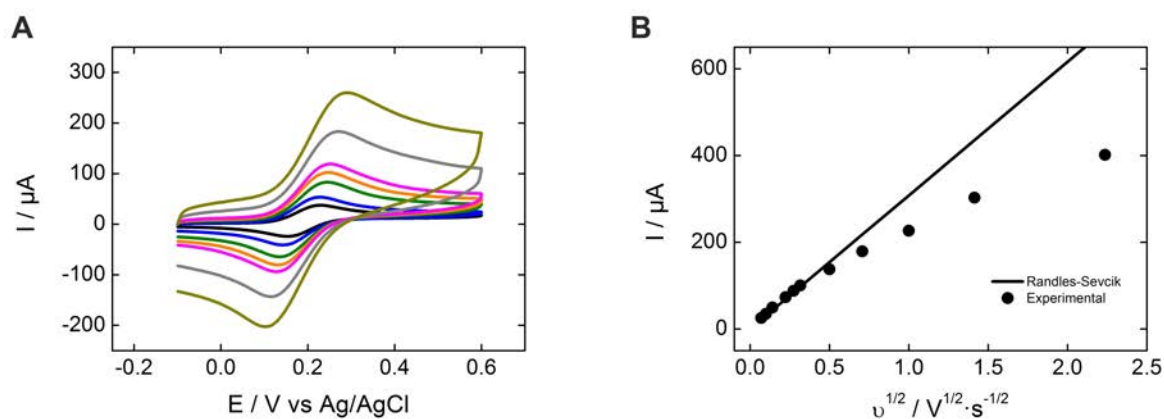


Figure 3.5: (A) Voltammograms recorded in a 5 mM ferrocyanide solution prepared in supporting electrolyte at different scan rates ($10, 20, 50, 75, 100, 250$ and 500 mV s^{-1}). (B) Peak current as a function of the square root of the scan rate for the cyclic voltammograms obtained in A, and the predicted behaviour using the Randles-Ševčík equation for a $3 \times 3 \text{ mm}$ working electrode. A diffusion coefficient value of $6.5 \cdot 10^{-10} \text{ m}^2 \text{ s}^{-1}$ was used to calculate the theoretical response of the electrodes.

| | Thickness (μm) | Contact angle ($^\circ$) | Track resistance (Ω) | ΔE_p (mV) | k_s (cm s^{-1}) ²⁴ |
|-------------------|-----------------------------|----------------------------|-------------------------------|-------------------|--|
| Carbon - 1 layer | 55 ± 2 | 126 ± 2 | 83 ± 10 | 172 ± 9 | $5.6 \cdot 10^{-4}$ |
| Carbon - 2 layers | 68 ± 3 | 129 ± 3 | 60 ± 8 | 120 ± 6 | $1.4 \cdot 10^{-4}$ |
| Carbon - 3 layers | 85 ± 5 | 113 ± 7 | 49 ± 6 | 96 ± 9 | $2.7 \cdot 10^{-3}$ |
| Ag/AgCl - 1 layer | 55 ± 2 | 109 ± 2 | | | |

Table 3.1: Comparison of physical and electrochemical properties of different working electrodes in a typical batch ($n=3$).

deposited material. All of the phenomena mentioned above point at a possible variation in the composition of the electrode material. This is likely due to the action of the solvent of the printing paste which, in contact with the adhesive layer of the PSA, may dissolve the adhesive material, altering the composition of the carbon layer after the curing step. This hypothesis is in agreement with the observed data depicted in Table 3.1 which show that a better performance is obtained at electrodes with a higher graphite content.

To rule out the possibility that the changes in electrode composition were due to the curing conditions as reported in previous works,²⁵ electrodes with one carbon layer were cured for the same amount of time as the electrodes with three layers (3 curing steps of 15 minutes each). As seen in Figure 3.6, cyclic voltammograms show that the electrochemical performance is markedly worse in the case of electrodes with one layer, despite having the same amount of curing time, which reinforces the idea of contamination caused by the adhesive material. However, this contamination is minimized with increasing printed layers and so electrodes were consequently made depositing a total amount of three carbon layers.

Last, Fusion 5 lateral flow membranes were mounted on devices featuring glucose biosensors as show in Figure 3.2. As expected, steady-state currents showing a linear dependence on the concentration ferrocyanide were observed at a fixed potential of 0.4 V (Figure 3.7A). The effect of the flow of electroactive material can be observed in Figure 3.7B, where the shape of the voltammograms is closer in shape to those obtained in a stationary diffusion regime, where forward and backward sweep overlap.²⁶

3.3.2 Amperometric detection of glucose

To demonstrate the suitability of the fabricated electrodes as electrochemical detectors in paper-based electroanalytical applications, the chips presented above were used to study the response of a glucose biosensors under flow conditions.

To calibrate the biosensors, glucose solutions were allowed to flow through the Fusion 5 paper strip under fully wetted flow conditions.^{27,28} This was achieved by placing a

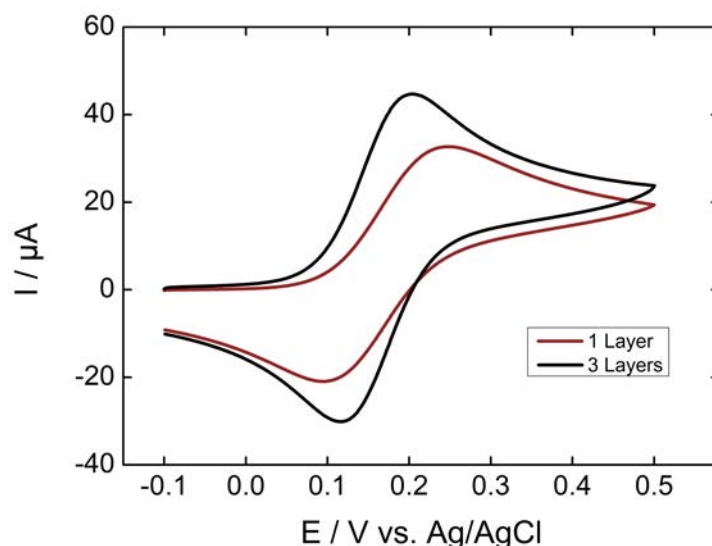


Figure 3.6: Comparison of one and three layers devices cured for the same amount of time (45 min). Voltammograms were obtained for a 5 mM ferrocyanide solution prepared in supporting electrolyte. Scan rate of 20 mV s^{-1} .

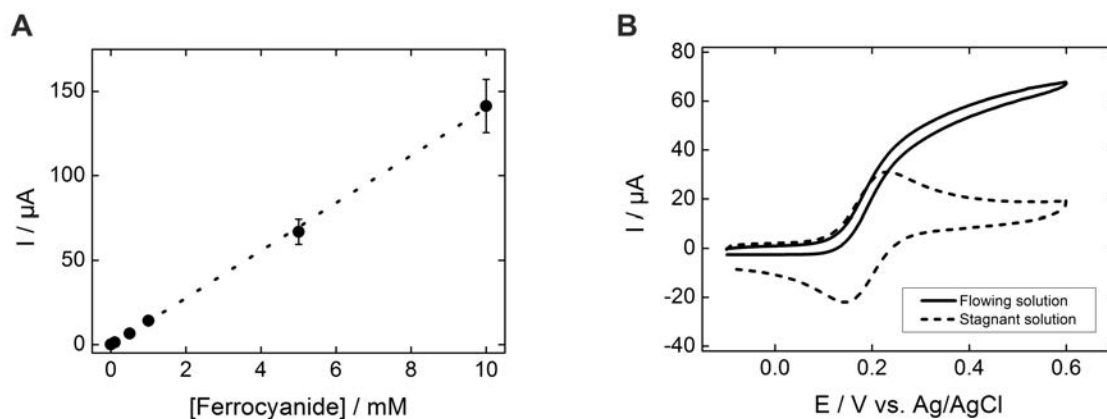


Figure 3.7: (A) Amperometric calibration curve obtained for different ferrocyanide concentrations prepared in supporting electrolyte under a flowing regime with a fixed potential of 0.4 V vs Ag/AgCl . (B) Comparison of voltammograms obtained for a 5 mM ferrocyanide solution prepared in supporting electrolyte in a stagnant and flowing solution. Scan rate of 20 mV s^{-1} .

large wicking pad on the wide end of the strip. The working electrode was kept at 0.2 V vs. the upstream Ag/AgCl pseudo-reference electrode, which ensured oxidation of TMPD as depicted below in Figure 3.10A, and the current was recorded. Buffered glucose aliquots of increasing concentration were added every 120 seconds. A stable response was obtained 30 seconds after each addition, as seen in Figure 3.8A, and the Michaelis-Menten plot for the biosensor can be obtained by representing the measured current against the

concentration of glucose (Figure 3.8B).

Human capillary blood samples were collected from a healthy volunteer's thumb using safety lancets. 50 μL of sample were spiked with 150 μL of a 10 mM glucose standard solution to make a final volume of 200 μL in microeppendorf tubes. Samples were used immediately after collection. After calibrating the biosensors using glucose standards of concentrations ranging between 0.5 and 10 mM, the system was rinsed with buffer solution before approximately 50 μL of the test solution was run through the strip (Figure 3.8A). Another drop of blood was analyzed simultaneously using a commercial glucose meter (CardioCheck, Novalab, ES). A blood glucose concentration of 3.0 ± 0.3 mM (54.7 mg dL^{-1}) was determined using the commercial biosensor. A direct interpolation of the current measured by our biosensor using its calibration curve yielded a blood glucose concentration of 2.7 ± 1.2 mM (49 mg dL^{-1}). This lower value compared to the commercial device is thought to be due to the effect of blood cells present in the sample that may lower the flow in the membrane as well as passivate the electrode surface.

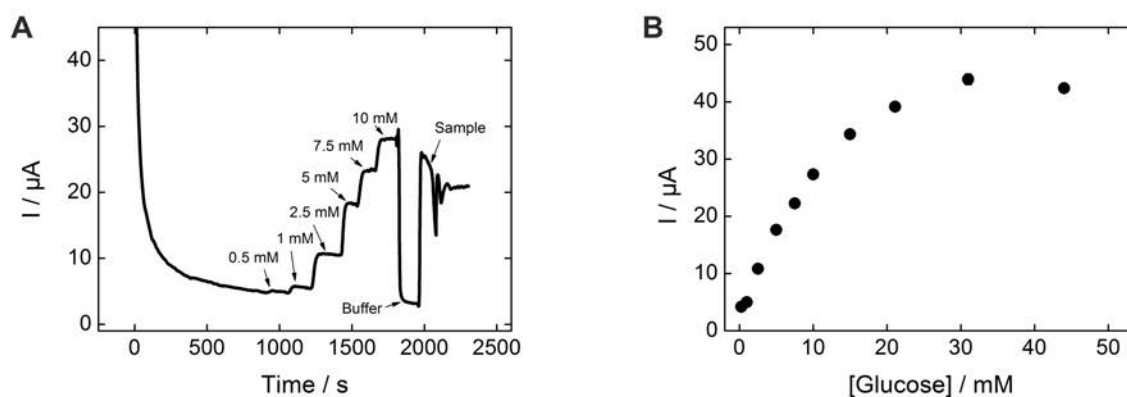


Figure 3.8: (A) Amperometric response of the biosensor to glucose solutions. (B) Michaelis-Menten plot for the biosensor. Measurements were performed at a 0.2 V vs. Ag/AgCl. Error bars represent the standard deviation of $n=4$ electrodes.

3.3.3 Horizontal electrochromic displays

The concept of visual coulometer was demonstrated by using a Prussian Blue horizontal display. The display consists of a 3×15 mm transparent ITO electrode coated by a thin layer of electrodeposited Prussian Blue, 100 ± 15 nm thick. The electrochromic display was assembled on the electrochemical lateral flow device as shown in Figure 3.3. The Prussian Blue electrode is separated by a lateral flow membrane used to contain the electrolyte, which also facilitates the introduction of solutions of different composition. The thickness of the membrane combined with the electrolyte concentration can be used to adjust the electrical resistance between anode and cathode, and therefore, the device per-

formance. For this reason, the membrane used in these experiments was changed from Fusion 5 to a thinner one, Whatman 1, which increased the electrical resistance but allowed to see a better defined colour switch.

A series of experiments were carried out in which a known charge was passed through the system under different conditions. First, the charge contained in the Prussian Blue cathode was determined by integration of the current peaks in a stable cyclic voltammogram, obtaining a charge of 1.2 ± 0.2 mC. This charge was forced through the system at a constant current of $40 \mu\text{A}$, in line with the maximum current output of the glucose biosensor (Figure 3.8B), and the display behaviour was recorded. Figure 3.9A shows images of the Prussian Blue electrode taken at different times. As charge is passed, the colour front moves away from the anode. The figure shows a comparison in the position chosen at the end of the colour bar subjectively by a person (circles), or by numerical analysis of the colour profiles obtained using ImageJ²⁹ (triangles). Figure 3.9B shows the colour intensity profiles determined by ImageJ at different times during the experiment. Clear colours are represented by high % values on the y-axis, whilst darker colours (blue) take lower % values. The position of the colour front was determined using the profiles by extracting the intersection of the two straight lines fitting the region where the discolouration begins and the baseline region where no discolouration is observed (see Annex 1). As expected, the length covered by the colour change is directly proportional to the charge drawn from the electrochromic layer. Figure 3.9C, on the other hand, shows images taken after 30 seconds passing different current levels through the system, which again represents different total charges. This experiment aimed to study the behaviour of the horizontal display as a visual coulometer in the form of a metering bar in the presence of different glucose concentrations. As seen in Figure 3.9D, the system continues to respond well, and the distance traveled by the colour front remains proportional to the total charge. This experiment is only an approximation, because during the experiment with the biosensor both cell potential and current change over time. Nevertheless, this experiment demonstrates proof of principle, and strongly suggests that a clear visual readout is possible if a biosensor with the right oxidation potential is combined with a suitable electrochromic counter electrode.

3.3.4 Self-powered electrochromic biosensor

Last, the Prussian Blue electrode was connected to a glucose biosensor using TMPD as redox mediator. The electrode reactions taking place, which allow the system to work as a galvanic cell, are:

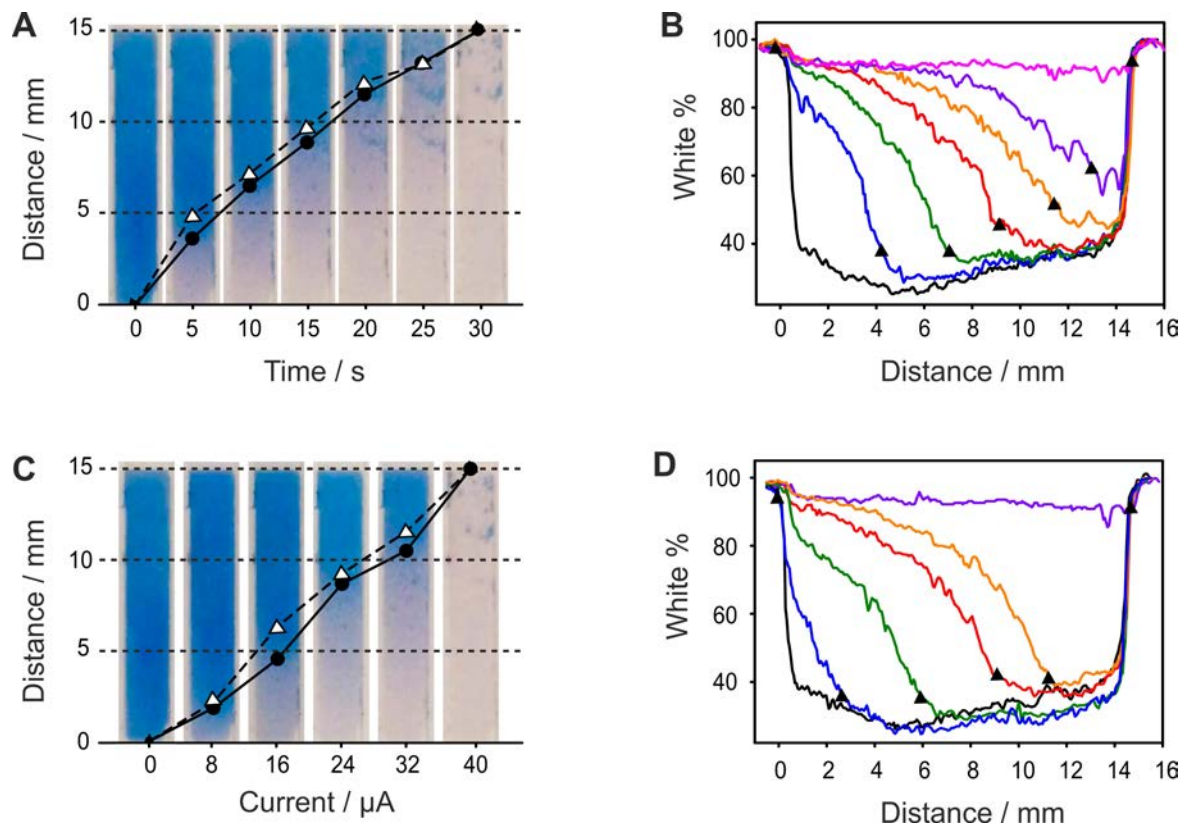
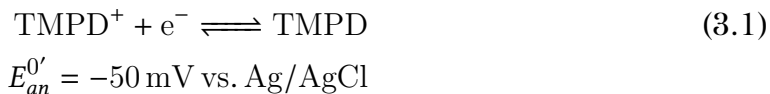
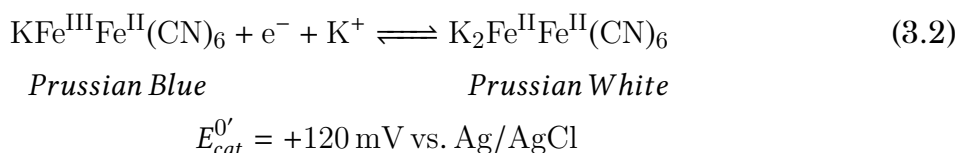


Figure 3.9: Behaviour of the horizontal electrochromic display. (A) Captures of the display at different times under a constant applied current of 40 μA . The points signal the position of the colour front chosen arbitrarily by a user (circles) and determined by analysis of the corresponding colour profiles (triangles). (B) Colour profiles of the electrochromic display obtained with ImageJ software. (C) Captures of the display recorded 30 s after application of different current levels. (D) Colour profiles obtained for the images in C.

At the biosensor:



and at the electrochromic display:



For each electron taken from the TMPD at the anode (biosensor), an electron is transferred to the Fe(III) sites in the Prussian Blue cathode (display) while ions carry the charge inside the cell. Amongst these ions, potassium facilitates a rapid cathode response and ensures the reversibility of the electrochromic process.³⁰ Figure 3.10A shows typical cyclic

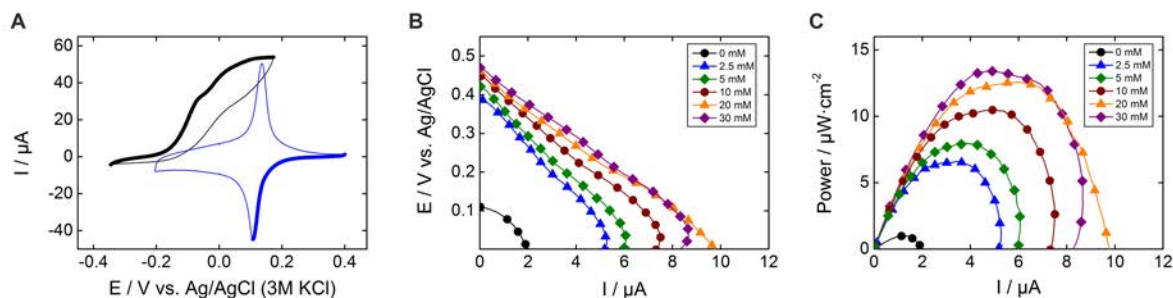


Figure 3.10: (A) Cyclic voltammograms showing the reduction and oxidation of Prussian Blue on an ITO electrode (blue) and the response of a biosensor in contact with a saturating concentration of glucose (black). (B) Polarization curves taken from the OCV to 0 V at a scan rate of 1 mV s^{-1} . (C) Power curves obtained from the polarization curves.

voltammograms of both the glucose oxidase/TMPD anode and the Prussian Blue cathode. The onset of the reduction of Prussian Blue is observed at 0.3 V while the oxidation of TMPD by action of the enzymatic activity begins approximately at -0.15 V, leading to cell potentials around 0.45 V, in line with the OCV observed in the polarization curves recorded at various glucose concentrations (Figure 3.10B).

The behaviour of the self-powered device was studied connecting the electrochromic cathode to the biosensing anode, thus initiating the enzymatic reaction. Figures 3.10B and C show the corresponding polarization and power curves where the limited amount of charge available at the Prussian Blue electrode is apparent at high glucose concentrations. As the Prussian Blue is depleted, the current passing through the system drops. It can also be observed a progressive increase in the maximum current and power density produced by the cell as the fuel concentration is increased. As other self-powered devices, the system power output is proportional to the analyte concentration. In this case a maximum power density around 13 W cm^{-2} was obtained.

To carry out the experiments using the Prussian Blue cathode as a visual readout, anode and cathode were connected, and glucose solutions were allowed to flow through the system as shown in Figure 3.11. The colour switch was recorded and captures were taken 30 seconds after the connection of the electrodes (Figure 3.12A). The use of image analysis software helps to have a more accurate readout of the display, observing a bigger difference between the two measuring methods than in the case of controlled charge experiments where a better defined colour switch was achieved. Another interesting feature of these experiments is that the biosensor was only able to convert the colour of the display on roughly half of its area, even though the biosensor was able to draw currents of similar magnitude as those in the controlled current experiments as seen in Figure 3.8B. These two effects observed when operating the device from a biosensor are caused by the device internal resistance, which changes during the experiment. Due to the changing internal resistance, the cathode is not able to power the reaction at the anode the

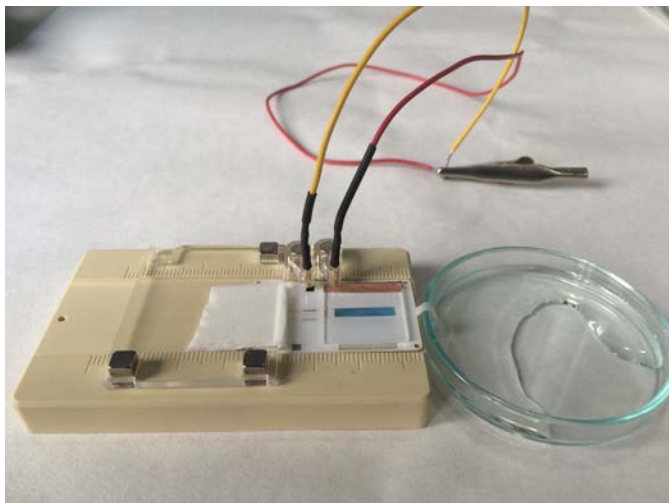


Figure 3.11: Photograph of the self-powered device during a measurement of a glucose solution.

way a potentiostat at a fixed potential does, which causes a decrease in the current output of the biosensor, going from a maximum current of $40\ \mu\text{A}$ to roughly $10\ \mu\text{A}$. The internal resistance progressively increases also as a result of the Prussian Blue depletion, and the biosensing anode current output decreases. Both effects translate into a blurrier colour switch as well as shorter conversion distances (6–7 mm) instead of consuming all the Prussian Blue available at the cathode.

The variability shown by the self-powered biosensor (Figure 3.12A) is thought to be due to differences in construction of the device. Since the display is pressure-mounted on the lateral flow membrane holding the electrolyte, changes in geometry arising from different assemblies affect sample flow conditions and especially the internal electrical re-

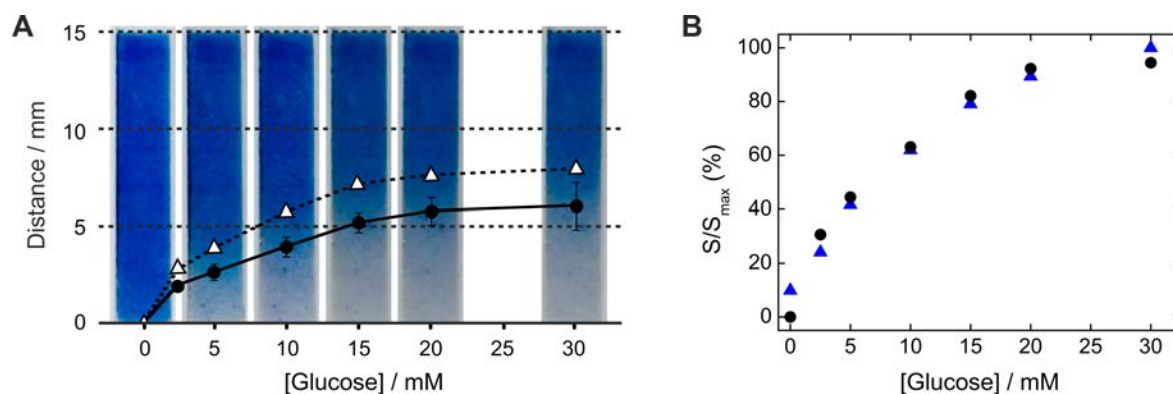


Figure 3.12: (A) Captures of the display 30 seconds after the addition of different glucose solutions. The points signal the position of the colour front determined subjectively (circles) and from the analysis of colour profiles (triangles). Error bars correspond to the standard deviation of the measurements obtained from four different devices. (B) Plots of the normalized to the maximum biosensor current (blue triangles) and colour front position (black circles) as a function of glucose concentration.

sistance. Figure 3.12B shows that the self-powered device follows the Michaelis-Menten curve of the biosensor. The current data from Figure 3.8B and the distances measured in Figure 3.12A have been normalized and plotted together. As the figure shows, the two normalized datasets are in excellent agreement. Last, the device was tested with a diluted sample of a commercial fruit juice. The amount of glucose present in the sample was previously determined with the commercial glucose meter, leading to a value of 7.6 ± 0.2 mM. The interpolation of the length of the colour change in the strip when the sample was let to flow yielded a glucose concentration of 7.3 ± 0.4 mM, demonstrating the value of this instrumentation-less device to quantify the concentration of an analyte in a sample.

3.4 Conclusions

The work presented in this chapter describes the prototyping of a lateral flow electroanalytical device using cutting techniques in combination with printing techniques. A glucose biosensor with a low working potential was developed to demonstrate the feasibility of the manufactured devices as analytical tools. The approach presented here can reduce considerably the development time and cost of new electroanalytical devices. These devices served as tools to show proof of concept of an unconventional use of electrochromic materials in the sensing field. The traditional parallel-plate configuration of electrochromic displays was modified to a coplanar one, which allows to take advantage of the ohmic drop inside the device and use the colour switch of the display as a visual coulometer. Moreover, the electrochromic display was coupled to the glucose biosensor so that a galvanic cell is formed. This way, the electrochromic material not only acts as a visual readout but it also acts as cathode, triggering the enzymatic reaction at the anode. The geometric configuration of the system allows to have a self-powered device which provides quantitative information about the concentration of the analyte. The principles described in this chapter are not only applicable to glucose biosensors, but they can also be extended to other sensors with the only pre-requisite for the system to present a positive cell voltage.

Bibliography

- [1] Katz, E.; Bückmann, A. F.; Willner, I. Self-powered enzyme-based biosensors. *J. Am. Chem. Soc.* **2001**, *123*, 10752–10753.
- [2] Turner, A. Biosensors: sense and sensibility. *Chem. Soc. Rev.* **2013**, *42*, 3184–3196.
- [3] Gao, W.; Emaminejad, S.; Nyein, H. Y. Y.; Challa, S.; Chen, K.; Peck, A.; Fahad, H. M.; Ota, H.; Shiraki, H.; Kiriya, D.; Lien, D.-H.; Brooks, G. A.; Davis, R. W.; Javey, A. Fully integrated wearable sensor arrays for multiplexed in situ perspiration analysis. *Nature* **2016**, *529*, 509–514.
- [4] Arechederra, R. L.; Minter, S. D. Self-powered sensors. *Anal. Bioanal. Chem.* **2011**, *400*, 1605–1611.
- [5] Monk, P.; Mortimer, R.; Rosseinsky, D. *Electrochromism and electrochromic materials*; Cambridge University Press, Cambridge, 2007.
- [6] Beaujuge, P. M.; Reynolds, J. R. Color control in π -conjugated organic polymers for use in electrochromic devices. *Chem. Rev.* **2010**, *110*, 268–320.
- [7] Möller, M.; Leyland, N.; Copeland, G.; Cassidy, M. Self-powered electrochromic display as an example for integrated modules in printed electronics applications. *Eur. Phys. J.: Appl. Phys.* **2010**, *51*, 33205.
- [8] Wang, J.; Zhang, L.; Yu, L.; Jiao, Z.; Xie, H.; Lou, X. W.; Sun, X. W. A bi-functional device for self-powered electrochromic window and self-rechargeable transparent battery applications. *Nat. Comm.* **2014**, *5*, 1–7.
- [9] Neff, V. D. Electrochemical oxidation and reduction of thin films of Prussian Blue. *J. Electrochem. Soc.* **1978**, *125*, 886–887.
- [10] Kong, B.; Selomulya, C.; Zheng, G.; Zhao, D. New faces of porous Prussian blue: interfacial assembly of integrated hetero-structures for sensing applications. *Chem. Soc. Rev.* **2015**, *44*, 7997–8018.
- [11] Zhang, X.; Zhang, L.; Zhai, Q.; Gu, W.; Li, J.; Wang, E. Self-powered bipolar electrochromic electrode arrays for direct displaying applications. *Anal. Chem.* **2016**, *88*, 2543–2547.
- [12] Liu, H.; Crooks, R. M. Paper-based electrochemical sensing platform with integral battery and electrochromic read-out. *Anal. Chem.* **2012**, *84*, 2528–2532.

- [13] Zloczewska, A.; Celebanska, A.; Szot, K.; Tomaszewska, D.; Opallo, M.; Jönsson-Niedziolka, M. Self-powered biosensor for ascorbic acid with a Prussian blue electrochromic display. *Biosens. Bioelectron.* **2014**, *54*, 455–461.
- [14] Pinyou, P.; Conzuelo, F.; Sliozberg, K.; Vivekananthan, J.; Contin, A.; Pöller, S.; Plumeré, N.; Schuhmann, W. Coupling of an enzymatic biofuel cell to an electrochemical cell for self-powered glucose sensing with optical readout. *Bioelectrochem.* **2015**, *106*, 22–27.
- [15] Xu, W.; Fu, K.; Ma, C.; Bohn, P. W. Closed bipolar electrode-enabled dual-cell electrochromic detectors for chemical sensing. *Analyst* **2016**, *141*, 6018–6024.
- [16] Shen, L.; Hagen, J. A.; Papautsky, I. Point-of-care colorimetric detection with a smartphone. *Lab. Chip* **2012**, *12*, 4240–4243.
- [17] Liana, D. D.; Raguse, B.; Gooding, J. J.; Chow, E. Toward paper-based sensors: turning electrical signals into an optical readout system. *ACS Appl. Mater. Interfaces* **2015**, *7*, 19201–19209.
- [18] Kawahara, J.; Ersman, P. A.; Engquist, I.; Berggren, M. Improving the color switch contrast in PEDOT:PSS-based electrochromic displays. *Org. Electron.* **2012**, *13*, 469–474.
- [19] Shen, D. E.; Österholm, A. M.; Reynolds, J. Out of sight but not out of mind: the role of counter electrodes in polymer-based solid-state electrochromic devices. *J. Mater. Chem. C* **2015**, *3*, 9715–9725.
- [20] Deakin, M. R.; Stutts, K. J.; Wightman, R. M. The effect of pH on some outer-sphere electrode reactions at carbon electrodes. *J. Electroanal. Chem.* **1985**, *182*, 113–122.
- [21] Cui, G.; Yoo, J. H.; Lee, J. S.; Yoo, J.; Uhm, J. H.; Cha, G. S.; Nam, H. Effect of pre-treatment on the surface and electrochemical properties of screen-printed carbon paste electrodes. *Analyst* **2001**, *126*, 1399–1403.
- [22] Karyakin, A. A.; Gitelmacher, O. V.; Karyakina, E. E. Prussian Blue-based first-generation biosensor. a sensitive amperometric electrode for glucose. *Anal. Chem.* **1995**, *67*, 2419–2423.
- [23] Matsuda, H.; Ayabe, Y. Zur theorie der Randles-Sevčičsken kathodenstrahlpolarographie. *Z. Electrochem* **1955**, *59*, 494–503.

- [24] Lavagnini, I.; Antiochia, R.; Magno, F. An extended method for the practical evaluation of the standard rate constant from cyclic voltammetric data. *Electroanalysis* **2004**, *16*, 505–506.
- [25] Grennan, K.; Killard, A.; Smyth, M. Chemically polymerized polyaniline films for the mass-production of biosensor devices. *Electroanalysis* **2005**, *17*, 1360–1369.
- [26] Compton, R. G.; Banks, C. E. *Understanding voltammetry*; Imperial College Press, London, 2011.
- [27] Osborn, J. L.; Lutz, B.; Fu, E.; Kauffman, P.; Stevens, D. Y.; Yager, P. Microfluidics without pumps: reinventing the T-sensor and H-filter in paper networks. *Lab Chip* **2010**, *10*, 2659–2665.
- [28] Fu, E.; Ramsey, S. A.; Kauffman, P.; Lutz, B.; Yager, P. Transport in two-dimensional paper networks. *Microfluid. Nanofluid.* **2011**, *10*, 29–35.
- [29] ImageJ, <https://imagej.nih.gov/ij/>.
- [30] Karyakin, A. A. Prussian blue and its analogues: electrochemistry and analytical applications. *Electroanalysis* **2001**, *13*, 813–819.

4

iR Drop effects in self-powered electrochromic biosensors

The proof of concept device presented in the previous chapter exploited the ohmic drop inside an enzymatic fuel cell. This enabled the development of a self-powered electrochromic device that displayed quantitative information about the analyte concentration without the need for external equipment. In this chapter, numerical simulations are used to better understand the different phenomena affecting the behavior of such electrochromic devices, and which will then be used as a designing tool to improve its performance and explore its limitations.

The contents of this chapter have been published in part in:

- Pellitero, M.A., Guimerà, A., Villa, R., del Campo, F.J.; *iR Drop Effects in Self-Powered and Electrochromic Biosensors*, *Journal of Physical Chemistry C*, 2018, 122, 2596–2607.

4.1 Introduction

Ohmic, or iR drop, is an undesirable effect in electrochemical experiments stemming from a combination of electrolyte resistance and electrochemical cell geometry that results in uneven distribution of the electric current or potential.¹ The most common approaches to control ohmic drop involve increasing the conductivity of the solution that is in contact between electrodes,^{2,3} avoiding the passage of large currents through the cell,^{4,5} or a combination of both.^{6,7}

In contrast, the self-powered device presented in Chapter 3 takes advantage of the internal resistance. By controlling the iR drop inside the device, it was demonstrated that it is possible to translate the length of the colour switch of an electrochromic display into a quantitative measurement of the analyte concentration. This is achieved by the shifted electrode construction, ‘coplanar configuration’, which differs from the conventional ‘sandwich configuration’ where anode and cathode face each other, separated by a gap of a few microns that contains the electrolyte, and thus minimizing ohmic losses, which ensures a rapid and homogeneous colour switch.^{8,9}

In this chapter, numerical simulations are used to understand the factors controlling the operation of this type of devices to explore their limitations and to use them as a design tool to successfully predict the behavior of related systems prior to their fabrication. The mathematical model and the results presented here may be of help to those working on the development of electrochemical applications, particularly those including fuel cells, (bio)sensors and electrochromic devices.

4.2 Theory

Figure 4.1A presents a schematic representation of the electrochromic device used in Chapter 3, which has a rectangular geometry resembling a channel cell with two coplanar electrodes.¹⁰ In line with other self-powered sensors, and electrochemical power sources in general, only two electrodes were needed: anode and cathode.¹¹ As explained before, the use of coplanar electrodes in the design of the electrochemical cell provides the necessary control over the current path along the device, which allows to take advantage of the internal resistance to generate a colorimetric signal that can be easily read by the naked eye without the aid of external equipment (Figure 4.1B).

The system presented is based on a second-generation glucose biosensor,¹² which relies on the use of a redox mediator to shuttle electrons between the electrode and the active site of the enzyme, as depicted in Figure 4.1C. The mediator diffuses inside the biosensing layer in order to carry the charge to and fro. The electric current generated by the biosensor is transported through the electrolyte to the electrochromic display which is then reduced, switching from blue to colourless (Figure 4.1D).

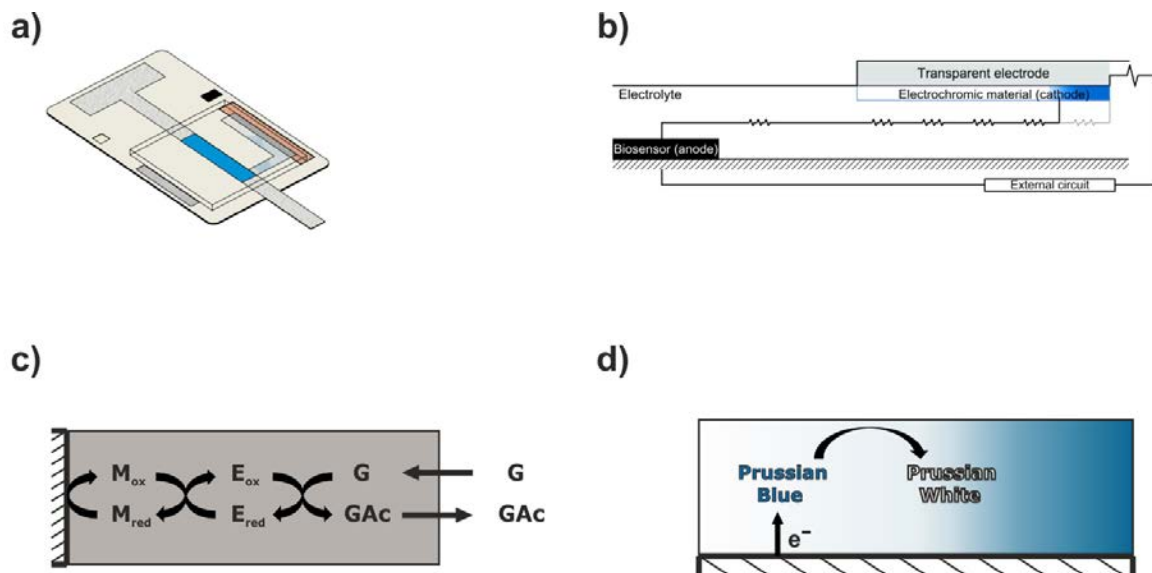
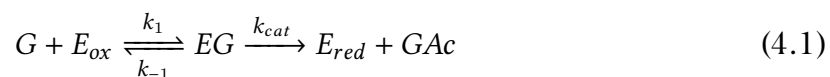


Figure 4.1: (A) Schematic representation of the self-powered electrochromic device. (B) Side view of the device. The charge consumed at the cathode increases with time or with higher analyte concentrations, creating a discolouration along the display that follows the path of least resistance. (C) Reaction sequences taking place in a general second-generation glucose biosensor. (D) Reaction of the electrochromic display at the transparent ITO electrode.

The mathematical model presented here considers: (i) the chemical reaction of the analyte and the redox mediator with the enzyme at the anode, (ii) diffusion of the redox mediator to the electrode surface, (iii) electron transfer between the redox mediator and the anode, and between the electrochromic species and the cathode, and (iv) ion conductivity through the electrolyte between electrodes.

4.2.1 Enzyme kinetics

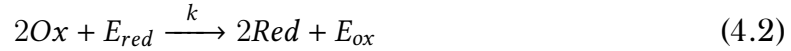
The enzymatic reactions have been modelled as described in Section 1.2.2, according to the Michaelis-Menten mechanism:¹³



This equation represents the homogeneous reaction taking place inside the domain corresponding to the biosensing layer coating the anode. G represents the analyte, e.g., glucose, E_{ox} and E_{red} the oxidized and reduced forms, respectively, of the enzyme glucose oxidase, EG the intermediate enzyme-substrate complex, and GAc the product of the enzymatic reaction, e.g., gluconic acid.

When modelling the enzymatic reaction in equation 4.1, the regeneration of the oxidized form of the enzyme must be taken into account, so the catalytic cycle can go on. In the case of a second-generation biosensor, this regeneration takes place by the action of

the redox mediator in a homogeneous process:



where *Ox* represents the oxidized form of a reversible redox mediator and *Red* its reduced form. Electrons are subtracted from the enzyme, regenerating its active site, and the mediator diffuses to the electrode where is reoxidized by action of the applied electric potential. The overall rate of the enzymatic reaction considering processes 4.1 and 4.2 is given by:¹⁴

$$v = \frac{k_{cat}[E]_{tot}}{1 + \frac{K_M}{[G]} + \frac{K_0}{[Ox]}} \quad (4.3)$$

where the Michaelis-Menten constant is defined as $K_M = (k_{cat} + k_{-1})$, $K_0 = k_{cat}/k$ and $E_{tot} = E_{ox} + E_{red} + EG$. The value of the Michaelis-Menten constant was experimentally determined, and the values of k_{cat} and k were taken from de literature (Table 4.1).¹⁵⁻¹⁷

4.2.2 Mass transport

The presented model does not involve convection or migration of the electroactive species, redox mediator and Prussian Blue, which are only subjective to diffusion according to Fick's laws.¹⁸

$$\frac{\partial C_i}{\partial t} = D_i \nabla^2 C_i \quad (4.4)$$

where i represents a generic species and C_i and D_i are its concentration and diffusion coefficient, respectively.

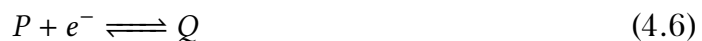
4.2.3 Electrode processes

At the anode, where the glucose biosensor is confined in a small domain, the mediator species *Red* is oxidized back to *Ox* by the action of the electrode potential:



This process may be controlled by either the enzymatic reaction or by the electrode kinetics, depending on the experimental conditions. The prevalence of one process over the other is what determines the actual anode potential.

At the cathode, it is assumed that the electrochromic material is homogeneously distributed over the electrode surface, and it is modelled by a one-electron redox process:



where P and Q are surface-bound species.

| Parameters | Value |
|---|--|
| Channel height, H_{ch} | 127 μm |
| Biosensor thickness, H_{bio} | 5 μm |
| Anode length, L_{ano} | 3 μm |
| Cathode length, L_{cat} | 15 μm |
| Electrode width, W_{elec} | 3 μm |
| Gap between electrodes, L_{gap} | 4 mm |
| Exchange current density in anode, $j_{0,ano}$ | $1 \times 10^2 \text{ A m}^{-2}$ |
| Exchange current density in cathode, $j_{0,cat}$ | $2 \times 10^4 \text{ A m}^{-2}$ |
| PB/PW formal potential, $E_{PB/PW}^0$ | 0.15 V |
| Redox mediator formal potential, $E_{Med^+/Med}^0$ | -0.05 V |
| Initial concentration of the oxidized form of the mediator, $[Ox]_0$ | $5 \times 10^{-2} \text{ mol L}^{-1}$ |
| Initial concentration of the reduced form of the mediator, $[Red]_0$ | $1 \times 10^{-6} \text{ mol L}^{-1}$ |
| Diffusion coefficient of glucose and redox mediator inside the polymeric membrane, $D = D_{gluc} = D_{med}$ | $1 \times 10^{-6} \text{ cm}^2 \text{ m}^{-1}$ |
| PB superficial concentration, $[PB]_{sup}$ | $2.3 \times 10^{-4} \text{ mol m}^{-2}$ |
| Maximum rate of enzymatic reaction, V_{max} | $5 \times 10^{-2} \text{ mol L}^{-1}$ |
| Michaelis-Menten constant for the substrate, K_M | $9 \times 10^{-3} \text{ mol L}^{-1}$ |
| Michaelis-Menten constant for the mediator, K_0 | $8 \times 10^{-5} \text{ mol L}^{-1}$ |
| Turnover number, k_{cat} | 800 s^{-1} |

Table 4.1: Parameters used in the simulations and their values.

Both electrode reactions are assumed to follow a Nernstian behaviour (eq. 1.2). In the case of the surface-bound species of the electrochromic material, the bulk concentration in Nernst equation was substituted by the surface concentration of the species.

The electron transfer is modelled assuming Butler-Volmer kinetics (eq. 1.13), also at both electrodes. In the cases where one of the electrodes remained unmodified, and thus the details of the electrode process were unimportant, a linearized version of the Butler-Volmer equation was used:

$$i = i_0 A \frac{F}{RT} (E - E_{eq}) \quad (4.7)$$

The two cases where this version was used were when a fixed current/potential was applied

from the unmodified anode to study the switching of the electrochromic cathode, or in the chronoamperometric simulations of the glucose biosensor.

The overall passing current can be obtained by integrating the current density along the electrode boundaries. In the case of the 2D domain this is done according to:

$$I_{elec} = W_{elec} \int_{x=0}^{x=x_f} j dx \quad (4.8)$$

where j is the current density vector normal to the electrode surface boundary. A 3 mm electrode width, W_{elec} , akin to the experimental device, was defined to integrate the current densities of the system.

4.2.4 Electrolyte conductivity and ionic current

Current is carried by ions in the electrolyte, and is described by the sum of fluxes of all charged species present:

$$j = \sum_i z_i F j_i \quad (4.9)$$

where z_i and j_i refer to the charge and the flux of the species i . Substituting this expression into the Nernst-Planck equation (eq. 1.20) it is found that:

$$j = -F \left(\nabla \sum_i z_i D_i c_i \right) - \frac{F^2 \nabla \phi}{RT} \sum_i z_i^2 D_i c_i - uF \sum_i z_i c_i \quad (4.10)$$

The last term in equation 4.10 can be neglected upon application of the electroneutrality condition:

$$\sum_i z_i c_i = 0 \quad (4.11)$$

which states that there is no charge separation within the solution, and which only breaks down in the very close vicinity of the electrodes, where the electric field gradient is greatest.¹⁹ However, this was neglected as this occurs at the nanoscale or on a time scale of nanoseconds, and none of these cases apply here.

The composition of the electrolyte was assumed to be homogeneous in all of the domain, with no composition gradients, which also cancels the first term in equation 4.10, thus obtaining Ohm's law for electrolytes:

$$j = -\sigma \nabla \phi \quad (4.12)$$

where the conductivity of the electrolyte is defined by:²⁰

$$\sigma = \frac{F^2}{RT} \sum_i z_i^2 D_i c_i \quad (4.13)$$

Solving these equations enables the determination of the electric field in the solution and, consequently, the value of the electrochemical potential at any point of the simulated domains, which can be related with the change in the concentrations of the present chemical species.

4.3 Computational procedure and model geometry

The approach followed in this chapter consists in first separately validating the models for the anode and the cathode, which in the actual device correspond to a glucose biosensor and a Prussian Blue display, respectively, as seen in Chapter 3. Once these models are validated using experimental data, they are combined to facilitate the study of the complete device. The model geometry presents the anode and cathode shifted on opposite sides of a channel, in line with the working prototype, but the results are equally valid for the case of perfectly coplanar electrodes as in the final prototype presented in this thesis.

Simulations were run using the commercial simulation software COMSOL Multiphysics 5.3 (COMSOL, SE) on a PC (Intel Core i7-4790, 16 Gb RAM) running Windows 7.

The mathematical model presents a dimensionality that has been simplified from three to two dimensions, considering the symmetry along the device midsection. Figure 4.2 shows a schematic representation of the 2D model, including the various subdomains and boundaries involved.

The channel height, H_{ch} , was set at $127\ \mu\text{m}$ to match the dimensions of the actual device, and different heights were also simulated ranging from 50 to $300\ \mu\text{m}$. The glucose biosensor was modelled by a $5\ \mu\text{m}$ domain resting on top of the anode domain. This $5\ \mu\text{m}$ represents the polymeric membrane layer containing the enzyme and the mediator, and its thickness is in line with those of similar reported polymeric membranes.²¹

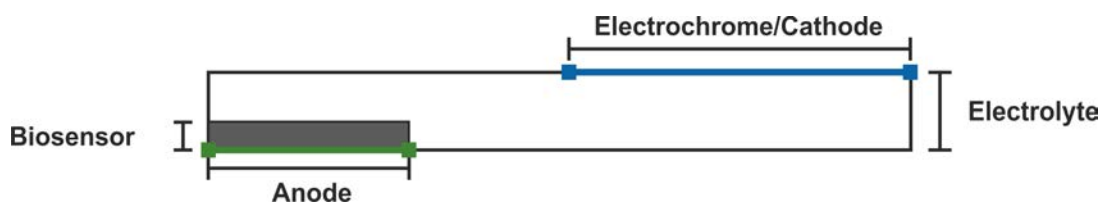


Figure 4.2: Two-dimensional representation of the domains implemented in the model (not to scale). The anode and cathode boundaries are highlighted in green and blue, respectively.

4.4 Results and discussion

4.4.1 Glucose biosensor / Anode

The anode studied in the simulation is a glucose biosensor that relies on glucose oxidase to catalyze the oxidation of glucose to gluconic acid, and on a low potential redox mediator to shuttle electrons between the enzyme and the electrode (see Section 3.2.3). The initial concentrations of the redox mediator and enzyme used in the model were extracted from the experiments. The steady supply of glucose to the biosensor by means of a lateral flow membrane was simulated by setting a constant concentration boundary condition at the interface between the biosensing layer and the electrolyte. Regarding mass transport properties, it was found that the values of the diffusion coefficients of glucose and the redox mediator inside the biosensing layer did not have a significant effect on the biosensor response, so an arbitrary value of $10^{-6} \text{ cm}^2 \text{ s}^{-1}$ was assigned to the species inside the membrane.^{22,23} Last, fast electrode kinetics were assumed by assigning an arbitrarily high exchange current density value, $j_0 = 10^3 \text{ A m}^{-2}$, both at the anode and at the cathode.

The biosensor response was simulated using a fixed polarization potential of 0.4 V. Figure 4.3 shows a comparison of the experimental and simulated current results taken at $t=30 \text{ s}$. The excellent agreement between both sets of data supports the validity of the model.

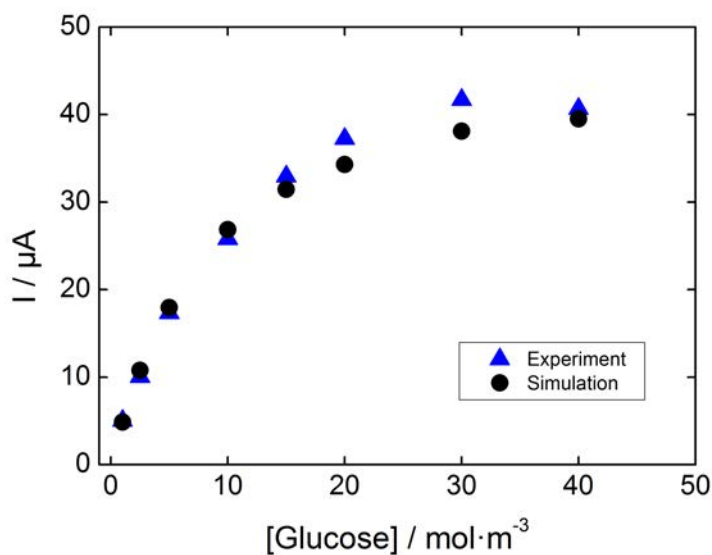
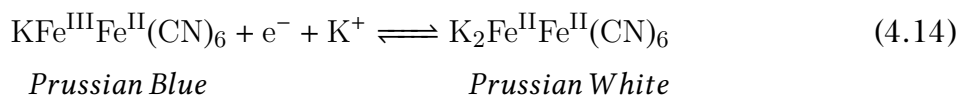


Figure 4.3: Comparison of the experimental amperometric calibration curve (blue triangles) and the simulated curve (black circles).

4.4.2 Electrochromic display / Cathode

The cathode consists of a modified electrode featuring a reversible electrochromic coating. Experimentally, this was a thin, homogeneous Prussian Blue layer electrodeposited on the surface of a transparent ITO electrode (see Section 3.2.2). Prussian Blue is a well-known inorganic electrochromic material displaying several electrochemical equilibria and their corresponding colour changes.²⁴ The present work focuses on the changes occurring at a potential around 0.2 V vs Ag/AgCl and which corresponds to the beginning of the reduction from the characteristic blue form to its colourless state. This process involves not only electron transfer at the electrode but also cation exchange with the solution, as represented in the following equilibrium:



A surface-bound reversible redox system was implemented in the model to represent the PB coating. The diffusion coefficient of the electrochromic species was fixed at $10^{-10} \text{ cm}^2 \text{ s}^{-1}$, according to previous works.²⁵

Experimental voltammetric data were used to determine the surface concentration of electroactive material on the electrode. The charge under oxidation and reduction peaks was recorded at a scan rate of 5 mV s^{-1} . Divided by the electrode area, the charge under the peaks yielded the surface concentration that was subsequently used in the simulations. The exchange current density, j_0 , was adjusted by fitting the experimental data of the cyclic voltammograms of Prussian Blue and the experiments under constant current to the simulations. A value of $2 \times 10^4 \text{ A m}^{-2}$ was implemented, reflecting the particular high electron transfer rate of the adsorbed system.

Data interpretation: relating simulation and experiment

To study the *iR* drop effects on colour switch position and definition in the electrochromic system, it is important to clarify first the link between the simulation results, which consist of concentration profiles, and those from experiments carried out in Chapter 3, which involved the use of images of the colour front evolution of the actual display. Electrochromic materials change colour as a function of electrochemical potential, which relates to the concentration of different oxidation states through the corresponding Nernst equation. This means that knowledge of the concentration profiles for the surface oxidized or reduced species suffices to establish a relation with the colours observed experimentally.

Figure 4.4 shows the effects of electrolyte conductivity, *iR* drop, and current distribution on the way in which the electrochromic material undergoes reduction. Panels *a-c* in Figure 4.4 shows concentration profiles of surface-bound electroactive species at three

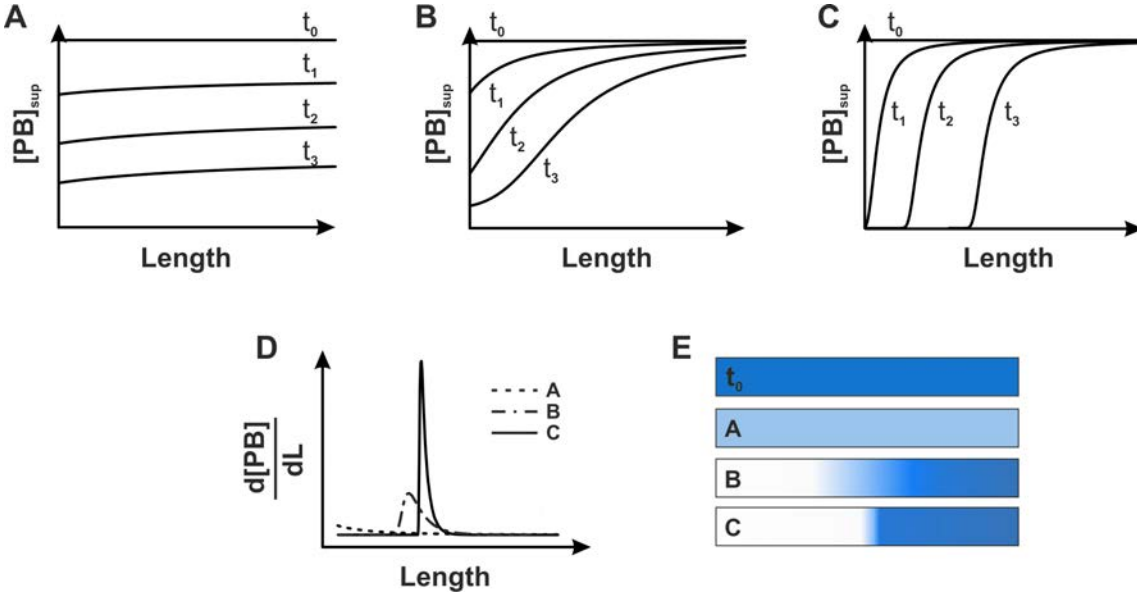


Figure 4.4: Concentration profiles of PB for (A) low, (B) moderate, and (C) high iR drop. (D) Plot of the derivative of the superficial concentration of PB corresponding to the displays with low ‘A’, moderate ‘B’, and high ‘C’ internal resistance. (E) Schematic representation of the electrochromic display at $t = 0$ (deep blue) and after operation under the cases of different internal resistance in (D).

different times during the simulation of a constant applied current experiment under three different iR drop conditions. For this experiments, iR drop was controlled through the electrolyte volume extending over two coplanar electrodes.

The resistance inside the channel can be defined as:

$$R = \frac{1}{\sigma} \frac{l}{A} \quad (4.15)$$

where σ is the conductivity of the electrolyte, l is the length of the conductor, and A is the cross-sectional area of the channel. Increasing the volume of the solution over the electrodes increases the sectional area, A , and the resistance is lowered.

Figure 4.4 shows the concentration profiles obtained for an electrode immersed in a solution with ‘infinite’ volume; that is, the current lines are unrestricted and distributed homogeneously over the entire electrochromic electrode. Under these circumstances, the bound electroactive species is consumed at nearly the same rate across the entire electrode surface, and the concentration profiles are almost flat as seen in Figure 4.4A. If the solution volume over the electrodes decreases, solution resistance increases, and the concentration profiles show the progressive consumption of material along the path of least internal resistance as seen in Figure 4.4B for a case of moderate internal resistance, and Figure 4.4C for a case of high internal resistance.

These concentration profiles were used to determine the position of the colour front and its width, which was used to represent the colour smeariness. The position of the

front can be determined by means of the first derivative of the concentration profile curve (Figure 4.4D), which is related to the current density by the expression:¹

$$\frac{\partial C}{\partial x} = \frac{i}{nFDA} \quad (4.16)$$

where C is the concentration of the electrochromic species, and x represents the direction normal to the electrode. Thus, the peak appearing in this representation shows the point where the current density is maximum at the electrode, which can be a way to define the colour front position more accurately. The peak shape, on the other hand, provides a qualitative image of the iR drop distribution at the colour front. Thus, sharp peaks with a short tail are a sign of ‘significant’ iR drop, while cases of ‘moderate’ iR drop are related to broad peaks with long tail (Figure 4.4D-E).

Figure 4.4E shows the way in which colour may be perceived by an observer in each of the three cases depicted in Figure 4.4D. Accuracy in the determination of the maximum current density area or colour edge is thus affected by the magnitude of the iR drop present in the system but also, and equally important, by the user’s perception. While the latter can be easily overcome by means of image analysis software, controlling the iR drop of the system can be a much harder challenge. Out of the many design possibilities available, one might think about narrowing the working range of the device or introducing more advanced geometries.

The above mentioned seems to imply that the higher the iR drop the better, because sharper colour fronts are favored. It is important to bear in mind that a too high iR drop is likely to render the self-powered device inoperative, as the magnitude of the drop exceeds the potential difference between anode and cathode, as will be discussed below.

Modelling a galvanostatic experiment

This section aims (i) to show that concentration profiles are a straightforward way to interpret electrochromic phenomena and (ii) to study the effect of iR drop on applied potential under constant current conditions.

A constant current experiment was simulated in which current was injected through the anode and the depletion of the electrochromic material at the cathode was studied. Simulations considered the case of an electrolyte conductivity of 1 S m^{-1} , similar to that of a supporting electrolyte solution commonly used in bioanalytical experiments. To validate the numerical model for the electrochromic display, different current levels were simulated, corresponding to the currents registered in the amperometric experiment displayed in Figure 4.3. As the electric current flows through the system, the Prussian Blue on the cathode is progressively bleached to Prussian White. The full conversion under a maximum applied current of $40 \mu\text{A}$ took place after 30 s, and the colour front position was determined at this time on passage of lower current levels. Figure 4.5 shows the plot

of distance converted of the display against applied current. Barring some minor differences arising from experimental error, theory and experiment seem to be in excellent agreement.

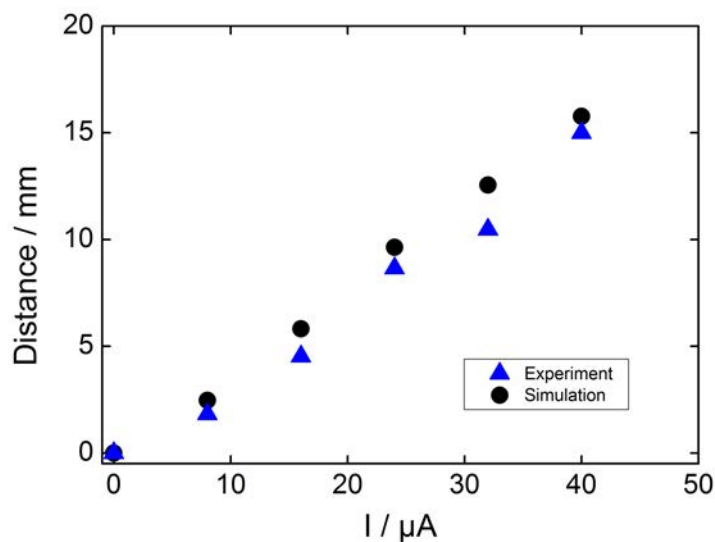


Figure 4.5: Plot of the distance converted of the display for different levels of current. Experimental data (blue triangles) and simulated data (black circles).

During these constant current experiments, the cathode potential is free to take whatever value is required in order to overcome the iR drop at each point on the electrode surface to sustain the current. This results in the observation of large potential differences between electrodes and even from one position to another within a given electrode. While this is not a problem in the simulations, which are only concerned with the redox reaction of Prussian Blue, care must be taken when dealing with real experimental conditions where other processes may be involved, resulting in unwanted reactions that may damage the device, as the overoxidation of Prussian Blue into Prussian Yellow.²⁶

Figure 4.6A shows the distance converted of the display with time and the respective cell voltage change under a constant applied current of $40 \mu\text{A}$. As expected from Ohm's law, the transient evolution of length converted and the cell voltage follow a linear relation. Moreover, since the electrolyte conductivity is assumed to be constant, the potential drop in the zone where the colour switch happens is constant throughout the experiment, and a homogeneous colour front is always observed as shown by the peaks of the derivative curves in Figure 4.6B, which are essentially identical. In summary, the colour front under constant current conditions advances at a constant rate, and its width depends on the magnitude of the applied current. However, the current in the final device does not remain constant throughout the experiment, but it will be affected by the analyte concentration

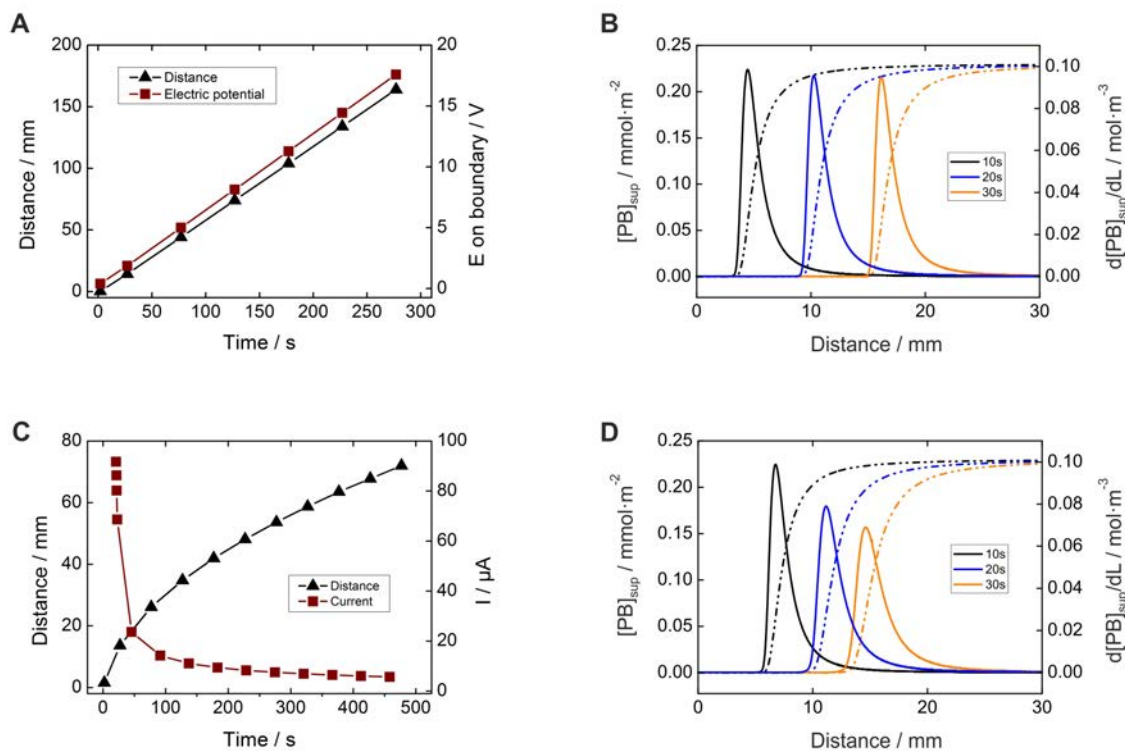


Figure 4.6: Galvanostatic (A–B) and potentiostatic (C–D) experiments. (A) Plots of the distance consumed of the display (black triangles) and the potential at the boundary electrolyte-electrode (red squares) with time. (B) Evolution of the superficial concentration of PB with time and the corresponding derivatives. (C) Plots of the distance consumed of the display (black triangles) and the current intensity (red squares) with time. (D) Evolution of the superficial concentration of PB with time and the corresponding derivatives.

as well as by variations in the iR drop.

Modelling a potentiostatic experiment

The case of a potentiostatic experiment, where a constant electric potential is applied between the two electrodes, represents a closer approximation to what happens in an actual self-powered device. This is because it considers the effect of an increasing internal resistance on the electrochemical process taking place at the cathode.

A constant voltage of 1 V was arbitrarily applied from the unmodified anode to induce the conversion of Prussian Blue into Prussian White at the cathode. The resulting behaviour is markedly different from the case of a constant current. In the galvanostatic experiment the potential at the cathode was free to adjust until all the electroactive material was consumed. In the potentiostatic experiment, on the other hand, the electrochromic material at the cathode is consumed until the internal resistance offsets the electrochemical potential at the cathode, and the electrode process slowly stops. The colour front does not progress following a linear relationship anymore, as shown in Figure 4.6C. This is be-

cause, as the internal resistance progressively increases, the potential observed by the cathode changes, affecting the conversion rate of the electrochromic material. A situation is eventually reached in which the increasing internal resistance is dominated by electrolyte resistance across a long interelectrode distance, causing the current to drop as a result of an insufficient electrochemical potential, thus widening the colour front as shown by the peaks represented in Figure 4.6D. A similar behaviour is observed at the self-powered device, where the colour front slows its advance at different positions as a consequence of the progressive increase in the internal resistance.

4.4.3 Self-powered electrochromic biosensor

After studying the two components of the device independently, the behaviour of the self-powered device was also simulated, evaluating the colour switch of the display after 30 s, as done with the actual device. The simulation was done by poisoning both electrodes at a constant potential of 0 V. This means that the system is shorted and it delivers its maximum current. The experiment was simulated under conditions of a constant medium conductivity of 1 S m^{-1} , using different glucose concentrations to match the actual experimental conditions.

Figure 4.7 shows that, despite slight discrepancies likely due to error in the visual determination of the colour front position, the agreement between both curves is still remarkable. It is worth noting that the colour front advances a maximum distance of 6 mm after 30 seconds. This is because the potential difference between the cathode and the anode reactions is around 0.5 V, and is rapidly affected by the increasing internal resistance. The resistance growing inside the cell affects the actual potential observed at both electrodes, as presented in the previous section, diminishing the cell potential (see equation 4.17 below) as the experiment progresses. This also affects the maximum current the system can deliver, which decreases with increasing internal resistance.

The effect that the iR drop has on the system was studied. For this, simulations were carried out with different electrolyte conductivities ranging from 100 S m^{-1} , a high value that results in virtually no iR drop, to 0.01 S m^{-1} , a low value under which iR drop is very significant. Figure 4.8 shows a number of linear sweep voltammograms for the same anode and cathode simulated under different electrolyte conductivities.

These voltammograms show that, as expected,²⁷ the electrochemical response at both electrodes is heavily influenced by the magnitude of the iR drop present. On one hand, the current peak potentials shift toward each other. On the other hand, the peak currents decrease with increasing internal resistance. Figure 4.9 shows a graph of the maximum current of the anode as a function of the electrolyte conductivity for the galvanic system of Figure 4.8. These voltammograms and maximum current plots were obtained for a system modelled with a homogeneous current distribution, that is with a geometry where

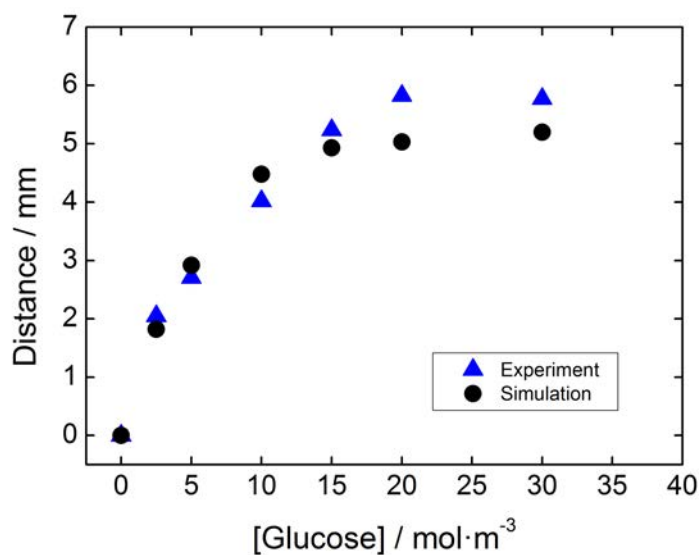


Figure 4.7: Calibration curves for the self-powered device. Experimental (blue triangles) and simulated (black squares).

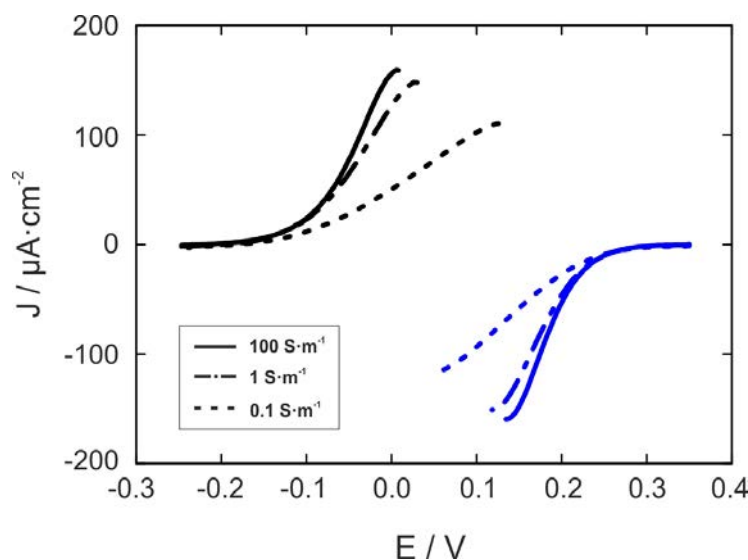


Figure 4.8: Simulated linear sweep voltammograms of the anode (black lines) and cathode (blue lines) under different electrolyte conductivities.

anode and cathode face each other, and the conductivity of the electrode was used as the main parameter affecting internal resistance. However, the results can be extrapolated to the model system in which conductivity is constant but internal resistance changes as a function of distance. The effective potential observed by both electrodes shifts as the experiment progresses, causing the cell voltage, ΔE_{cell} , to decrease and dragging the current down. This current decrease slows the conversion and results in a widening of the

colour front as a result of the low iR value.

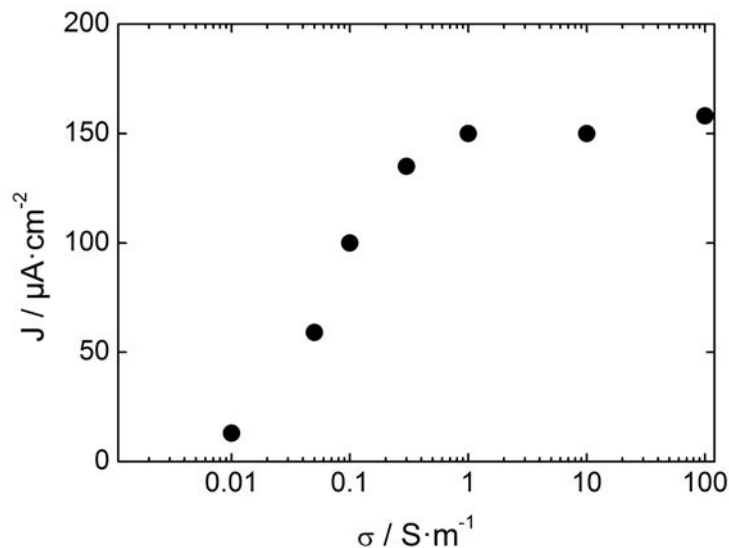


Figure 4.9: Limiting current density plot as a function of supporting electrolyte conductivity.

4.4.4 Design aspects in self-powered devices

The previous section described the impact of iR drop effects on the behaviour of the electrochromic displays as well as on the self-powered device. Simulations have enabled to understand the system behaviour, and will be used in the future for design purposes.

When the device is configured as a self-powered biosensor, its behaviour is controlled by the internal resistance inside the cell, which affects the conversion rate and colour front width. The device cell voltage is defined as:

$$\Delta E_{cell} = E_{cat} - E_{ano} - iR \quad (4.17)$$

where E_{cat} and E_{ano} are the potentials of the cathode (display) and the anode (biosensor), respectively. An electric current flows at positive cell voltages, turning Prussian Blue into Prussian White, while the mediator at the biosensing anode is oxidized. As the electrochromic material on the display is consumed, the internal resistance between the unconverted Prussian Blue and the redox mediator increases, reaching a point where the cell potential approaches zero. At this point, the current drops and the colour front becomes blurrier until the system appears to have come to a halt. Although the electrode processes continue, their rate is markedly diminished due to the small overpotential, causing the current to drop to almost zero.

Equations 4.15 and 4.17 point at three ways to control the performance of the device: (i) by choosing adequate electrode processes, (ii) by selecting the right electrolyte conductivity, and (iii) by designing a suitable cell geometry.

The following results were obtained from simulations using a fixed glucose concentration of 5 mol m^{-3} , which falls in the lower range of concentrations where the current output is low and a sluggish and less clear colorimetric response is obtained. The response time is fixed as in the previous experiments at 30 seconds.

Effect of formal cell potential

Figure 4.10 shows the effect that increasing the formal potential of the electrochromic species, E_{cat} , has on the colorimetric response. As expected, with higher formal potentials, and thus higher cell voltages, the cathode region undergoing colour change becomes larger as the cell is able to sustain higher internal resistance levels. Once this internal resistance becomes equal to or higher than the potential difference between the cathode and anode reaction 4.17, the regeneration of the redox mediator is stopped and the enzymatic reaction ceases, in line with the potentiostatic experiment. The maximum current, which is controlled by the biosensing anode, will decrease, as described, earlier unless the formal potential remains sufficiently high throughout the experiment. As seen with the error bars in Figure 4.10A representing the size of the colour gradient of the switch, the colour front remains essentially unaltered, regardless of the overall cell potential, as the *iR* drop at the colour front is almost constant. However, a clear improvement can be observed in the distance converted as it increases with the cell voltage, reaching a maximum at around 600 mV, a value that current biofuel cells can achieve.^{28,29}

The onset of the oxygen reduction process sets a natural limit at the anode, so using redox mediators with formal potentials below -0.2 to -0.3 V vs SCE does not make much sense in oxidase-based systems (the formal potential of the FAD group in glucose oxidase is around -0.5 V vs SCE³⁰). In the case of the cathode, it may be possible to find electrochromic materials with formal potentials higher than that of the couple Prussian Blue/Prussian White, although they may not be as friendly to work with.³¹

Effect of electrolyte conductivity

Figure 4.10B shows the effect of electrolyte conductivity on a system with a cell voltage of 200 mV, according to the experiment. The conductivities covered in the study range between 0.1 S m^{-1} , characteristic of solid-gel polymeric electrolytes,³² and 1.25 S m^{-1} , which is more typical of conventional liquid electrolytes. Conductivity variations translate into changes in the internal resistance, as seen in equation 4.15, which ultimately affect the behaviour of the display. Higher electrolyte conductivities result in lower internal resistance, which facilitates higher degrees of colour conversion in the cell; however, the lower

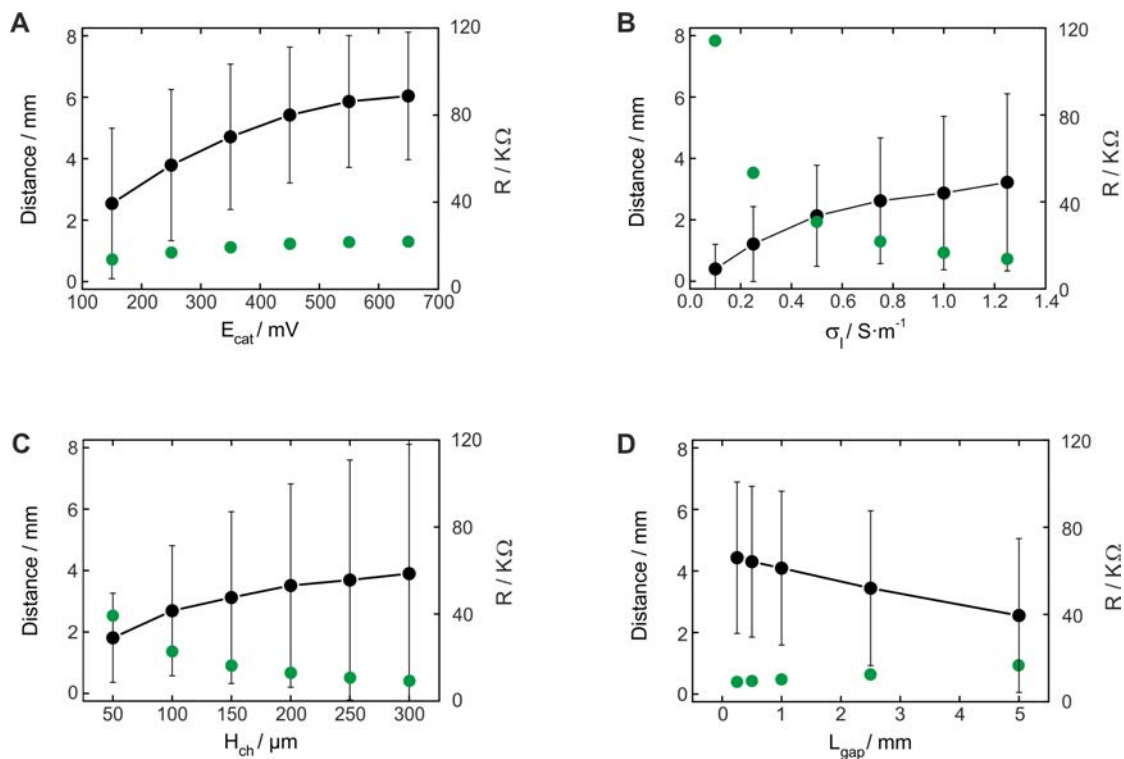


Figure 4.10: Plots of the length converted (black dots), the corresponding internal resistance (green dots), and the colour front definition (error bars) against the parameter evaluated: (A) Formal potential of the electrochromic species, (B) electrolyte conductivity, (C) paper thickness, and (D) anode—cathode separation distance.

internal resistance generates a wider and blurrier colour front. In other words, in the case of a sensing device, conductivity provides a trade off between sensitivity and accuracy.

Low conductivity media, which leads to narrower colour fronts at high current levels, may be a feasible choice in cases where power availability is not an issue, but may be a poor choice in self-powered devices (and power sources in general). Although lower conductivities result in higher resistances that keep the current more focused, they will also require larger potential differences between electrodes to overcome the corresponding iR drop levels as seen in Figure 4.10B.

Effect of cell geometry

Cell geometry covers several design parameters such as electrode size and shape, inter-electrode separation, and channel aspect ratio. The last two parameters were evaluated because they play a key role in the behaviour of the electrochromic display.

The height of the channel containing both electrodes was studied using values up to several hundreds of micrometers, which are typical magnitudes in displays and in miniaturized devices in general. The modification of the channel height containing the elec-

trodes affects the current distribution inside the device and, therefore, the current path inside the channel. The results in this case are similar to those obtained when electrolyte resistance was changed. As the cross-sectional area of the device is increased, internal resistance decreases, facilitating the flow of electric current and thus achieving larger extensions of colour conversion, as seen in Figure 4.10C. However, the current is more homogeneously distributed across the surface of the electrochromic display, so the colour front becomes more diffuse.

Last, the effect the anode—cathode separation distance has on the device performance was also studied. Different distances were tested, ranging from a few hundred micrometers to a few millimeters. As the separation distance increases, the *iR* drop inside the channel increases too, leading to a more sluggish conversion of the PB display (Figure 4.10D). As in the first case, where the formal potentials were tested, the internal resistance at the switching zone remains almost constant due to the small contribution of the increasing length between the PB and the anode in equation 4.15, which leads to an unaltered colour front.

The importance of cell geometry is that it can help the designer overcome certain limitations imposed by the materials, the sensing anode, the device work environment, or the fabrication processes.

4.5 Conclusions

This work has shown how *iR* drop can be used as a design factor in electrochromic devices, as a means to control the degree of colour conversion. The present work has presented a numerical tool intended for the exploration of the effects of internal resistance on the performance of self-powered devices based on the combination of electrochromic materials and biosensors. However, the scope of this work goes much further as it can serve as a design tool of interest not only for these type of devices but also for other devices involving electrochromic materials such as displays and smart glasses, and in miniaturized power-generation devices in general where internal resistance losses are clearly detrimental to their performance.

Some fundamental insights can be gained already from equation 4.15 and particularly from equation 4.17, which provide the first approach for understanding the behaviour of these systems and their design. However, these simplified approaches fall short in complex systems like the one described here, where the net observed behaviour results from the combination of different phenomena occurring in each component of the system. This is when finite element tools have a significant advantage by providing solutions that better reflect these interactions. The model presented here accounts for three key design parameters, namely, electrode processes, electrolyte resistance, and cell geometry. The model

enables the exploration of different conditions so that specific applications can be better designed, considering the limitations imposed by materials and fabrication processes. In the case of the self-powered electrochromic biosensors studied in this chapter, this tool can serve to design devices that can operate within a desired concentration range, ensuring that the resulting colour changes can be observed easily and unambiguously by the naked eye. The limitations facing these self-powered devices may be solved mainly with suitable formal potentials. On the other hand, conventional electrochromic devices such as displays and smart windows, which account for most of the applications involving electrochromic materials, can also benefit from the inclusion of iR drop as a design parameter for the fabrication of multicolour devices or for the modulation of the radiation filtering abilities in smart glasses.

Bibliography

- [1] Bard, A. J.; Faulkner, L. R. *Electrochemical methods: fundamentals and applications*; John Wiley & Sons, New York, 2001.
- [2] Nam, J.-Y.; Kim, H.-W.; Lim, K.-H.; Shin, H.-S.; Logan, B. E. Variation of power generation at different buffer types and conductivities in single chamber microbial fuel cells. *Biosens. Bioelectron.* **2010**, *25*, 1155–1159.
- [3] Dickinson, E. J. F.; Limon-Petersen, J. G.; Rees, N. V.; Compton, R. G. How much supporting electrolyte is required to make a cyclic voltammetry experiment quantitatively “diffusional”? A theoretical and experimental investigation. *J. Phys. Chem. C* **2009**, *113*, 11157–11171.
- [4] Forster, R. J. Microelectrodes: new dimensions in electrochemistry. *Chem. Soc. Rev.* **1994**, *23*, 289–297.
- [5] Arrigan, D. W. M. Nanoelectrodes, nanoelectrode arrays and their applications. *Analyst* **2004**, *129*, 1157–1165.
- [6] Amatore, C.; Maisonhaute, E.; Simonneau, G. Ultrafast cyclic voltammetry: performing in the few megavolts per second range without ohmic drop. *Electrochem. Commun.* **2000**, *2*, 81–84.
- [7] Rees, N. V.; Klymenko, O. V.; Maisonhaute, E.; Coles, B. A.; Compton, R. G. The application of fast scan cyclic voltammetry to the high speed channel electrode. *J. Electroanal. Chem.* **2003**, *542*, 23–32.
- [8] Kawahara, J.; Ersman, P. A.; Engquist, I.; Berggren, M. Improving the color switch contrast in PEDOT:PSS-based electrochromic displays. *Org. Electron.* **2012**, *13*, 469–474.
- [9] Shen, D. E.; Österholm, A. M.; Reynolds, J. Out of sight but not out of mind: the role of counter electrodes in polymer-based solid-state electrochromic devices. *J. Mater. Chem. C* **2015**, *3*, 9715–9725.
- [10] Cooper, J. A.; Compton, R. G. Channel electrodes — A Review. *Electroanalysis* **1998**, *10*, 141–155.
- [11] Katz, E.; Bückmann, A. F.; Willner, I. Self-powered enzyme-based biosensors. *J. Am. Chem. Soc.* **2001**, *123*, 10752–10753.
- [12] Wang, J. Electrochemical glucose biosensors. *Chem. Rev.* **2008**, *108*, 814–825.

- [13] Michaelis, L.; Menten, M. L. Die kinetik der invertinwirkung. *Biochem. Z.* **1913**, *49*, 333–369.
- [14] Battaglini, F.; Calvo, E. J. Digital simulation of homogeneous enzyme kinetics for amperometric redox-enzyme electrodes. *Anal. Chim. Acta* **1992**, *258*, 151–160.
- [15] Cass, A. E. G.; Davis, G.; Francis, G. D.; Hill, H. A. O.; Aston, W. J.; Higgins, I. J.; Plotkin, E. V.; Scott, L. D. L.; Turner, A. P. F. Ferrocene-mediated enzyme electrode for amperometric determination of glucose. *Anal. Chem.* **1984**, *56*, 667–671.
- [16] Yokoyama, K.; Kayanuma, Y. Cyclic voltammetric simulation for electrochemically mediated enzyme reaction and determination of enzyme kinetic constants. *Anal. Chem.* **1998**, *70*, 3368–3376.
- [17] Kulys, J.; Tetianec, L.; Bratkovskaja, I. Pyrroloquinoline quinone-dependent carbohydrate dehydrogenase: Activity enhancement and the role of artificial electron acceptors. *Biotechnol. J.* **2010**, *5*, 822–828.
- [18] Fick, A. Uber diffusion. *Journal of Science* **1855**, *16*.
- [19] Dickinson, E.; Limon-Petersen, J.; Compton, R. The electroneutrality approximation in electrochemistry. *J. Solid State Electrochem.* **2011**, *15*, 1335–1345.
- [20] Newman, J.; Thomas-Alyea, K. E. *Electrochemical systems*; John Wiley & Sons, New Jersey, 2004.
- [21] Harrison, D. J.; Turner, R. F. B.; Baltes, H. P. Characterization of perfluorosulfonic acid polymer coated enzyme electrodes and a miniaturized integrated potentiostat for glucose analysis in whole blood. *Anal. Chem.* **1988**, *60*, 2002–2007.
- [22] Harnisch, F.; Warmbier, R.; Schneider, R.; Schröder, U. Modeling the ion transfer and polarization of ion exchange membranes in bioelectrochemical systems. *Bioelectrochemistry* **2009**, *75*, 136–141.
- [23] Sel, O.; Kim, L. T. T.; Debiemme-Chouvy, C.; Gabrielli, C.; Laberty-Robert, C.; Perrot, H. Determination of the diffusion coefficient of protons in nafion thin films by ac-electrogravimetry. *Langmuir* **2013**, *29*, 13655–13660.
- [24] Monk, P.; Mortimer, R.; Rosseinsky, D. *Electrochromism and electrochromic materials*; Cambridge University Press, Cambridge, 2007.
- [25] Garcia-Jareno, J. J.; Sanmatias, A.; Navarro-Laboulais, J.; Vicente, F. Chronoamperometry of prussian blue films on ITO electrodes: ohmic drop and film thickness effect. *Electrochim. Acta* **1999**, *44*, 4753–4762.

- [26] Itaya, K.; Ataka, T.; Toshima, S. Spectroelectrochemistry and electrochemical preparation method of Prussian blue modified electrodes. *J. Am. Chem. Soc.* **1982**, *104*, 4767–4772.
- [27] Henley, I.; Fisher, A. Computational electrochemistry: a model to studying ohmic distortion of voltammetry in multiple working electrode, microfluidic devices, an adaptive fem approach. *Electroanalysis* **2005**, *17*, 255–262.
- [28] Zebda, A.; Gondran, C.; Goff, A. L.; Holzinger, M.; Cinquin, P.; Cosnier, S. Mediatorless high-power glucose biofuel cells based on compressed carbon nanotube-enzyme electrodes. *Nat. Commun.* **2011**, *2*, 1–6.
- [29] Pinyou, P.; Conzuelo, F.; Sliozberg, K.; Vivekananthan, J.; Contin, A.; Pöllner, S.; Plumeré, N.; Schuhmann, W. Coupling of an enzymatic biofuel cell to an electrochemical cell for self-powered glucose sensing with optical readout. *Bioelectrochem.* **2015**, *106*, 22–27.
- [30] Cai, C.; Chen, J. Direct electron transfer of glucose oxidase promoted by carbon nanotubes. *Anal. Biochem.* **2004**, *332*, 75–83.
- [31] Beaujuge, P. M.; Reynolds, J. R. Color control in π -conjugated organic polymers for use in electrochromic devices. *Chem. Rev.* **2010**, *110*, 268–320.
- [32] Quartarone, E.; Mustarelli, P. Electrolytes for solid-state lithium rechargeable batteries: recent advances and perspectives. *Chem. Soc. Rev.* **2011**, *40*, 2525–2540.

5

Screen-printed Prussian Blue electrodes

The electrochromic sensor presented in Chapter 3 relied on a thin layer of Prussian Blue electrodeposited on a transparent ITO-glass electrode. However, electrodeposition can be a major drawback in terms of cost and manufacturing scalability. This chapter presents the development of an electrochromic paste based on Prussian Blue and suitable for screen-printing. This paste aims at eliminating the need for a transparent electrode as well as an electrodeposited display, beginning the transition toward simpler electrochromic sensing devices.

The content of this chapter has been previously published in the following article:

- Pellitero, M.A., Colina, Á., Villa, R., del Campo, F.J.; *Antimony tin oxide (ATO) screen-printed electrodes and their application to spectroelectrochemistry*, **Electrochemistry Communications**, 2018, 93, 123–127.

and in the following manuscript:

- Pellitero, M.A., Fremeau, J., Villa, R., Lakard, B., Hihn, J-Y., del Campo, F.J.; *Electrochromic biosensors based on screen-printed Prussian Blue electrodes*, **Sensors and Actuators B: Chemical**, 2019, submitted (under revision).

5.1 Introduction

Since its discovery in 1704 by Diesbach,¹ Prussian Blue has gained much attention, not only by its chemical properties but also by its use in the formulation of paints and inks (Figure 5.1A).

Prussian Blue consists of iron (II) and (III) atoms bridged by cyanide groups in a cubic crystal structure of formula $Fe_4^{III}[Fe^{II}(CN)_6]_3$ (Figure 5.1B).² This composition and structure bestow Prussian Blue its characteristic optical and electrochemical properties.³

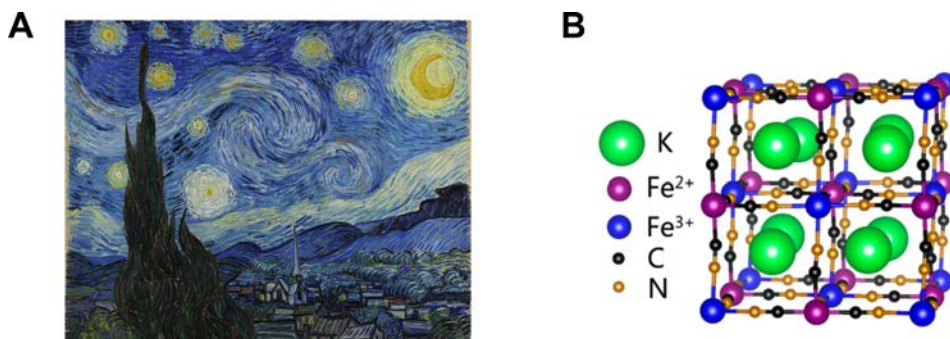


Figure 5.1: (A) The Starry Night by Vincent van Gogh, 1889. (B) Crystal structure of Prussian Blue. Figure adapted with permission from⁴

In addition to its electrochromic behaviour, Prussian Blue also displays catalytic properties towards the reduction of oxygen and hydrogen peroxide, something that has been exploited in the development of first-generation oxidase-based electrochemical⁵ and optical biosensors.⁶ The use of Prussian Blue as sensing material has led to a boost in the design and fabrication of electrodes modified with this material.

Regarding the preparation of PB-modified electrodes, there are three main ways:

- Electrodeposition.
- Chemical growth.
- Deposition of PB-modified graphite pastes.

Electrodeposition. Since it was first reported by Neff,² electrodeposition has been the preferred method when it comes to developing electrochromic devices and electrochemical sensors based on PB. The main advantages of electrodeposition methods are not only the selective growth on electrode surfaces alone, but also the control of growth conditions. This ultimately means controlling device-critical features such as film thickness, roughness, porosity, and stability.⁷ Deposition methods based on potentiostatic,⁸ galvanostatic,² cyclic,⁹ and pulse voltammetry¹⁰ control have been reported. Most of them consist in the application of a reducing potential at the working electrode immersed in a solution of Fe(III) and ferricyanide in dilute HCl. Ferrocyanide produced at the electrode

readily reacts with the free Fe(III) ions in solution, leading to the formation of Prussian Blue.

Chemical growth. Another way used to produce Prussian Blue films, both on electrodes^{11,12} and on inert surfaces, is by chemical growth.¹³ However, this is not an ideal approach either. Although chemical deposition greatly simplifies material synthesis by avoiding electrochemical instrumentation, it lacks the surface selectivity and much of the control that electrochemical methods provide. However, chemical synthesis of PB is used in the formulation of screen-printing materials, which is the third relevant approach for the production of PB-modified electrodes.

Deposition of PB-modified graphite pastes. Up until the mid 1990s, most electrochemical studies on Prussian Blue used electrodeposited films.^{14–16} However, the use of chemically synthesized Prussian Blue has been made popular through the introduction of carbon paste¹⁷ and screen-printed electrodes (SPEs).¹¹ PB-modified pastes represent a straightforward way to overcome critical production issues affecting electrodeposition, such as the batch nature of the electrodeposition process and its relatively high cost. Screen-printing turns a batch into a continuous, large area process, and extends the nature of possible substrates beyond conducting electrode materials to include paper,¹⁸ textiles,¹⁹ ceramics,²⁰ polymers,²¹ and nearly any material imaginable.

PB-modified pastes have typically three key components: a conducting material, the PB itself, and a suitable binder. In this work, PB was chemically grown over the surface of conducting particles, and then mixed with a Viton® binder system to produce an electrochromic paste. The main difference between this paste and others previously reported is that, instead of graphite, either SiO₂ microparticles coated with an antimony-doped tin oxide (ATO) layer, or indium-doped tin oxide (ITO) nanoparticles were used as conducting material. Because these particles are clear in colour — SiO₂-ATO is a grey powder, and ITO is pale-yellow (Figure 5.2) — it is possible to observe the electrochromism of PB at the resulting electrodes.



Figure 5.2: Image with the powders of the two tin oxide-based particles used for the modification with Prussian Blue. (A) SiO₂-ATO, (B) ITO.

Although this material had been previously described for the fabrication of displays,²² it has never hitherto been used to build electrochromic sensors. This chapter evaluates the use of these pastes for the fabrication of electrochromic devices and looks at their spectroelectrochemical performance.

5.2 Experimental

5.2.1 Reagents and materials

The electroanalytical devices presented here were designed using VectorWorks 2018, Student Edition (Techlimits, ES). Potassium ferrocyanide, ferrous sulfate, potassium chloride, hydrochloric acid and 2-butoxyethyl acetate were purchased from Sigma-Aldrich. SiO₂-ATO conducting particles (nominal size of 3 μm) Zelec 1610-S were kindly provided by Milliken Chemical (BE). ITO conducting particles (nominal size of 50 nm) NanoTek® were purchased from Alfa Aesar (USA). Viton® fluoroelastomer (GBL-600S, DuPont) was acquired from Eagle Elastomer (USA). 500 μm-thick polyethylene terephthalate (PET) sheets (Autostat WP20) from Mac Dermid (UK) were used as substrate for the printing of the electrochemical devices. PB-modified carbon conducting paste (C2070-424P2) was purchased from Gwent Electronic Materials LTD. (UK). Electrodag silver (725A) and photocurable dielectric (PF-455B) pastes were obtained from Henkel (ES). PB-modified screen-printed carbon electrodes (PB-SPCEs) ref. 710 were purchased from Metrohm DropSens (ES).

5.2.2 Instrumentation

A 30 W Epilog Mini 20 CO₂ Laser engraver from Laser Project (ES) was used to cut the PET substrates. Electrochemical and spectroelectrochemical measurements were done using a SPELEC instrument (Metrohm DropSens) controlled by DropView SPELEC software (version 3.0). Scanning electron microscopy images were obtained at an Auriga microscope (Carl Zeiss). A Kulicke & Soffa four-point probe connected to a 3455A Digital Voltmeter (Hewlett Packard) was used to measure the sheet resistance of the fabricated materials.

5.2.3 Electrochromic Prussian Blue pastes

Prussian Blue screen-printing pastes were prepared following a previously reported protocol.²² Briefly, 20 g of conducting ITO or SiO₂-ATO particles were suspended, under vigorous stirring, in 200 mL of a 25 mM iron (II) sulfate aqueous solution. Then, 30 mL of a 60 mM ferricyanide solution were added dropwise to the stirred solution. The re-

sulting blue particles were separated by decantation, washed with dilute HCl, and dried at 100 °C.

Prussian Blue-modified conducting particles were next combined with a 15-20 % Viton solution prepared in 2-butoxyethylacetate to a 2.5:1 pigment to binder proportion, and thoroughly mixed in a ball mill, until the resulting paste presented a honey-like texture. The particle size was estimated using a 50 μm grind gauge (Figure 5.3), obtaining a maximum particle size range between 5 and 12 μm . This is extremely good considering that the starting particle size was nominally 3 μm , and that no additives were used to promote particle suspension in the paste.



Figure 5.3: Grind gauge used for the estimation of particles size in a screen-printing paste. The appearance of grooves in the pass indicates the size of the particles mixed in the paste.

5.2.4 Electrode fabrication

The screen-printed electrodes fabricated consisted of a conventional 3-electrode design, akin to those used in most electroanalytical experiments.²³ The fabrication steps are schematized in Figure 5.4. Briefly, a conducting silver paste was used to print the conducting tracks and the pseudo-reference electrode on a PET substrate. Conducting graphite paste was used for the working and auxiliary electrodes. The working electrode was designed to have a diameter of 2.5 mm. Next, the manufactured Prussian Blue pastes were printed. Due to the high electrical resistance of the PB layer, to access the electrochromic properties of the material required printing it over a conducting substrate, the screen-printed carbon working electrode in this case. The PB layer was designed to completely cover the carbon electrode underneath, with a diameter of 3 mm. Last, a photocurable dielectric paste was used to define the electroactive area of the electrodes.

5.3 Results and discussion

The electrochemical and spectroelectrochemical performance of the PB-SPEs was evaluated and compared to that of (i) electrodes fabricated with commercial PB-Graphite paste, and (ii) to commercial PB-SPCEs (Figure 5.5). In addition to the electrochromism of the pastes presented here, which graphite electrodes lack, other differences will also be noted.

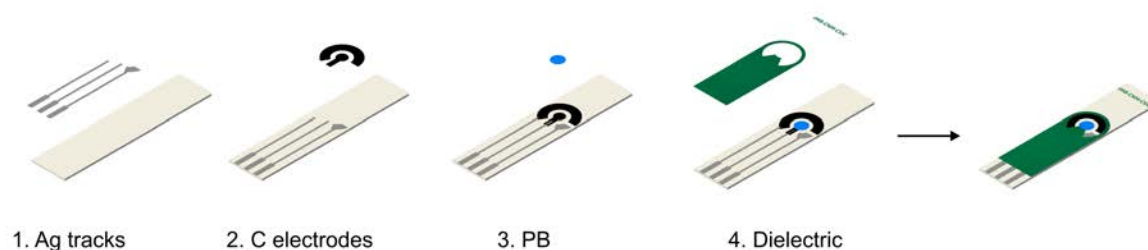


Figure 5.4: Fabrication steps of the Prussian Blue screen-printed electrodes.

5.3.1 Electrochemical characterization

Figure 5.6 shows cyclic voltammograms recorded in supporting electrolyte for the 4 types of electrode studied. Although fast electron transfer rates are observed in all cases, the most striking difference in the voltammetry of the different PB-modified pastes is the much higher currents observed for the electrochromic pastes presented here, compared to those obtained from the commercial materials. This suggests that commercial graphite pastes contain a much lower amount of Prussian Blue than the home made electrochromic pastes described here. Also, the voltammograms show that the presented PB electrodes display relatively larger background currents. The most likely reason for such currents is the large surface area of the electrodes due to their high rugosity (Figure 5.7), combined with the mild electroactivity of indium and antimony tin oxides,^{24,25} and perhaps not so much due to the modification of the conducting particles with Prussian Blue.

Table 5.1 provides a summary of peak-to-peak separation, peak current density, and charge density of all electrodes studied. The PB electrodes based on tin oxide particles exhibit a superior electrochemical behaviour based on their peak-to-peak separation compared to commercial materials based on graphite. This is probably due to a better contact

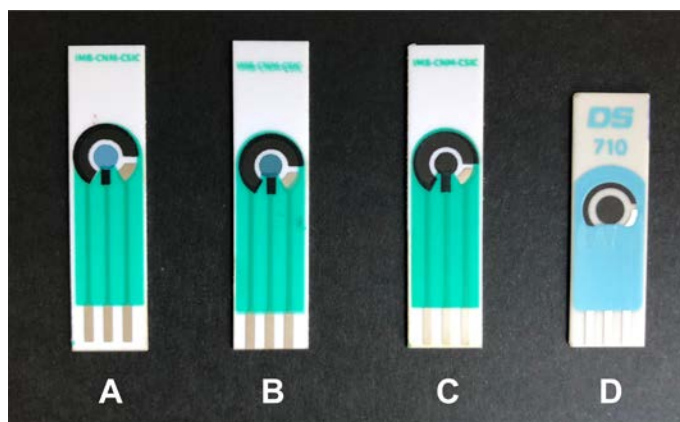


Figure 5.5: Capture of the 4 types of electrode used in this chapter. (A) SiO₂-ATO/PB, (B) ITO/PB, (C) Gwent C/PB (D) DropSens C/PB.

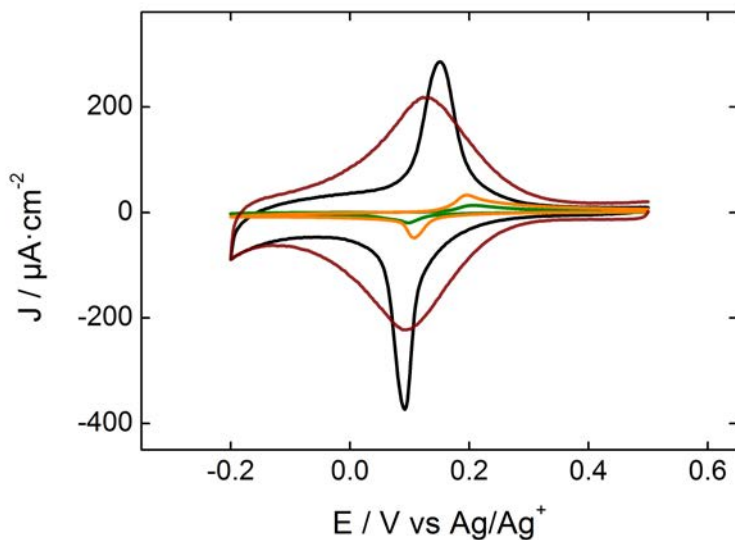


Figure 5.6: Cyclic voltammograms obtained in aqueous supporting electrolyte for the different types of PB-based electrodes. Scan rate of 5 mV s^{-1} . SiO_2 -ATO/PB (Black), ITO/PB (Red), DropSens C/PB (Orange), Gwent C/PB (Green).

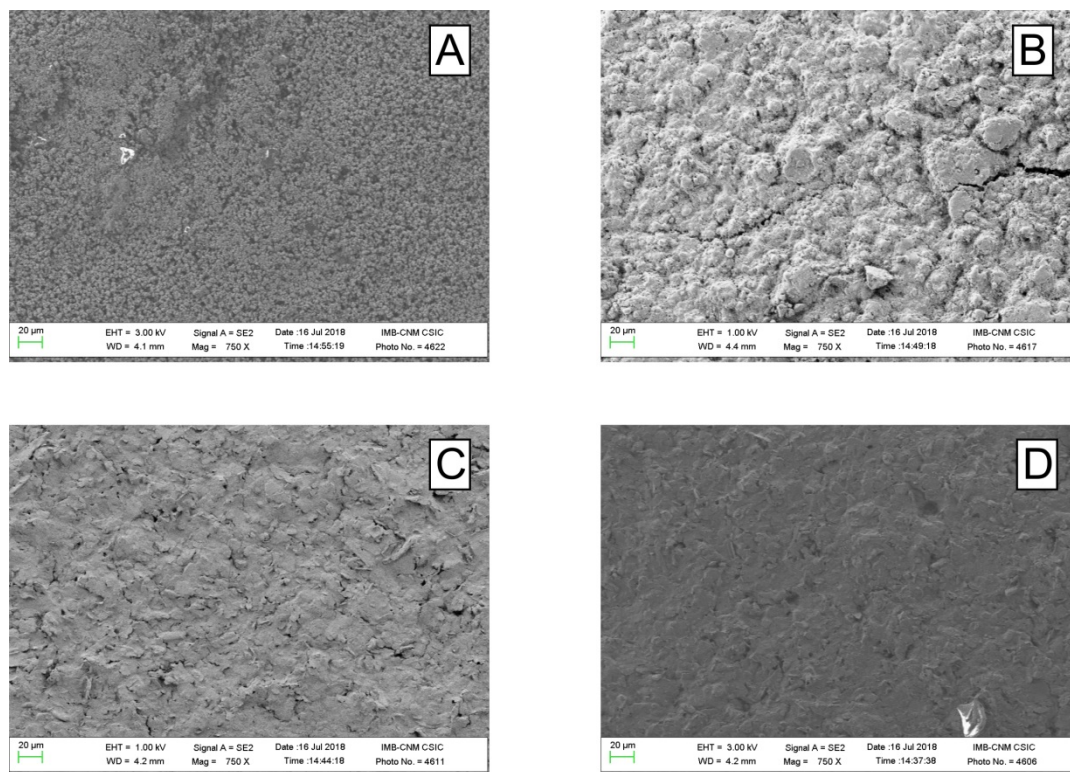


Figure 5.7: SEM images of the different electrode surfaces. (A) SiO_2 -ATO/PB, (B) ITO/PB, (C) DropSens C/PB, (D) Gwent C/PB.

of the PB and the conducting material. ITO-modified nanoparticles display the smallest peak-to-peak separation, at roughly 30 mV, presumably due to the better conductivity afforded by ITO nanoparticles compared to SiO₂-ATO/PB microparticles. However, the much higher PB loading, arising from the massive available surface area of the nanoparticles combined with the thickness of the screen-printed layer, results in much broader peaks compared to other materials.

This peak broadness, which may be detrimental for electroanalytical applications, is due to a limitation in the rate of potassium exchange during the redox process. In fact, this limitation has been observed for all four electrode types under study in the form of linear plots of peak current vs. the square root of scan rate (Figure 5.8). Such a linear dependency points at a diffusion controlled process. This was unexpected at first, given the surface-bound nature of the fabricated electrodes. But looking at the magnitude of the peak-to-peak separations in Table 5.1, typical of diffusion controlled processes, it reinforces the idea of a limitation in the electron rate transfer due to the diffusion of potassium cations inside the PB layer. In contrast, thin film electrogenerated electrodes^{26,27} exhibit a surface-controlled regime as predicted by the Laviron expression.²⁸ The reason to observe this different behaviour is in the thickness of the PB layer. While electrodeposited layers are typically in the range of nanometers (hundreds), screen-printed layers are at least a few microns thick and must exchange larger amounts of cations in order to see the electrochemical reaction.

Another important difference between graphite and tin oxide-based electrodes is their electrical conductivity. In the case of commercial materials, the presence of Prussian Blue has very little impact on the conductivity of the resulting electrodes; the datasheet of Gwent's sensor graphite paste reference C10903P14 reports a resistivity of less than 75 Ohm/square for a 25 µm thick layer, whereas the PB-modified paste, reference C20-70424P2, reports 49 Ohm/square for a similar layer. These values were compared to those obtained for the fabricated Prussian Blue pastes. For this, Prussian Blue layers of different thickness were applied using an applicator frame (Figure 5.9), and their electrical resistance was measured using a four-point probe connected to a digital voltmeter.

It was found that the resistivity of PB modified particles increased by more than 5

| | $\Delta E_p / \text{mV}$ | $J_{p,c} / \mu\text{A} \cdot \text{cm}^{-2}$ | $Q / \text{mC} \cdot \text{cm}^{-2}$ |
|--------------------------|--------------------------|--|--------------------------------------|
| SiO ₂ -ATO/PB | 60 ± 2 | 369 ± 1 | 8.9 ± 0.1 |
| ITO/PB | 31 ± 2 | 243 ± 1 | 11.0 ± 0.1 |
| DropSens/PB | 82 ± 2 | 42 ± 1 | 0.6 ± 0.1 |
| Gwent/PB | 87 ± 4 | 73 ± 7 | 1.4 ± 0.3 |

Table 5.1: Data extracted from the voltammetric experiments using the different SPEs.

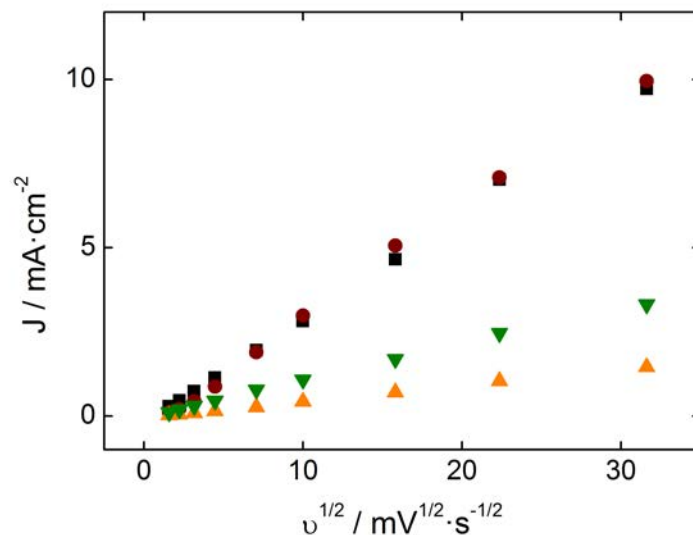


Figure 5.8: Plot of the peak current density against the square root of the scan rate of the voltammetric experiments for each type of electrode. SiO₂-ATO/PB (Black), ITO/PB (Red), Gwent C/PB (Green), DropSens C/PB (Orange).

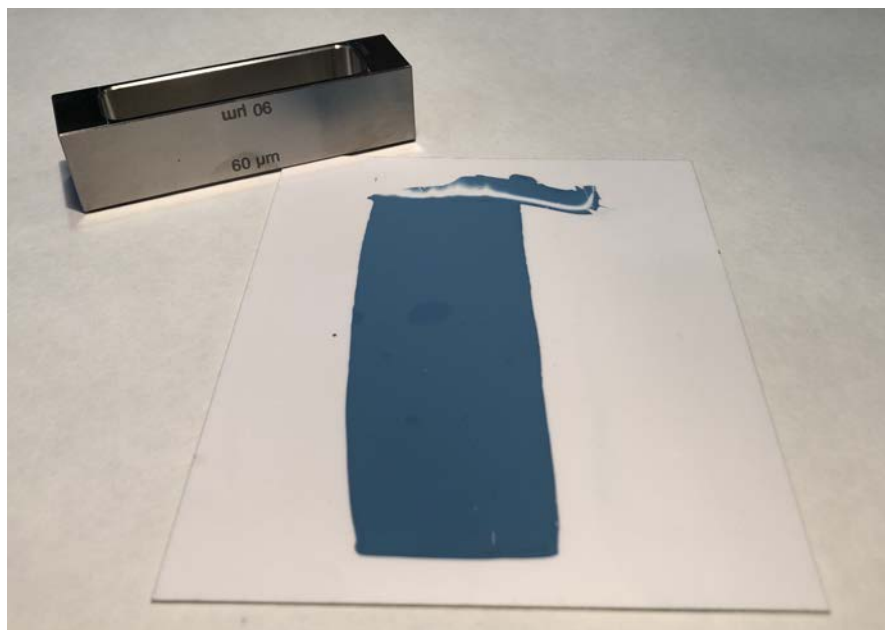


Figure 5.9: Applicator frame and test structure obtained for a Prussian Blue screen-printing paste.

times compared to a paste formulated with unmodified particles at the same concentration (Table 5.2). This suggests that commercial materials may have been produced simply by adding a small amount of PB particles to an existing graphite paste formulation, in contrast with the coated tin oxide particles (Figure 5.10), that exhibit higher signals and broader

peaks in the cyclic voltammetry, indicating a higher amount of loading of PB.

| Material | Layer thickness / μm | Resistivity / $\text{k}\Omega \cdot \text{cm}^{-1}$ |
|--------------------------|---------------------------------|---|
| SiO ₂ -ATO | 30 | 52 ± 15 |
| SiO ₂ -ATO | 60 | 47 ± 15 |
| SiO ₂ -ATO | 90 | 7 ± 2 |
| SiO ₂ -ATO | 120 | 8 ± 4 |
| SiO ₂ -ATO/PB | 30 | 207 ± 81 |
| SiO ₂ -ATO/PB | 60 | 190 ± 74 |
| SiO ₂ -ATO/PB | 90 | 38 ± 13 |
| SiO ₂ -ATO/PB | 120 | 25 ± 6 |
| ITO/PB | 30 | >10.000 |
| ITO/PB | 60 | 4280 ± 217 |
| ITO/PB | 90 | 1380 ± 165 |
| ITO/PB | 120 | 430 ± 73 |

Table 5.2: Resistivity of the pastes fabricated using the PB-coated tin oxide particles as well as the unmodified SiO₂-ATO particles.

5.3.2 Spectroelectrochemical characterization

Last, electrodes were compared using spectroelectrochemistry. Obviously, the black colour of graphite in the commercial PB-modified electrodes precluded the observation of any spectroelectrochemical changes, in contrast with the ITO and ATO based pastes presented here. Figures 5.11A and B show cyclic voltammograms of the two types of PB-SPEs together with the derivative of their respective voltabsortograms obtained by UV-vis reflectance spectroscopy using wavelengths of 675 and 700 nm for ATO and ITO-based electrodes, respectively. A clear correlation between the electrochemical and the spec-

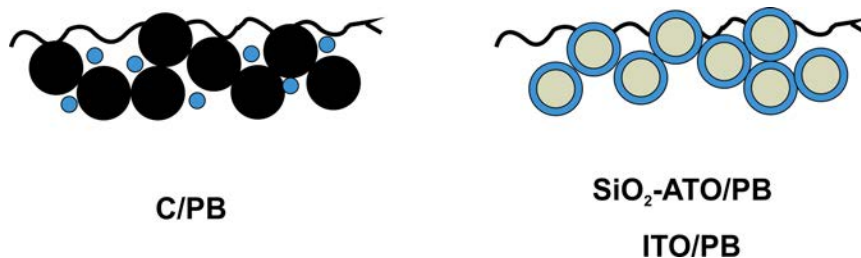


Figure 5.10: Schematic representation of the two types of PB-based screen-printing pastes.

troscopic behaviour in both types of electrodes is apparent, although a shift ca. 50 mV is observed between the two signals in ITO/PB electrodes. This shift in peak position between electrochemical and optical signals has been reported in the past and, again, is attributed to the mass transport limitations of K^+ exchange from the Prussian Blue lattice, and which is involved in the colouration process.¹⁷ In spite of this slight delay between the current and the colour change, neither the electrocatalytic performance of the material nor its electrochromism have been adversely affected.

The performance and stability of the electrochromic material under a continuous switching regime was also studied. The potential of the working electrode was stepped between -0.1 V and +0.4 V vs Ag/Ag⁺ at intervals of 60 s in a 0.25 mM H₂O₂ solution in aqueous supporting electrolyte for up to three hours. The experiment was carried out in the presence of hydrogen peroxide to simulate the stringent conditions of an oxidase-based biosensor where hydrogen peroxide is produced under neutral pH conditions, and PB is less stable than in an acidic medium.²⁹ Figure 5.11C shows the change in absorbance as reducing and oxidizing potentials are applied. The data show that ITO/PB electrodes display a higher contrast between the oxidized and reduced states than SiO₂-ATO/PB do. This is mainly due to two reasons. First, the higher PB loading of the ITO nanoparticle-based electrodes, confirmed by the charge densities in Table 5.1 above, makes these electrodes show a much deeper blue colour than SiO₂-ATO/PB-based electrodes, and so when PB is reduced into the colourless PW, the contrast to the pale yellow of the underlying nanoparticles is enhanced. The second reason seems to be a wetting issue of SiO₂-ATO/PB-based electrodes. Although both types of electrodes are highly hydrophobic due to the Viton binder, SiO₂-ATO/PB electrodes wet more slowly than ITO-based electrodes. This is likely due to differences in surface topology and roughness (Figure 5.7). Eventually, however, the electrolyte wets the entire surface, allowing the interaction between more PB particles and the solution, as observed by the gradual increase in absorbance at SiO₂-ATO/PB electrodes (Figure 5.11D).

A complete characterization of the electrochromic material was extracted from the spectroelectrochemical experiments, obtaining important parameters such as contrast ratio (C_R), colouration efficiency (η), and response time (τ).

Contrast ratio gives a quantitative measurement of the colour intensity of the electrochromic system:

$$C_R = \frac{R_0}{R_X} \quad (5.1)$$

where R_X is the intensity of the light reflected in the coloured state of the electrochrome, and R_0 the light reflected in the bleached state. C_R values smaller than 2 may not be well perceived by the naked eye.³⁰ As observed in Table 5.3, both materials display higher values of C_R .

Colouration efficiency gives an estimation of the performance of the electrochrome

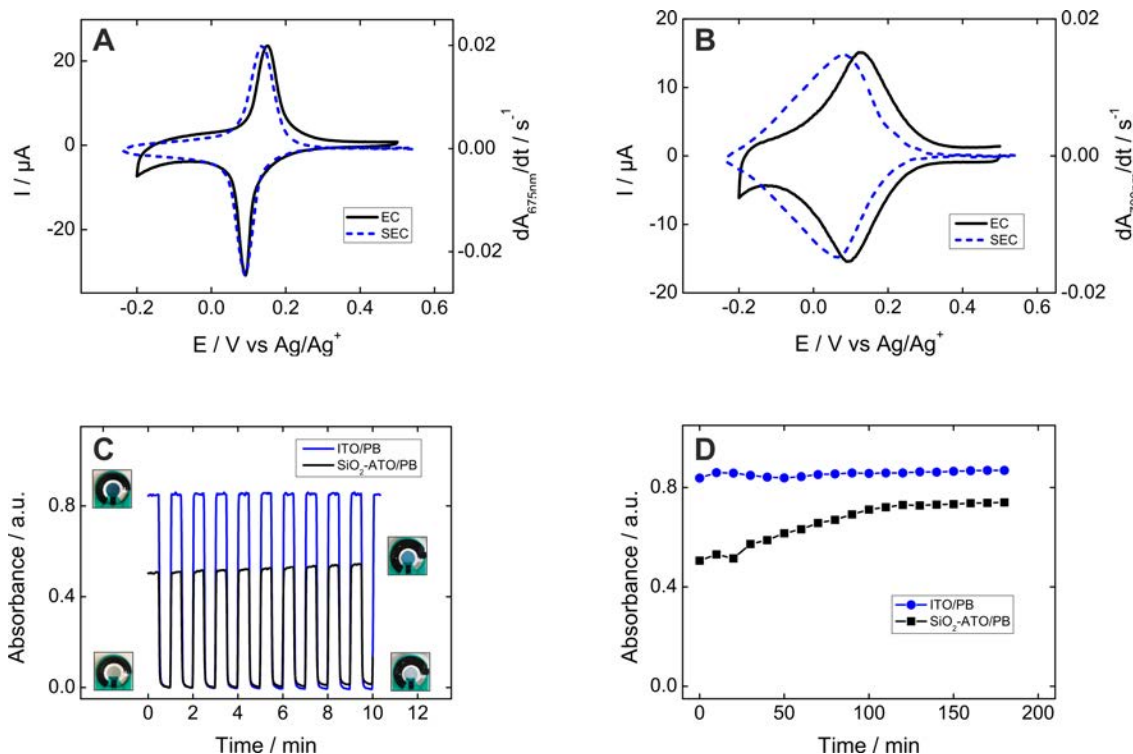


Figure 5.11: Cyclic voltammograms obtained in aqueous supporting electrolyte and derivative of the voltabsortogram for a $\text{SiO}_2\text{-ATO/PB}$ (A) and ITO/PB (B) electrode. Scan rate of 5 mV s^{-1} . (C) Plot of the absorbance when potential was stepped from -0.1 V to $+0.4 \text{ V}$ vs Ag/Ag^+ at intervals of 60 s in a 0.25 mM H_2O_2 solution in aqueous supporting electrolyte. (D) Representation of the contrast variation of the experiment in (C) for a longer time scale.

by relating the changes in absorbance with the amount of electric charge injected:

$$\eta = \frac{\Delta A}{Q} \quad (5.2)$$

where ΔA represents the variation in absorbance between coloured and bleached state, and Q is the charge required by the system to switch. The colouration efficiency is often referred to the maximum absorbance wavelength of each species, in this case $675 - 700 \text{ nm}$ (Table 5.3). The efficiency displayed by both materials is quite similar, as in both cases the electrochromic material is the same, and is comparable to other inorganic electrochromes reported in the literature with values in the range of 40 to 100 .³⁰

Last, the response time refers to the time required for the electrochromic display to switch from its coloured to its bleached state (or vice versa). The optimal response time depends on the actual application of the electrochromic device, ranging from a few milliseconds³¹ to several minutes.³² In the fabrication of electrochromic sensors it is desirable to observe fast response times, something that both Prussian Blue materials can achieve.

Despite the fact that ITO/PB electrodes seem to display a slightly better spectroelec-

trochemical performance than the analog SiO₂-ATO/PB electrodes, nanoparticle-based pastes present higher manufacturing costs as well as a more limited availability. For this, Prussian Blue pastes based on SiO₂-ATO were selected for the fabrication of the electrochromic devices in the next chapter.

| | SiO ₂ -ATO/PB | ITO |
|------------------------------------|--------------------------|-------------|
| C_R | 3.2 | 7.5 |
| $\eta / \text{cm}^2 \text{C}^{-1}$ | 58 (675 nm) | 63 (700 nm) |
| τ / s | <10 | <10 |

Table 5.3: Obtained parameters of the spectroelectrochemical performance for both electrochromic materials.

5.4 Conclusions

This chapter has presented the formulation of two electrochromic screen-printing pastes based on Prussian Blue. The PB pigments were prepared by chemically growing a thin PB layer on the surface of tin oxide-based conducting particles. Two different conducting materials were used: indium tin oxide (ITO) nanoparticles with a nominal size of 50 nm, and 3 μm SiO₂ particles covered by a thin (ca. 100 nm) antimony tin oxide (ATO) shell. PB-modified pigments have been combined with a Viton® binder system to yield high-quality screen-printing pastes. The high electrical resistance of the resulting layers required printing the material on a conventional electrode surface.

The presented material shows advantages compared to both electrodeposited PB, and screen-printed PB-modified graphite electrodes. Compared to electrodeposited PB, (i) it eliminates the “wet” nature of electrodeposition, (ii) the need to control critical electrodeposition parameters such as current and potential distribution over large area substrates, and (iii) it replaces an intrinsically “batch” process by a “continuous” large area process, screen-printing. On the other hand, compared to currently existing PB-modified graphite pastes, the material presented here enables the use of both, electrochemical and optical detection.

Although this work has focused on a classic electrochromic material such as Prussian Blue, other electrochromes may be used similarly, leading to additional uses and applications.

The outstanding spectroelectrochemical performance shown by both electrochromic materials in terms of electron transfer, colour contrast and switching stability, establishes the suitability of these materials to substitute the current electrodeposited Prussian Blue

display on a transparent electrode and progress toward a fully printed electrochromic sensor.

Bibliography

- [1] Diesbach, *Handbuch der Anorganischen Chemie* **1704**, 59, Teil B.
- [2] Neff, V. D. Electrochemical oxidation and reduction of thin films of Prussian Blue. *J. Electrochem. Soc.* **1978**, 125, 886–887.
- [3] Kong, B.; Selomulya, C.; Zheng, G.; Zhao, D. New faces of porous Prussian blue: interfacial assembly of integrated hetero-structures for sensing applications. *Chem. Soc. Rev.* **2015**, 44, 7997–8018.
- [4] Eftekhari, A.; Jian, Z.; Ji, X. Potassium secondary batteries. *ACS Appl Mater Interfaces* **2017**, 9, 4404–4419.
- [5] Karyakin, A. A.; Gitelmacher, O. V.; Karyakina, E. E. Prussian Blue-based first-generation biosensor. a sensitive amperometric electrode for glucose. *Anal. Chem.* **1995**, 67, 2419–2423.
- [6] Koncki, R.; Lenarczuk, T.; Radomska, A.; Głąb, S. Optical biosensors based on Prussian Blue films. *The Analyst* **2001**, 126, 1080–1085.
- [7] Lin, C.-L.; Ho, K.-C. A study on the deposition efficiency, porosity and redox behavior of Prussian blue thin films using an EQCM. *J. Electroanal. Chem.* **2002**, 524–525, 286–293.
- [8] Karyakin, A. A.; Karyakina, E. E. Prussian Blue-based ‘artificial peroxidase’ as a transducer for hydrogen peroxide detection. Application to biosensors. *Sens. Actuators B Chem.* **1999**, 57, 268–273.
- [9] Karyakin, A. A.; Gitelmacher, O. V.; Karyakina, E. E. A high-sensitive glucose amperometric biosensor based on Prussian Blue modified electrodes. *Anal. Lett.* **1994**, 27, 2861–2869.
- [10] Najafisayar, P.; Bahrololoom, M. E. Pulse electrodeposition of Prussian Blue thin films. *Thin Solid Films* **2013**, 542, 45–51.
- [11] Bonacin, J.; Santos, P. D.; Katic, V.; Foster, W.; Banks, C. Use of screen-printed electrodes modified by Prussian Blue and analogues in sensing of cysteine. *Electroanalysis* **2018**, 30, 170–179.
- [12] Sekretaryova, A. N.; Beni, V.; Eriksson, M.; Karyakin, A. A.; Turner, A. P. F.; Vagin, M. Y. Cholesterol self-powered biosensor. *Anal. Chem.* **2014**, 86, 9540–9547.

- [13] Cinti, S.; Cusenza, R.; Moscone, D.; Arduini, F. Paper-based synthesis of Prussian Blue nanoparticles for the development of whole blood glucose electrochemical biosensor. *Talanta* **2018**, *187*, 59–64.
- [14] Itaya, K.; Uchida, I.; Neff, V. D. Electrochemistry of polynuclear transition metal cyanides: Prussian blue and its analogues. *Acc. Chem. Res.* **1986**, *19*, 162–168.
- [15] Lundgren, C. A.; Murray, R. W. Observations on the composition of Prussian blue films and their electrochemistry. *Inorg. Chem.* **1988**, *27*, 933–939.
- [16] Karyakin, A. A.; Karyakina, E. E.; Gorton, L. The electrocatalytic activity of Prussian blue in hydrogen peroxide reduction studied using a wall-jet electrode with continuous flow. *J. Electroanal. Chem.* **1998**, *456*, 97–104.
- [17] Zakharchuk, N. F.; Meyer, B.; Henning, H.; Scholz, F.; Jaworksi, A.; Stojek, Z. A comparative study of Prussian-Blue-modified graphite paste electrodes and solid graphite electrodes with mechanically immobilized Prussian Blue. *J. Electroanal. Chem.* **1995**, *398*, 23–35.
- [18] Dungchai, W.; Chailapakul, O.; Henry, C. S. Electrochemical detection for paper-based microfluidics. *Anal. Chem.* **2009**, *81*, 5821–5826.
- [19] Yang, Y.-L.; Chuang, M.-C.; Lou, S.-L.; Wang, J. Thick-film textile-based amperometric sensors and biosensors. *Analyst* **2010**, *135*, 1230–1234.
- [20] Stojanovic, B. D.; Foschini, C. R.; Pavlovic, V. B.; Pavlovic, V. M.; Pejovic, V.; Varela, J. A. Barium titanate screen-printed thick films. *Ceram. Int.* **2002**, *28*, 293–298.
- [21] Krebs, F. C.; Fyenbo, J.; Jørgensen, M. Product integration of compact roll-to-roll processed polymer solar cell modules: methods and manufacture using flexographic printing, slot-die coating and rotary screen printing. *J. Mater. Chem.* **2010**, *20*, 8994–9001.
- [22] Coleman, J. P.; Lynch, A. T.; Madhukar, P.; Wagenknecht, J. H. Printed, flexible electrochromic displays using interdigitated electrodes. *Sol. Energy Mater. Sol. Cells* **1999**, *56*, 395–418.
- [23] DropSens, <https://dropsens.com>.
- [24] Coleman, J. P.; Lynch, A. T.; Madhukar, P.; Wagenknecht, J. H. Antimony-doped tin oxide powders: electrochromic materials for printed displays. *Sol. Energy Mater. Sol. Cells* **1999**, *56*, 375–394.

- [25] Schiller, R.; Battistig, G.; Rabani, J. Reversible electrochemical coloration of indium tin oxide (ITO) in aqueous solutions. *Radiat. Phys. Chem.* **2005**, *72*, 217–223.
- [26] Ricci, F.; Amine, A.; Palleschi, G.; Moscone, D. Prussian Blue based screen printed biosensors with improved characteristics of long-term lifetime and pH stability. *Biosens. Bioelectron.* **2003**, *18*, 165–174.
- [27] Li, N. B.; Park, J. H.; Park, K.; Kwon, S. J.; Shin, H.; Kwak, J. Characterization and electrocatalytic properties of Prussian blue electrochemically deposited on nano-Au/PAMAM dendrimer-modified gold electrode. *Biosens. Bioelectron.* **2008**, *23*, 1519–1526.
- [28] Laviron, E. The use of linear potential sweep voltammetry and of a.c. voltammetry for the study of the surface electrochemical reaction of strongly adsorbed systems and of redox modified electrodes. *J. Electroanal. Chem. Interfacial Electrochem.* **1979**, *100*, 263–270.
- [29] Karyakin, A. A. Prussian blue and its analogues: electrochemistry and analytical applications. *Electroanalysis* **2001**, *13*, 813–819.
- [30] Monk, P. M.; Mortimer, R. J.; Rosseinsky, D. R. *Electrochromism: fundamentals and applications*; VCH, Weinheim, 1995.
- [31] Sato, Y. Characterization of thermally oxidized iridium oxide films. *Vacuum* **1990**, *41*, 1198–1200.
- [32] Munro, B.; Krämer, S.; Zapp, P.; Krug, H.; Schmidt, H. All sol—gel electrochromic system for plate glass. *J. Non-Cryst. Solids* **1997**, *218*, 185–188.

6

A fully printed self-powered electrochromic biosensor

This chapter presents the complete transition towards a fabrication process entirely based on screen-printing for the production of self-powered biosensors akin to that presented in Chapter 3. In addition to the electrochromic Prussian Blue paste presented in the previous chapter, the development of a suitable electrolyte system was also required. In the present case, a gel polymer based on an ionic liquid and developed in collaboration with Prof. Gonzalo Guirado at the Department of Chemistry of the UAB, has been used.

6.1 Introduction

As discussed in previous chapters, the use of self-powered systems as analytical tools eliminates the need for an external power source to activate the sensing process. Self-powered systems such as those presented here also simplify considerably the fabrication processes, reducing the instrumentation needs to a minimum, facilitating portability, and potentially extending the scope of electroanalytical systems.^{1,2} However, a signaling device must always be coupled to the sensor in order to extract the analytical information.³ Since the introduction of the first self-powered sensor in 2001 by Katz and Willner,⁴ most of the efforts done in this field have focused on improving the typically low power output of these systems by optimizing the design of the electrochemical cell, the performance of the biosensor, or introducing new materials for their fabrication so the energy output could be high and sustainable in time to power the signaling system and any other possible external components.

As demonstrated in Chapter 3, an interesting alternative to the use of external detection systems is the combination of biofuel cells with electrochromic materials. The application of these materials is well known in the construction of electrochemical and photo-electrochemical self-powered devices,^{5,6} but their use in the fabrication of self-powered sensors is in a very early stage.

Most reported electrochromic sensors rely on the utilization of displays with a “sandwich” or “parallel-plate” configuration,⁷ where anode and cathode are placed face to face, thus minimizing the ohmic drop between electrodes, and allowing faster and homogeneous switches. As explained in Section 1.4.3, this simultaneous conversion at the display enables the detection of a certain analyte by the naked eye^{8–10} or, if coupled to a colour recording system, it also allows to relate the colouration/discolouration degree with the amount of analyte more accurately.^{11–13} When a “coplanar” or “interdigitated” construction is used instead, the internal resistance in the system can be exploited to generate a colour gradient in the display, leading to a instrumentation-less quantitative readout, as described in Chapters 3 and 4.

Other electrochromic sensors reported in the literature rely on the use of at least one transparent electrode.^{8,12,14} These are mostly tin oxides such as indium tin oxide (ITO)¹⁵ or fluorine tin oxide (FTO),¹⁶ but also the polymeric mixture of poly(3,4-ethylenedioxythiophene) and polystyrene sulfonate (PEDOT:PSS) is widely used.^{17,18} Moreover, thin layers of electrochromic materials are always deposited on them to ensure that, in the presence of an electrolyte with a high ionic conductivity, a fast and reversible colour switch is obtained. Both things can be a major issue when looking at a possible industrial impact of this technology in terms of costs and scalability of the fabrication processes.

In this chapter, the conventional transparent electrodes and the deposited thin layers of electrochromic material were replaced by a screen-printed layer of the electrochromic

material presented in the previous chapter, based on the use of conducting antimony tin oxide (ATO) particles coated with Prussian Blue.

A glucose biosensor was coupled to the electrochromic display in a coplanar arrangement, following a similar construction as that of Chapter 3, so the system can work as a galvanic cell providing an easy to interpret colorimetric readout. Moreover, a gel polymer electrolyte based on an ionic liquid was formulated and printed on top of the display, replacing the traditional aqueous supporting electrolytes used in most electroanalytical experiments, allowing to obtain a fully-printed solid-state analytical device.

6.2 Experimental

6.2.1 Reagents and materials

The electroanalytical devices presented here were designed using VectorWorks 2018, Student Edition (Techlimits, ES). 500 μm -thick polyethylene terephthalate (PET) sheets (Autostat WP20) from Mac Dermid (UK) were used as substrate for the printing of the electrochemical devices. Carbon (C2030519P4), and gold polymer (C2041206P2) conducting pastes were purchased from Gwent Electronic Materials LTD. (UK). Electrode silver (725A) and photocurable dielectric (PF-455B) pastes were obtained from Henkel (ES). White dielectric paste was kindly provided by Marabu (ES). SiO_2 -ATO-based electrochromic Prussian Blue paste was fabricated as described in the previous chapter.

Potassium trifluoromethanesulfonate (KTf) and poly(vinylidene fluoride-co-hexafluoropropylene) (PVDF-HFP) were obtained from Sigma-Aldrich. Ionic liquid 1-Ethyl-3-methylimidazolium trifluoromethanesulfonate (EMIM-Tf) was acquired from Solvionic (FR).

Glucose oxidase (GOx), EC 1.1.3.4, 236 U mg^{-1} , was purchased from Sekisui Diagnostics (UK). Poly(ethyleneglycol) diglycidyl ether (PEGDGE), and glucose were obtained from Sigma-Aldrich. The redox polymer $[\text{Os}(4,4'\text{-dimethyl-2,2'\text{-bipyridine}})_2(\text{poly-vinylimidazole})_{15}\text{Cl}]^+$ (Os-PVI₁₅) was synthesized using a previous reported protocol.^{19,20} A 0.1 M potassium chloride (KCl) from Sigma-Aldrich and 0.05 M phosphate buffer (PBS) from Fluka was used as the aqueous supporting electrolyte.

6.2.2 Instrumentation

A 30 W Epilog Mini 20 CO_2 Laser engraver from Laser Project (ES) was used to cut the PET substrates. Electrochemical measurements were done using a μ -Autolab III potentiostat (Metrohm) controlled by a GPES 4.1 software. Scanning electron microscopy images were obtained at an Auriga microscope (Carl Zeiss). An Alpha-Step 200 profilometer from Tencor Instruments was used to measure the thickness of the different

printed layers.

6.2.3 Electrode fabrication

Two types of electrochemical cells were used in this work, both screen-printed. The first cell consisted of a conventional 3-electrode design (Figure 6.1). The fabrication process of these electrodes was described in Section 5.2.4. When needed, the deposition of the electrochromic PB layer was omitted, leaving exposed the carbon surface of the working electrode.



Figure 6.1: Screen-printed electrodes used with (A) and without (B) a PB printed layer coating.

The second cell consisted of a Prussian Blue electrode with a rectangular shape (2x15 mm) placed between two carbon electrodes, 5 mm in diameter each (Figure 6.2). As in the device of Chapter 3, one carbon electrode is modified with a glucose biosensor, thus acting as the anode when connected to the PB display that acts as cathode. In this design, however, a second carbon electrode was printed opposite to the sensing electrode to easily regenerate the electrochromic display after each measurement. As seen in Figure 6.2, the fabrication process is similar to that of the previous electrodes. A gold screen-printing paste was used instead of the carbon paste to improve the colour contrast after PB bleaching. Last, a white colour dielectric paste was printed to define the electroactive areas of the cell. When required, a layer of gel polymer electrolyte was printed on top, covering the electrochromic display and slightly overlapping both carbon electrodes.

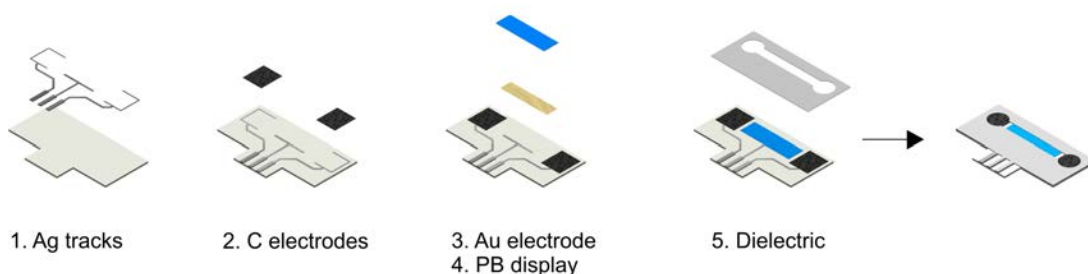


Figure 6.2: Fabrication steps of the electrochromic devices

6.2.4 Glucose biosensor construction

The surface of one carbon electrode was modified to build the glucose biosensor. A similar protocol to that reported by Heller *et al.* was followed.²¹ Briefly, 4 μL of a 10 mg mL^{-1} solution of the Os-PVI₁₅ prepared in a mixture of EtOH:H₂O (1:1) were mixed with 0.8 μL of a 10 mg mL^{-1} solution of GOx prepared in supporting electrolyte, and 1.2 μL of a 2.5 mg mL^{-1} aqueous solution of PEGDE. 5 μL were spread on the surface of the carbon electrode and allowed to dry at 4°C protected from light. After 1 hour, the electrodes were ready for use.

6.2.5 Gel polymer electrolyte

The composition of the gel electrolyte was optimized to obtain a consistent, homogeneous, and transparent flexible layer. For this, an optimal ratio between the ionic liquid, the gelling polymer, and the amount of solvent was obtained. 0.14 g of the gelling agent, PVDF, were dissolved in 0.5 mL acetone under vigorous stirring and mild heating. Note that, if the heating temperature exceeds 80-90 °C, PVDF may degrade, turning yellow. After 15-30 minutes, a transparent solution is obtained, indicating the complete dissolution of the polymer. Then, 50 mg of KTF and 340 μL of the IL were added to the mixture, and stirred while heating for another 15 minutes. After this, the gel polymer was ready for printing. The thickness of the printed layers of gel polymer were measured with a profilometer, obtaining values in the range between 10 and 20 μm .

6.3 Results and discussion

This section describes the results observed in the transition from the electrochromic device in Chapter 3, to a device where both display and electrolyte are printed. First, the performance of the printable electrochromic material as a horizontal coulometric metering bar is evaluated. Next, the use of a gel polymer electrolyte based on an ionic liquid substituting the conventional aqueous supporting electrolyte is assessed. Last, the Prussian Blue electrode is connected to a glucose biosensor to obtain a self-powered analytical device, and its performance using both electrolytes —aqueous and polymeric— is studied.

6.3.1 Printed coplanar display

The shift from an electrodeposited electrochromic material, which thickness is in the range of a few hundred nanometers, to a printed display where the thickness of the layer can be up to 20 μm , brings about changes to its electrochemical and optical properties. Figure 6.3 shows cyclic voltammograms recorded for two different Prussian Blue electrodes, one with a thin electrodeposited layer on a transparent ITO electrode similar to

those used in Chapter 3, and the other with a thick printed layer over a screen-printed gold electrode, as shown in Figure 6.2. As expected, the amount of deposited electrochromic material per unit area is much higher in the case of the printed display (2.7 mC cm^{-2} electrodeposited vs 8.9 mC cm^{-2} printed). This increase in the amount of PB results in a slower charge transfer, despite the semi-conducting nature of the ATO nanoparticles underneath the PB. Thus, peak-to-peak separation increases from 30 mV in the case of the electrodeposited layer to roughly 60 mV for the printed layer. The higher amount of

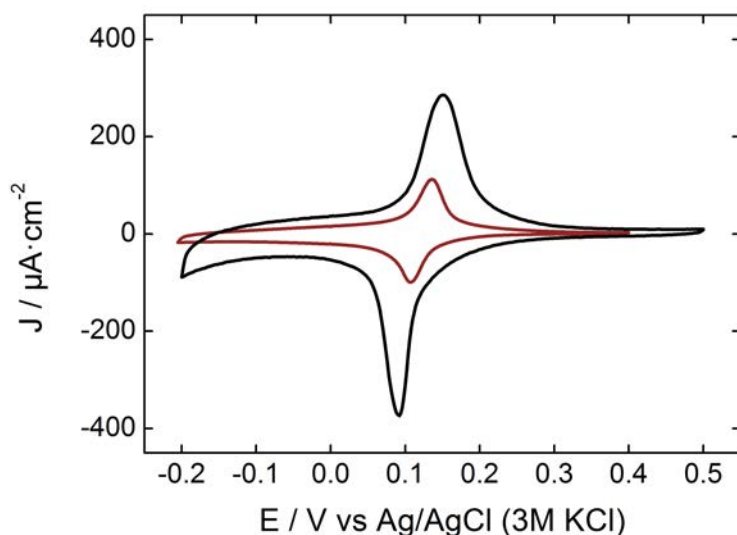


Figure 6.3: Cyclic voltammograms of electrodeposited (red line) and printed (black line) PB electrodes under aqueous supporting electrolyte. Scan rate of 5 mV s^{-1} .

electrochromic material as well as the more sluggish electron transfer alter the behaviour of the display when used as a visual coulometer in the form of a horizontal metering bar. For this, the nature and properties of the selected electrolyte must be readjusted in order to maintain a fast and clear colour conversion, as shown in Chapter 4. To study the behaviour of the PB display under different electrolyte conditions, a constant electric current of $40 \mu\text{A}$ was applied from the unmodified carbon electrode so the PB was progressively converted into PW. Two aqueous electrolytes with different conductivities were used. One, a 0.1 M KCl aqueous solution with a high conductivity similar to those used in common electroanalytical experiments, $\sigma_1 = 1.6 \text{ S m}^{-1}$, and the other, a 0.01 M KCl solution with a much lower conductivity, $\sigma_2 = 0.16 \text{ S m}^{-1}$. Also, the resistance of the medium was manually modified by depositing different volumes of solution, thus adjusting the thickness of the electrolyte of electrode surface so two different heights of electrolyte could be tested, $H_1 \approx 2 \text{ mm}$, and $H_2 \approx 0.1 \text{ mm}$. H_1 aimed at simulating the conditions of a system in which the current lines are distributed through the thick layer

of the ionic conductor, while H2 aimed at simulating a printed thin layer of electrolyte in which the current lines are restricted to a smaller volume. As seen in Figure 6.4, when an electrolyte with high conductivity is selected and a high volume is deposited on the surface of the electrode, the colour conversion at the display takes place at the same rate across the entire surface, and a full conversion from PB to PW is observed. If either the electrolyte conductivity or its thickness decreases, the internal resistance of the solution increases, and the electric current, which follows the path of least resistance, progressively depletes the electrochromic material at the display, generating a colour gradient. Last, when both electrolyte conductivity and thickness decrease, the internal resistance increases even more, resulting in two effects. First, the colour front is better defined due to the abrupt iR drop at the switching region and, second, the conversion rate of the PB is considerably slower. It is important to note that, under these stringent conditions, the electrochromic display can be irreversibly damaged by the degradation of either the ATO core of the particles or the electrochromic coating.

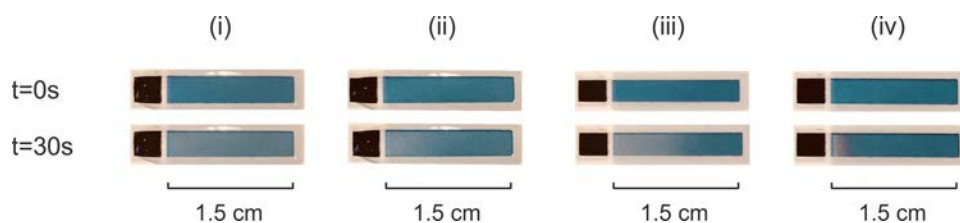


Figure 6.4: Captures of the display at two different times under a constant applied current of $40 \mu\text{A}$ for different aqueous electrolyte conductivities and thicknesses: (i) $\sigma_1 = 1.6 \text{ S m}^{-1}$, 2 mm; (ii) $\sigma_1 = 0.16 \text{ S m}^{-1}$, 2 mm; (iii) $\sigma_1 = 1.6 \text{ S m}^{-1}$, 0.1 mm; (iv) $\sigma_1 = 0.16 \text{ S m}^{-1}$, 0.1 mm.

The galvanostatic experiments of Figure 6.4 show that an electrolyte with intermediate properties between the two limit cases ('i' and 'iv') may lead to an optimum performance of the display, i.e. fast and clear colour conversions. When considering possible electrolytes that fulfill this, two important things must be taken into account. On the one hand, it is necessary to control the deposition of the electrolyte on the device since, as shown above, the thickness of the layer plays a key role on its performance, leading to considerable variations in rate and clearness of colour conversions. On the other hand, it is desirable that the final device is able to measure any kind of sample, regardless of its colour or the presence of substances that may interfere with the electrochromic display, i.e. sample and display should be physically separated. For this, ionic liquid-based gel polymer electrolytes may represent an interesting alternative to conventional aqueous electrolytes as they are capable of displaying relatively high ionic conductivities,²² and, at the same time, they can be screen-printed as any other paste, which allows to control the thickness of the material used. Moreover, given the organic nature of most common gel polymer electrolytes, a separation barrier between sample and display is formed, allowing the exchange of ions between the two phases without being mixed.

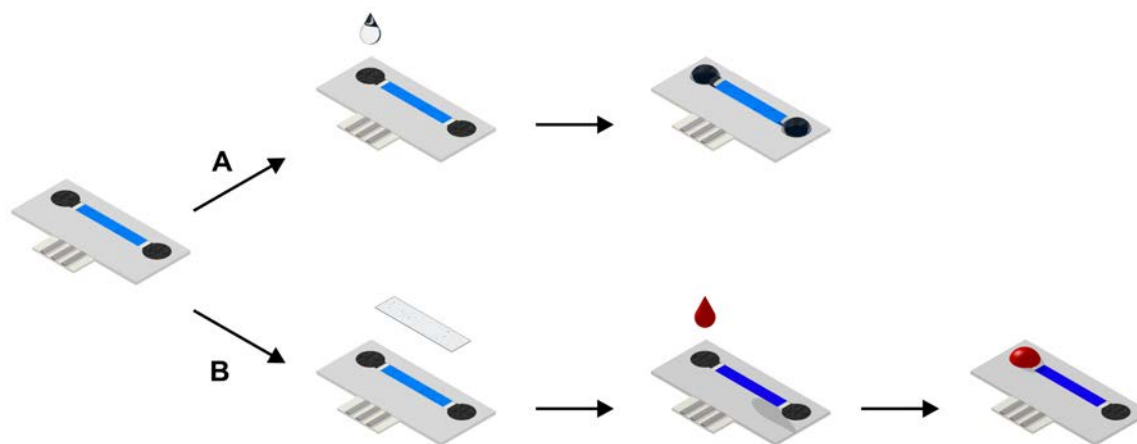


Figure 6.5: Schematic representation of the two approaches that can be used for measuring with the electrochromic devices. (A) An aqueous sample, that serves also as supporting electrolyte, is placed on top, covering the exposed areas of the three electrodes. (B) After printing the gel polymer electrolyte, a drop of the sample is placed only on top of the sensing electrode, with no physical contact between sample and display.

6.3.2 Gel polymer electrolyte characterization

Solid-state electrolytes display certain advantages over conventional liquid electrolytes that make them a suitable option for printed electrochromic devices. These advantages include the outstanding mechanical stability, a simple fabrication and assembly of the devices, or the protection against possible leakages of toxic chemical components present in them.²² Among the different types of solid-state electrolytes, gel polymer electrolytes stand out above the others because of their relatively high conductivities,^{23,24} Particularly, ionic liquid-based gel polymer electrolytes display high ionic conductivities, besides other features such as nonvolatility and wide potential windows.^{25,26} A suitable gel polymer electrolyte for electrochromic displays must show high ionic conductivity and high mechanical stability, in addition to a high degree of transmissivity. Moreover, the formulated electrolyte must possess rheologic properties adequate for the printing process at hand.

The formulated gel polymer consisted of a mixture of three components: an ionic liquid, EMIM-Tf, that served as ionic charge carrier, potassium triflate, as the source of potassium required by the Prussian Blue in order to keep its reversibility,²⁷ and a fluoropolymer, PVDF, that was used as a gelling agent to provide consistency to the electrolyte in the form of a flexible and transparent gel where the other components of the mixture are embedded.

The physicochemical properties of the polymer electrolyte were studied. First, its ionic conductivity was estimated by electrochemical impedance spectroscopy (EIS) at room

temperature using $10 \times 10 \mu\text{m}$ interdigitated electrodes (IDEs).²⁸ For this, $10 \mu\text{L}$ of the polymer electrolyte were cast on the surface of the IDEs and let to dry, and the AC impedance response was registered. For the mathematical simulation of the impedimetric response, an equivalent circuit consisting of a constant phase element (CPE) representing the electrode/electrolyte interface in series with a resistance (R_s) representing electrolyte resistance was considered. As seen in Figure 6.6A, experimental and simulated data show

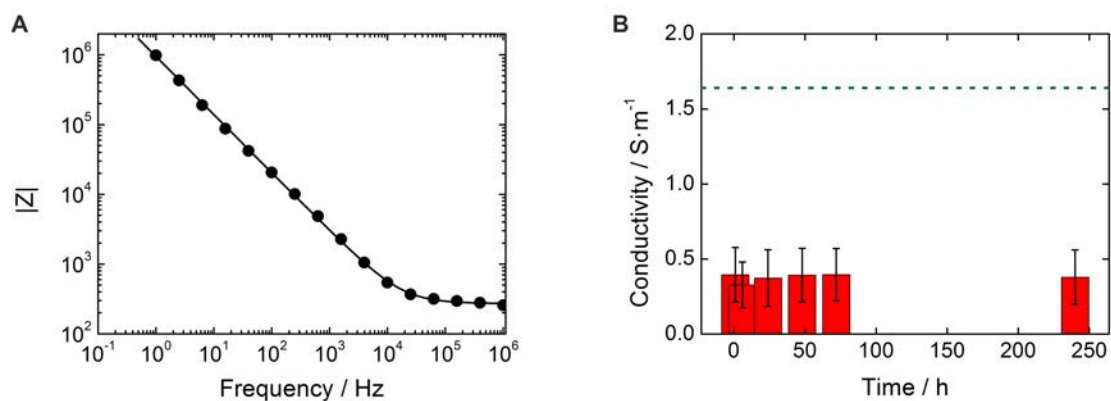


Figure 6.6: (A) General Bode plot for the gel polymer electrolyte. Black circles represent the experimental data, and black line the fitted data obtain from the equivalent circuit. (B) Plot of the gel polymer electrolyte conductivity measured through a time period of 10 days. Error bars represent the standard deviation for $n=3$ electrodes. Dotted green line represents the conductivity of most common aqueous supporting electrolytes used in bioanalysis.

an excellent fit, validating the implemented equivalent circuit. The magnitude of the electrolyte resistance was obtained from the Bode plot²⁹ of Figure 6.6A at high frequencies, where the main contribution to the registered impedance values are due to the electrolyte resistance. The obtained values for the resistance were interpolated with those obtained with the same IDE in each case in aqueous KCl solutions of different conductivities, and an electrolyte conductivity of $0.4 \pm 0.1 \text{ S m}^{-1}$ was calculated.

The chemical composition of the gel polymer electrolyte not only provides a high ionic conductivity, but also, due to the low vapor pressure of ionic liquids, this conductivity presents a remarkable stability in time as seen in Figure 6.6B, something that must be taken into account when fabricating solid state electrochromic devices.³⁰

It is important that the selected electrolyte shows a wide electrochemical window, that is, the different components of the electrolyte do not undergo any electrochemical process for a wide range of potentials. This is the case for the present ionic liquid gel polymer electrolyte. Figure 6.7A shows cyclic voltammograms for the gel polymer electrolyte and for the aqueous supporting electrolyte using the carbon electrodes of Figure 6.1B. As seen, both electrolytes display a wide potential window of roughly 3 V, and none of them show any redox activity in the range of 0 to 0.5 V vs Ag/Ag^+ , where the PB/PW system

reacts.

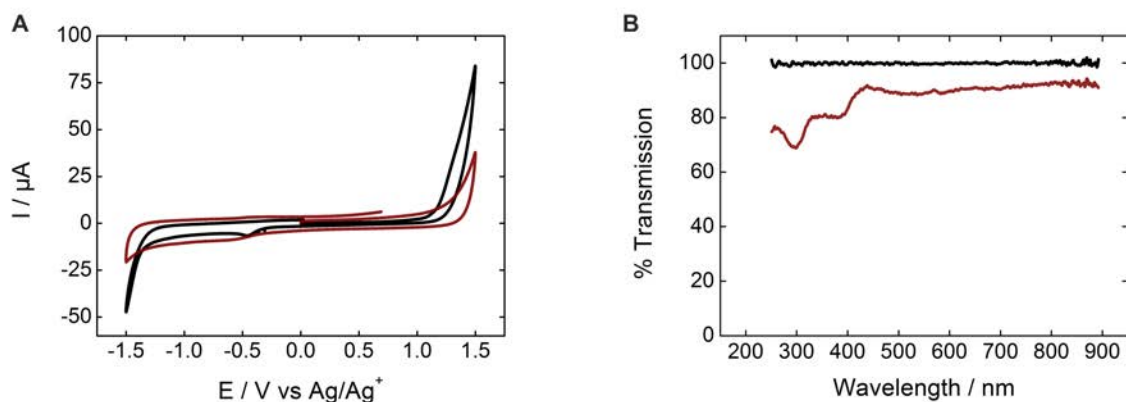


Figure 6.7: (A) Cyclic voltammograms obtained in a carbon SPE with a gel polymer electrolyte (red line) and an aqueous supporting electrolyte (black line). Scan rate of 10 mV s^{-1} . (B) UV-vis reflectance spectrum of a printed layer of gel polymer electrolyte (red line) compared to the background with no sample (black line).

As explained above, a very important characteristic that a suitable electrolyte must have for its use in electrochromic devices/sensors is a high optical transmissivity. The use of an ionic liquid in the formulation of the polymer electrolyte not only provides the required ionic conductivity, but it also confers the resulting gel the optical transparency sought in this case. Figure 6.7B shows the wavelength spectrum obtained on a PET substrate in a UV-vis reflectance mode for a printed layer of the gel polymer of roughly $10 \mu\text{m}$. As observed, no significant amount of light is absorbed in the visible region, obtaining transmission values higher than 90 %.

Last, the electrochemical performance of the Prussian Blue paste was evaluated under the use of the gel polymer electrolyte. For this, cyclic voltammograms were recorded with the PB-SPEs of Figure 6.1A using the aqueous and gel polymer electrolytes. As seen in Figure 6.8, a shift in the position of the voltammograms appears due to the different anions present in each electrolyte, modifying the behaviour of the pseudo-reference Ag/Ag^+ electrode. Also, peak currents decrease when using the polymer electrolyte since the diffusion coefficient of potassium is affected by the composition of the solution, as predicted by the Randles-Ševčík equation.²⁹ Regardless of this, the electrochemical performance of the electrochromic material with a polymer electrolyte was still remarkable.

6.3.3 Fully printed self-powered sensor

Once the suitability of the gel polymer electrolyte was assessed, the fully-printed electrochromic device was assembled and tested in the determination of glucose. First the amperometric response of the glucose biosensor was evaluated. Next, the electrochromic

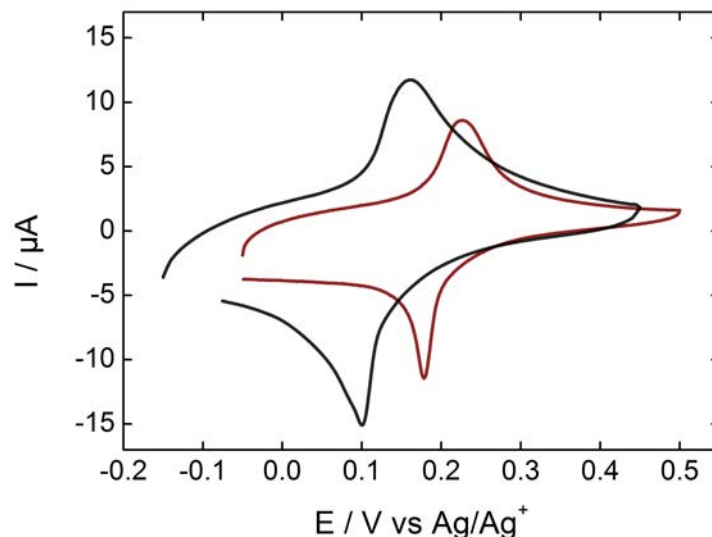


Figure 6.8: Cyclic voltammograms obtained in a PB-SPE with a gel polymer electrolyte (red line) and an aqueous supporting electrolyte (black line). Scan rate of 5 mV s^{-1} .

display was connected to the biosensor, and the electrochemical performance of the self-powered system was studied. Last, the electrochromic sensor was used for the determination of glucose in buffered standard solutions and in human blood. In all cases, the behaviour of the system with a printed electrolyte was compared to that of the system with an aqueous electrolyte.

Amperometric glucose biosensor

The glucose biosensor used in Chapter 3 was modified in order to achieve a system with a much higher degree of stability but maintaining a similar performance in terms of dynamic range, current densities and working potential. The redox mediator TMPD was replaced by an osmium-based redox polymer. In this polymer, a low redox potential osmium complex is chemically attached to the chains of a water insoluble organic polymer, PVI, which prevents its leakage to the solution. Moreover, the glucose oxidase enzyme was “wired” to the redox polymer using a cross-linker, thus increasing its stability and preventing also its leakage.^{21,31}

The performance of this biosensor was evaluated by chronoamperometry using the carbon SPEs of Figure 6.1B. The working electrode was poised at a fix potential of 0.3 V vs Ag/Ag^+ that ensured a complete oxidation of the osmium centers in the redox polymer as observed in Figure 6.9A. The electric current registered was measured for 120 seconds and plotted against the glucose concentration of different standard solutions prepared in supporting electrolyte as seen in the Michaelis-Menten plot in Figure 6.9B. As

observed, the biosensor displays high current densities, and a linear behaviour is obtained in the range from 1 to 10 mM of glucose. For higher concentrations, the biosensor slowly saturates, and a slight deviation from the linear behaviour appears.

Last, the stability of the biosensor was evaluated. For this, the amperometric response of the biosensor in a 10 mM glucose solution was registered. Measurements were carried out for a time period of 9 days in separate intervals. Each electrode used in the calibration curves of Figure 6.9B was rinsed with deionized water, dried, and kept at 4°C in darkness before each measurement (Figure 6.9C). During the first 24 hours after the electrode modification, the activity of the biosensor remained essentially unaltered. A decrease in its activity was observed, in line with previous works reporting on the use of a similar biosensor composition.²¹ After 48 hours the biosensor tends to stabilize at roughly 60% of its initial activity.

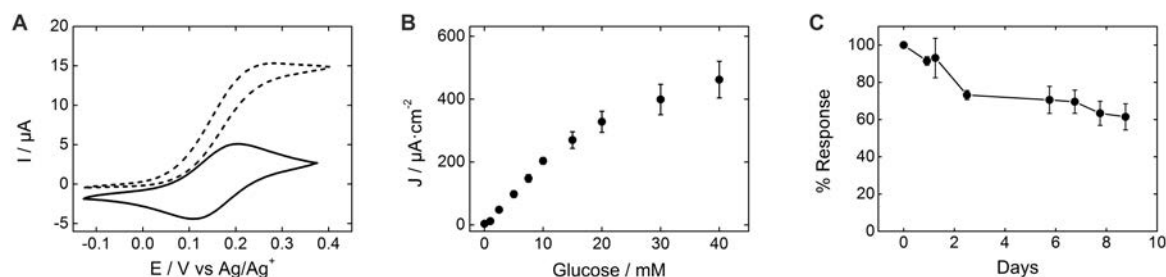


Figure 6.9: (A) Cyclic voltammograms of the osmium redox polymer in the absence (black line) and in the presence (dotted line) of 10 mM glucose. Scan rate of 5 mV s^{-1} (B) Amperometric calibration curve of the biosensor for different glucose concentrations. (C) Plot of the stability of the biosensor for a 10 mM glucose solution for a time period of 9 days. Error bars represent the standard deviation of $n=4$ electrodes.

Self-powered system

The feasibility of an electrochemical system to work as a galvanic cell can be estimated by looking at the cyclic voltammograms of the electroactive species involved. Figure 6.10 shows cyclic voltammograms recorded for the osmium redox polymer at the anode and for the Prussian Blue at the cathode. The onset potential of the PB reduction at the cathode is observed at 0.3 V vs Ag/Ag^+ , while the oxidation of the osmium redox polymer is observed at 0.1 V vs Ag/Ag^+ , which leads to cell voltages of roughly 0.2 V . Note that the cell voltage obtained for the present species tends to be rather low compared to current state of the art enzymatic fuel cells.³² This limits the device performance, particularly in systems with relatively high internal resistance. However, the fuel cell presented in this chapter represents a limit case where the formal potentials of the electroactive species are very close. The substitution of either the redox mediator or the electrochromic species, or even both, for others with lower and higher formal potentials respectively, would lead to higher cell voltages, and thus to an improvement in the overall system performance.

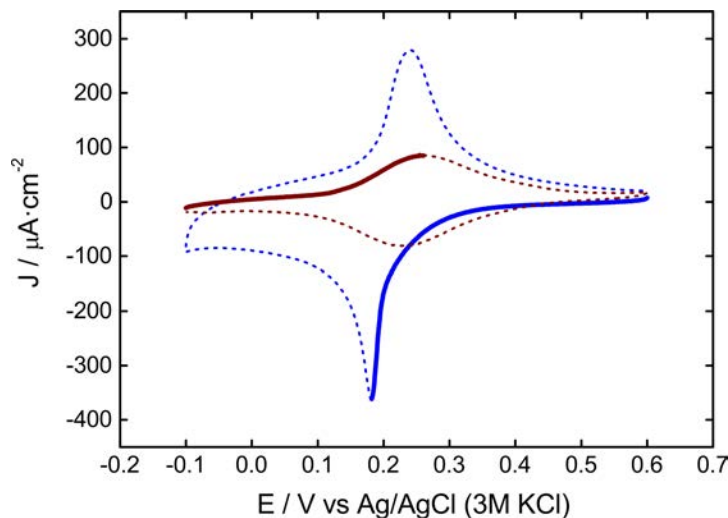


Figure 6.10: Cyclic voltammograms of the electroactive species at the anode, Os-PVI₁₅ (red line), and at the cathode, PB (blue line). Scan rate of 5 mV s⁻¹.

The behaviour of the self-powered system was studied with both electrolytes using glucose solutions of different concentrations. The Prussian Blue cathode was connected to the sensing anode, thus initiating the enzymatic reaction. Figure 6.11 shows the polarization and power curves corresponding to the systems with an aqueous electrolyte ('A' and 'B') and with a gel polymer electrolyte ('C' and 'D'). The first thing to notice is that, in contrast to the self-powered system shown in Chapter 3, the electrochromic cathode does not limit the enzymatic reaction at the anode, as the amount of charge available in the printed display is much higher than that in the electrodeposited one. Also, a progressive increase in the current and power output is observed as the amount of analyte is increased, reaching maximum values at 10 — 15 mM, in agreement with the Michaelis-Menten plot in Figure 6.9B. The lower internal resistance in the aqueous system is observed when the maximum current output of both systems is compared. While the cell with an aqueous electrolyte reaches a maximum current density of roughly 60 $\mu\text{A cm}^{-2}$ at 20 mM of glucose, the system with the gel polymer electrolyte is only capable of achieving 35 $\mu\text{A cm}^{-2}$, almost half of that generated by the aqueous electrolyte.

Last, anode and cathode were connected, and the progressive conversion of the Prussian Blue in the display into its reduced form by action of the enzymatic activity was registered. The transition from an electrodeposited to a printed display with a higher amount of electrochromic material, as well as the change in the redox mediator to one with a higher formal potential (TMPD vs Os-PVI₁₅), makes it necessary to extend the measuring time from the 30 seconds of experiments in Chapter 3 to 90 seconds, to see similar degrees of conversion in the display. In addition, the shift from an aqueous to a gel polymer electrolyte with higher internal resistance, further increases the measuring time up to 5 minutes, since the conversion rate of the display is markedly slower.

It was observed that the concentration of PVDF and ionic liquid in the paste, and thus the thickness of the printed layer, was a critical parameter to the performance of the device. For this, the amount of solvent, acetone, was reduced to a minimum, compared to other gel polymer electrolytes with similar chemical compositions,³³ which allowed to print thicker layers of material, leading to a substantial decrease in the measuring time from 20 to 5 minutes. This indicates that an improved formulation of the polymer electrolyte, or optimized printing parameters such as the snap-off distance or the screen mesh density³⁴ could lead to an improved performance of the device, reducing the measuring time even further. Also, as mentioned above, the substitution of the electroactive species at both electrodes by others that generate higher cell voltages would lead to similar results.

Figure 6.12 shows images taken 90 seconds and 5 minutes after the connection of the electrodes for the aqueous and gel polymer electrolyte, respectively. The points in the calibration curves (Figures 6.12) represent the position of the colour front estimated from the images captured. A clear correlation between the distance converted and the concentration of glucose is observed in both systems. As mentioned above, one important advantage of using a printed gel polymer electrolyte instead of the conventional aqueous

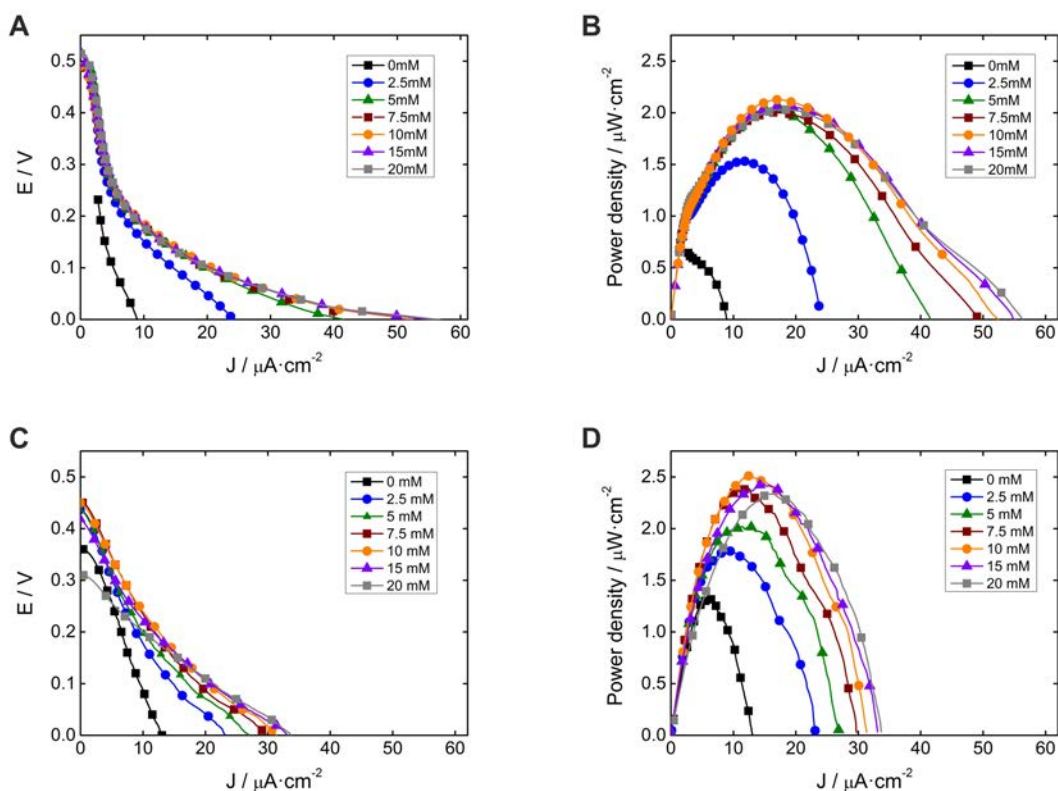


Figure 6.11: Polarization and corresponding power curves obtained for the self-powered device for different glucose concentrations using an aqueous supporting (A and B) or gel polymer (C and D) electrolyte. Scan rate of 1 mV s^{-1} .

supporting electrolyte is the possibility of separating the sample from the electrochromic display, which allows to measure coloured samples that otherwise would mask the conversion of Prussian Blue into Prussian White, as well as to prevent the action of electroactive interferences on the display. To test this, human blood samples were collected from a volunteer's thumb using safety lancets. Between 10 and 20 μL were extracted and placed on top of the biosensing anode, and the system was connected. As shown in Figure 6.12, the electrochromic display reaches a distance conversion slightly higher than that of the 2.5 mM glucose standard, in agreement with the measured concentration of 2.8 mM obtained using a commercial glucose meter (CardioCheck, Novalab, ES).

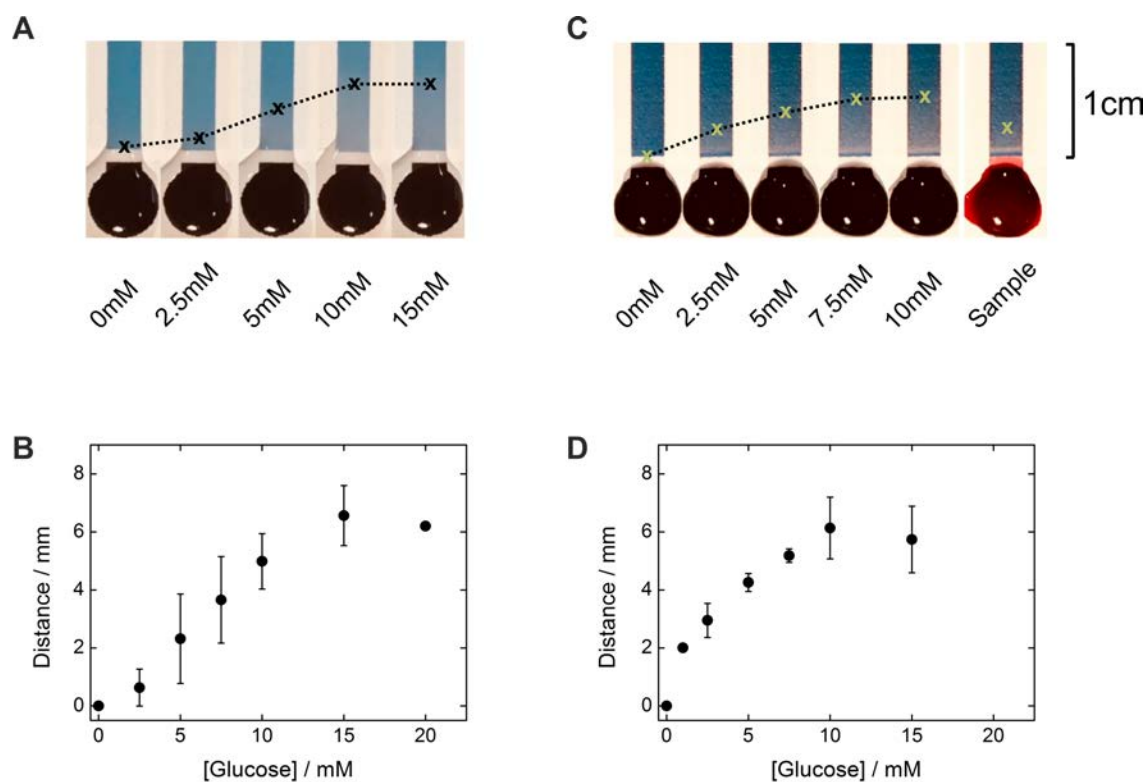


Figure 6.12: Image captures of the evolution of the electrochromic display after 90 s (A), and after 5 min (C) of connection of the system for different glucose concentrations prepared in supporting electrolyte, and for a human blood sample. (C) Calibration plot of the distance converted of the display obtained from 'A'. (D) Calibration plot of the distance converted from 'C'. Error bars represent the standard deviation for $n=3$ devices.

It is interesting to note that, while the device with the gel polymer electrolyte requires roughly 5 minutes to obtain a similar degree of colour conversion compared to the device with the aqueous electrolyte, the possibility of having a better control on the thickness of the electrolyte that covers the electrodes, and thus the internal resistance of the cell, leads to a significant improvement in the repeatability of the measurements with different devices, as inferred from the size of the error bars, which are shorter.

Moreover, the colour conversion of the electrochromic display under the two electrolytes was compared when the system was connected using a 10 mM glucose solution. Figure 6.13 shows the percentage of the red values extracted from the RGB plots of both cases (see Annex 2). As observed, the plot of the colour switch in the case of the gel polymer electrolyte displays a steeper slope than that of the aqueous electrolyte. The thin printed layer of gel polymer, and its lower ionic conductivity lead to a higher internal resistance, which translates into a better defined switch, as explained in Chapter 4.

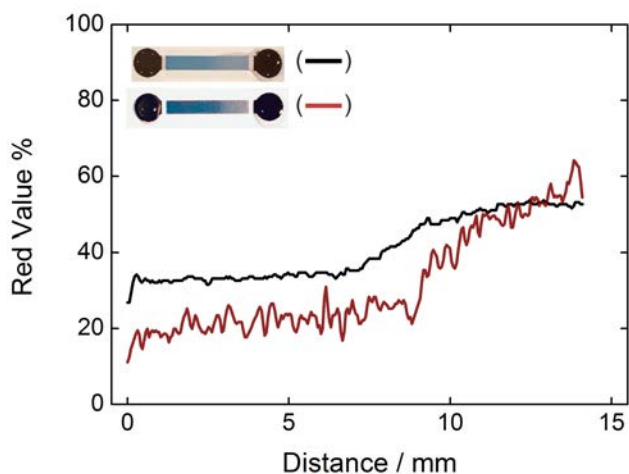


Figure 6.13: Colour profiles of the PB display obtained with ImageJ software for the self-powered experiment with a 15 mM glucose solution under the use of the two electrolytes: aqueous (black line), and gel polymer (red line).

6.4 Conclusions

This chapter has shown the evolution from an electrochromic sensor that relied on the use of an electrodeposited display on a transparent electrode to a device where the electrochromic display is printed using an ATO-based Prussian Blue paste. The behaviour of the printed device was evaluated under the use of a conventional aqueous electrolyte and under the use of a printed ionic liquid-base gel polymer electrolyte.

The use of a printable gel polymer as electrolyte allows the separation of the sample from the display, avoiding the effects of possible interfering substances. Moreover, since the sample does not contact the display, it is possible to measure coloured samples that would otherwise mask the colour changes at the PB cathode. The thin printed layer of electrolyte results in a high internal resistance, which increases the measuring time. However, a more clear colour switch is achieved, facilitating the readout of the display.

The fabrication of a solid state electrochromic sensor entirely by screen-printing can

lead to extremely cost effective devices including skin patches, contact lenses, and other non-invasive and easy to use wearables.³⁵⁻³⁷

Bibliography

- [1] Gonzalez-Solino, C.; Lorenzo, M. Enzymatic fuel cells: towards self-powered implantable and wearable diagnostics. *Biosensors* **2018**, *8*, 11–29.
- [2] Arechederra, R. L.; Minteer, S. D. Self-powered sensors. *Anal. Bioanal. Chem.* **2011**, *400*, 1605–1611.
- [3] Grattieri, M.; Minteer, S. D. Self-powered biosensors. *ACS Sens.* **2018**, *3*, 44–53.
- [4] Katz, E.; Bückmann, A. F.; Willner, I. Self-powered enzyme-based biosensors. *J. Am. Chem. Soc.* **2001**, *123*, 10752–10753.
- [5] Svensson, J. S. E. M.; Granqvist, C. G. Electrochromic coatings for “smart windows”. *Sol. Energy Mater.* **1985**, *12*, 391–402.
- [6] Rosseinsky, D. R.; Mortimer, R. J. Electrochromic systems and the prospects for devices. *Adv. Mater.* **2001**, *13*, 783–793.
- [7] Mortimer, R. J.; Rosseinsky, D. R.; Monk, P. M. *Electrochromic materials and devices*; Wiley-VCH, Weinheim, 2015.
- [8] Liu, H.; Crooks, R. M. Paper-based electrochemical sensing platform with integral battery and electrochromic read-out. *Anal. chem.* **2012**, *84*, 2528–2532.
- [9] Peimanifard, Z.; Rashid-Nadimi, S. Light-powered cell for detection of glucose with the naked eye. *Electrochem. Comm.* **2017**, *79*, 37–40.
- [10] Zhang, X.; Jing, Y.; Zhai, Q.; Yu, Y.; Xing, H.; Li, J.; Wang, E. Point-of-care diagnoses: flexible patterning technique for self-powered wearable sensors. *Anal. Chem.* **2018**, *90*, 11780–11784.
- [11] Zloczewska, A.; Celebanska, A.; Szot, K.; Tomaszewska, D.; Opallo, M.; Jönsson-Niedziolka, M. Self-powered biosensor for ascorbic acid with a Prussian blue electrochromic display. *Biosens. Bioelectron.* **2014**, *54*, 455–461.
- [12] Zhang, X.; Zhang, L.; Zhai, Q.; Gu, W.; Li, J.; Wang, E. Self-powered bipolar electrochromic electrode arrays for direct displaying applications. *Anal. Chem.* **2016**, *88*, 2543–2547.
- [13] Xu, W.; Fu, K.; Bohn, P. W. Electrochromic sensor for multiplex detection of metabolites enabled by closed bipolar electrode coupling. *ACS Sensors* **2017**, *2*, 1020–1026.

- [14] Xu, W.; Fu, K.; Ma, C.; Bohn, P. W. Closed bipolar electrode-enabled dual-cell electrochromic detectors for chemical sensing. *Analyst* **2016**, *141*, 6018–6024.
- [15] Hecht, D. S.; Hu, L.; Irvin, G. Emerging transparent electrodes based on thin films of carbon nanotubes, graphene, and metallic nanostructures. *Adv. Mater.* **2011**, *23*, 1482–1513.
- [16] Kim, H.; Auyeung, R. C. Y.; Piqué, A. Transparent conducting F-doped SnO₂ thin films grown by pulsed laser deposition. *Thin Solid Films* **2008**, *516*, 5052–5056.
- [17] Crispin, X.; Jakobsson, F. L. E.; Crispin, A.; Grim, P. C. M.; Andersson, P.; Volodin, A.; van Haesendonck, C.; der Auweraer, M. V.; Salaneck, W. R.; Berggren, M. The origin of the high conductivity of poly(3,4-ethylenedioxythiophene)-poly(styrenesulfonate) (PEDOT-PSS) plastic electrodes. *Chem. Mater.* **2006**, *18*, 4354–4360.
- [18] Singh, R.; Tharion, J.; Murugan, S.; Kumar, A. ITO-free solution-processed flexible electrochromic devices based on PEDOT: PSS as transparent conducting electrode. *ACS Appl. Mater. Interfaces* **2016**, *9*, 19427–19435.
- [19] Buckingham, D. A.; Dwyer, F. P.; Goodwin, H. A.; Sargeson, A. M. Mono- and Bis-(2,2'-bipyridine) and (1,10-phenanthroline) chelates of ruthenium and osmium. IV. Bis chelates of bivalent and trivalent osmium. *Aust. J. Chem.* **1964**, *17*, 325–336.
- [20] Forster, R. J.; Vos, J. G. Synthesis, characterization, and properties of a series of osmium- and ruthenium-containing metallopolymers. *Macromolecules* **1990**, *23*, 4372–4377.
- [21] Ohara, T. J.; Rajagopalan, R.; Heller, A. "wired" enzyme electrodes for amperometric determination of glucose or lactate in the presence of interfering substances. *Anal. Chem.* **1994**, *66*, 2451–2457.
- [22] Dubal, D. P.; Chodankar, N. R.; Kim, D.-H.; Gomez-Romero, P. Towards flexible solid-state supercapacitors for smart and wearable electronics. *Chem. Soc. Rev.* **2018**, *47*, 2065–2129.
- [23] Song, J.; Wang, Y.; Wan, C. C. Review of gel-type polymer electrolytes for lithium-ion batteries. *J. Power Sources* **1999**, *77*, 183–197.
- [24] Stephan, A. M. Review on gel polymer electrolytes for lithium batteries. *Eur. Polym. J.* **2006**, *42*, 21–42.
- [25] Hallinan, D. T.; Balsara, N. P. Polymer electrolytes. *Annu. Rev. Mater. Res.* **2013**, *43*, 503–525.

- [26] Alesanco, Y.; Viñuales, A.; Rodriguez, J.; Tena-Zaera, R. All-in-One gel-based electrochromic devices: strengths and recent developments. *Materials (Basel)* **2018**, *10*, 414–431.
- [27] Itaya, K.; Uchida, I.; Neff, V. D. Electrochemistry of polynuclear transition metal cyanides: Prussian blue and its analogues. *Acc. Chem. Res.* **1986**, *19*, 162–168.
- [28] Laczka, O.; Baldrich, E.; Munoz, F. X.; del Campo, F. J. Detection of Escherichia coli and salmonella typhimurium using interdigitated microelectrode capacitive immunosensors: the importance of transducer geometry. *Anal. Chem.* **2008**, *80*, 7239–7247.
- [29] Scholz, F. *Electroanalytical methods*; Springer, Berlin, 2010.
- [30] Desai, S.; Shepherd, R. L.; Innis, P. C.; Murphy, P.; Hall, C.; Fabretto, R.; Wallace, G. G. Gel electrolytes with ionic liquid plasticiser for electrochromic devices. *Electrochim. Acta* **2011**, *56*, 4408–4413.
- [31] Ohara, T. J.; Rajagopalan, R.; Heller, A. Glucose electrodes based on cross-linked bis(2,2'-bipyridine)chloroosmium(+2) complexed poly(1-vinylimidazole) films. *Anal. Chem.* **1993**, *65*, 3512–3517.
- [32] Mazurenko, I.; de Poulpiquet, A.; Lojou, E. Recent developments in high surface area bioelectrodes for enzymatic fuel cells. *Curr. Opin. Electrochem.* **2017**, *5*, 74–84.
- [33] Kumar, D.; Hashmi, S. A. Ionic liquid based sodium ion conducting gel polymer electrolytes. *Solid State Ion.* **2010**, *181*, 416–423.
- [34] Banks, C. E.; Foster, C. W.; Kadara, R. O. *Screen-printing electrochemical architectures*; Springer, New York, 2016.
- [35] Yao, H.; Shum, A. J.; Cowan, M.; Lähdesmäki, I.; Parviz, B. A. A contact lens with embedded sensor for monitoring tear glucose level. *Biosens. Bioelectron.* **2011**, *26*, 3290–3296.
- [36] Windmiller, J.; Wang, J. Wearable electrochemical sensors and biosensors: a review. *Electroanalysis* **2013**, *25*, 29–46.
- [37] Bandodkar, A. J.; Jia, W.; Yardımcı, C.; Wang, X.; Ramirez, J.; Wang, J. Tattoo-based noninvasive glucose monitoring: a proof-of-concept study. *Anal. Chem.* **2015**, *87*, 394–398.

7

Conclusions and outlook

This final chapter summarizes the principal conclusions of this dissertation. In addition, possible future directions are discussed, including device modifications that can lead to performance improvements.

7.1 Conclusions

The work presented in this thesis describes the development of self-powered glucose biosensors that use an electrochromic material as power source and as information display. The application of “coplanar” electrochromic displays in sensing has been described, studied, and characterized in detail, and a fully printed electrochromic sensing device has been presented. The specific results of this thesis are summarized as follows:

- **A self-powered electrochromic glucose biosensor was developed.** The combination of an electrochromic Prussian Blue display with a glucose biosensor allows to have a self-powered analytical device. The modification of the conventional “sandwich” configuration of most electrochromic devices for a “coplanar” architecture provides a quantitative readout of the analyte concentration at the display in the form of a metering bar.
- **Numerical simulations were used to understand the underlying behaviour of the system.** As the next step after the demonstration of the proof of concept of electrochromic self-powered sensors, the theoretical basis of these type of sensors were established. The combination of a software based on finite element methods with experimental data allowed the development of a reliable model that was used not only to have a complete understanding of the device, but also as a design tool for future electrochromic devices.
- **Two electrochromic Prussian Blue screen-printing pastes were formulated.** The coating of conducting tin oxide particles with Prussian Blue allows enables the manufacture of electrochromic screen-printing pastes that were used to fabricate electrodes with a high spectroelectrochemical performance. The use of these pastes to construct Prussian Blue electrodes removes the need for transparent electrodes, facilitating the mass production of electrochromic devices.
- **A fully printed self-powered electrochromic sensor was fabricated.** The substitution of the electrodeposited display on a transparent electrode by an electrochromic paste led to simplification of the electrochromic sensor construction. Moreover, an ionic liquid-based gel polymer printed on top of the display can be used as electrolyte, leading to a truly fully printed analytical device. The transition from the initial prototype to the final printed device brings about certain changes on the analytical performance observed. Figure 7.1 summarizes the most important aspects related to this performance.







| | | | |
|---|---|---|---|
|  |  |  | |
| Display | Screen-printed PB on Au | Screen-printed PB on Au | PB electrodeposited on ITO-Glass |
| Electrolyte | Ionic liquid gel polymer | Aqueous | Aqueous |
| Sample type | Coloured/colourless | Colourless | Colourless |
| Response time | 300 s | 90 s | 30 s |
| Display affected by interferences | No | Yes | Yes |
| Colour switch |  |  |  |

Figure 7.1: Schematic summary of the electrochromic devices developed in this thesis.

7.2 Outlook

The devices presented in this thesis allow to develop self-powered sensors in which an electrochromic display, that also acts as a power source, is capable of providing a naked eye quantitative readout of the concentration of the analyte in the sample in the form of a metering bar. As explained previously, the readout of the converted distance of the electrochromic display is done after a fixed time. Part of the current and future work aims at finding possible ways to overcome this time-dependence, but also aims at regenerating the electrochromic display after each measurement, so that real-time measurements are enabled.

Since Prussian Blue undergoes a reversible redox reaction, one way to achieve a more dynamic device is to couple a second enzymatic system opposite to the glucose biosensor. This second electrode would also be connected to the electrochromic display, leading to a system with two electrochemical cells, as depicted in Figure 7.2, and differing from the conventional bipolar architectures where the electrochromic display is “floating” between the other two electrodes.¹ The second enzymatic reaction would oxidize the Prussian White formed by the glucose reaction back to Prussian Blue. A suitable enzymatic reaction could be the reduction of oxygen (Figure 7.2).

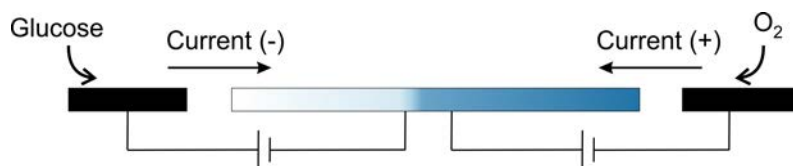


Figure 7.2: Schematic representation of the two enzymatic biosensors connected to the electrochromic display.

In the field of enzymatic fuel cells, so-called “air-breathing cathodes”² are widely spread. These utilize the oxygen in the air to trigger the enzymatic reaction at the anode at higher rates. Air-breathing cathodes not only allow to have a system where the oxygen is present in a larger concentration than in an aqueous system, but they also display a constant enzymatic rate as the amount of oxygen in the surroundings of the electrode remains essentially constant. These air-breathing cathodes normally rely on the use of an enzyme such as bilirubin oxidase (BOD), and a redox polymer mediator similar to the Os-PVI₁₅ used in Chapter 5, but in this case, with a higher formal potential.³

If the two enzymatic reactions are simultaneously connected to the electrochromic display, the resulting device would be a combination of two electrochemical cells, with the following redox systems:

At the glucose biosensor (anode):



at the oxygen sensor (cathode):



and at the electrochromic display (bipolar electrode):



where Med_1 represents a low-potential redox mediator, and Med_2 a high-potential redox mediator. The first cell (eq. 7.1 and eq. 7.3) is similar to that explained throughout this thesis where the glucose biosensor acts as the anode, and the displays acts as the cathode. The second cell (eq. 7.2 and eq. 7.3) would comprise the oxygen biosensor acting as cathode, and the electrochromic display acting this time as the anode.

When the two electrochemical cells are simultaneously connected to the PB electrode, two opposed reactions take place at the display. On the one hand, the electric current generated by the glucose biosensor gradually converts Prussian Blue into Prussian White; and, on the other hand, the current flowing from the oxygen biosensor does the opposite, converting PW back into PB. This way, the conversion rate of both reactions will be equal at some point, and an equilibrium state will be reach in which the electrochromic display stops its motion. This behaviour was confirmed with mathematical simulations. For simplification, the oxygen biosensor was implemented with the same kinetic constants than that of the glucose biosensor in Chapter 4. The potentials of the redox mediators were shifted to -0.3 V for the case of Med_1 and to 0.5 V for the Med_2 to observe a better defined and faster colour switch. The concentration of glucose was set at 10 mM and that of oxygen was fixed inside the saturation range of the biosensor, at 15 mM , as seen in Figure 4.7. This concentration is much higher than the actual concentration of oxygen in air.⁴ However, the value of 15 mM was selected in agreement with the simulated biosensor. As shown in Figure 7.3, the advance of the colour conversion slowly decreases, and, after approximately 3 minutes, it eventually stops.

The use of an air-breathing cathode allows to observe a constant enzymatic reaction rate since the concentration of oxygen in air is relatively high and constant (non-limiting). However, the concentration of the analyte at the first biosensor, i.e. glucose, will vary depending on the sample, and thus the rate of the enzymatic reaction. This leads to different

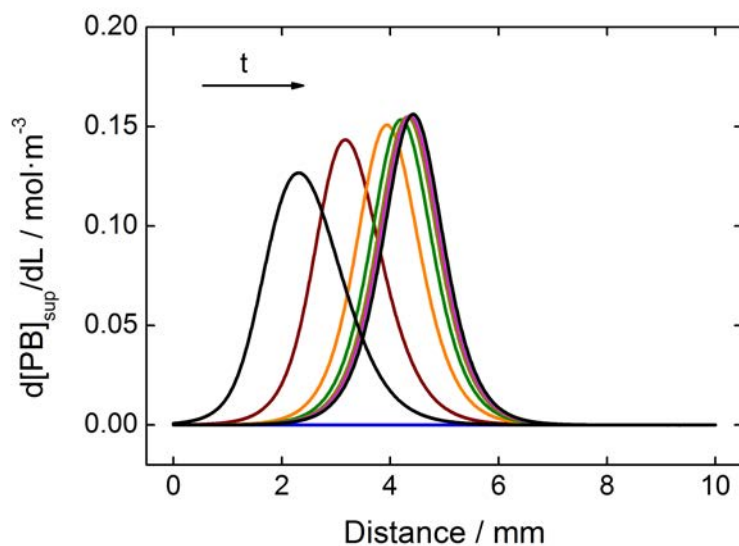


Figure 7.3: Plot of the derivative of the PB concentration at the surface of the display against the distance converted for increasing reaction times ranging from 15 to 210 seconds.

rates of conversion at the electrochromic display. When the glucose loading is low, the distance advanced when the PB-PW systems reaches its equilibrium is shorter than when the amount of glucose is higher, which can be used to obtain a calibration curve (Figure 7.4).

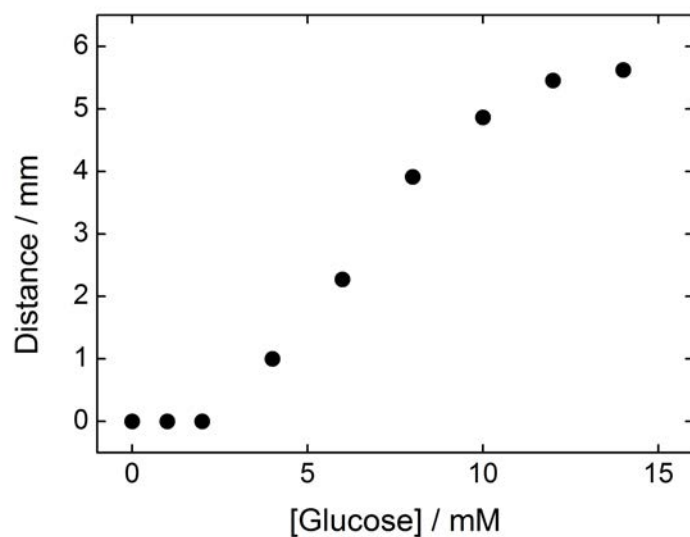


Figure 7.4: Calibration curve obtained for two-cell self-powered system. The measuring time was set at 180s.

Preliminary tests were carried out to experimentally validate this modelled system.

For this, a coplanar three-electrode device similar to that of Chapter 6 was used. A bipotentiostat was used to apply constant fixed potentials of opposite sign from both unmodified carbon electrodes to the PB electrode, thus simulating a two-cell system. Different experiments were carried out keeping a positive potential of 1.6 V constant in all the measurements to simulate the constant conversion rate due to the oxygen sensor, and the negative applied potential from the other electrode was varied to simulate the behaviour of the glucose biosensor with samples of different concentrations. The absence of a charge balance layer at the anode (glucose biosensor) and at the cathode (O_2 biosensor), makes it necessary to apply higher potentials to observe the colour conversion. Figure 7.5 shows image captures of the experiments with different applied potentials after 90 seconds. After that time, the display reaches an equilibrium state, as predicted by the mathematical simulations, and the motion of the colour front stops. As observed, the amount of PB converted to PW is related to the applied potential, indicating that a direct correlation between the converted distance and the amount of glucose in the sample may be possible.

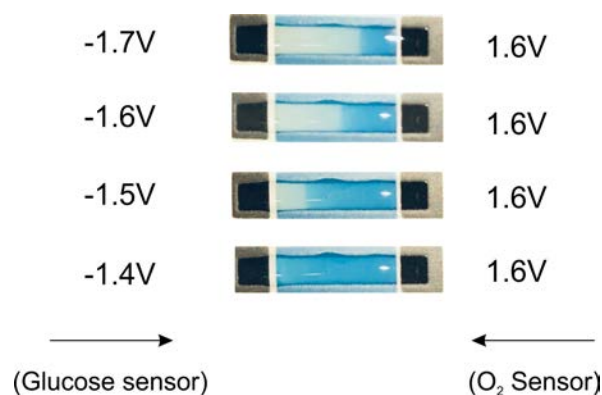


Figure 7.5: Potentiometric experiments carried out in an aqueous supporting electrolyte. Two electric potentials of different sign were applied simultaneously from each of the unmodified carbon electrodes. PB display was used both as auxiliary and reference electrode

The experiments as well as the mathematical simulations show that the use of a second coplanar biosensor can be a promising tool not only to regenerate the electrochromic display after each measurement, but also to obtain a real-time readout of the analyte concentration, which eventually allows to have a self-powered instrumentation-less device for continuous monitoring of analytes.

Bibliography

- [1] Fosdick, S. E.; Knust, K. N.; Scida, K.; Crooks, R. M. Bipolar electrochemistry. *Angew. Chem. Int. Ed.* **2013**, *52*, 10438–10456.
- [2] Mano, N.; de Poulpiquet, A. O₂ reduction in enzymatic biofuel cells. *Chem. Rev.* **2018**, *118*, 2392–2468.
- [3] Mano, N.; Heller, A. A miniature membraneless biofuel cell operating at 0.36 V under physiological conditions. *J. Electrochem. Soc.* **2003**, *150*, A1136–A1138.
- [4] Jayashree, R. S.; Gancs, L.; Choban, E. R.; Primak, A.; Natarajan, D.; Markoski, L. J.; Kenis, P. J. A. Air-breathing laminar flow-based microfluidic fuel cell. *J. Am. Chem. Soc.* **2005**, *127*, 16758–16759.

List of publications

Publications included in this thesis

Articles

- **Pellitero, M.A.**, Kitsara, M., Eibensteiner, F., del Campo, F.J.; *Rapid prototyping of electrochemical lateral flow devices: stencilled electrodes*, *Analyst*, 2016, 141, 2515–2522.
- **Pellitero, M.A.**, Guimerà, A., Kitsara, M., Villa, R., Rubio, C., Lakard, B., Douche, M-L., Hihn, J-Y., del Campo, F.J.; *Quantitative self-powered electrochromic biosensors*, *Chemical Science*, 2017, 8, 1995–2002.
- **Pellitero, M.A.**, Guimerà, A., Villa, R., del Campo, F.J.; *iR Drop Effects in Self-Powered and Electrochromic Biosensors*, *Journal of Physical Chemistry C*, 2018, 122, 2596–2607.
- **Pellitero, M.A.**, Colina, Á., Villa, R., del Campo, F.J.; *Antimony tin oxide (ATO) screen-printed electrodes and their application to spectroelectrochemistry*, *Electrochemistry Communications*, 2018, 93, 123–127.
- **Pellitero, M.A.**, del Campo, F.J.; *Electrochromic sensors: innovative devices enabled by spectroelectrochemical methods*, *Current Opinion in Electrochemistry*, DOI:10.1016/j.coelec.2019.03.004, 2019.
- **Pellitero, M.A.**, Fremeau, J., Villa, R., Lakard, B., Hihn, J-Y., del Campo, F.J.; *Electrochromic biosensors based on screen-printed Prussian Blue electrodes*, *Sensors and Actuators B: Chemical*, 2019,...

Patents

- del Campo, F.J., Guimerà-Brunet, A., Kitsara, M., **Pellitero, M.A.**; *Electrochromic biosensor*, Patent application number: WO20170908076A1.

Publications not included in this thesis

Articles

- Kitsara, M., Cirera, J.M., **Aller-Pellitero, M.**, Sabaté, N., Punter, J., Colomer-Farrarons, J., Miribel-Català, P., del Campo, F.J.; *Small-volume multiparametric electrochemical detection at low cost polymeric devices featuring nanoelectrodes*, Progress in Biomedical Optics and Imaging - Proceeding of SPIE, 2015, 9581, 95180Z, 1–8.
- Punter-Villagrasa, J., Paez-Aviles, C., Colomer-Farrarons, J., Lopez-Sanchez, J., Juanola-Feliu, E., Miribel-Català, P., Kitsara, M., **Aller-Pellitero, M.**, del Campo, F.J.; *A low-power electronic instrumentation for multi-parametric diabetes mellitus analysis*, IECON Proceeding, 2016, 5211–5215.
- Ruiz-Vega, G., Kitsara, M., **Pellitero, M.A.**, Baldrich, E., del Campo, F.J.; *Electrochemical Lateral Flow Devices: Towards Rapid Immunomagnetic Assays*, ChemElectroChem, 2017, 4, 880–889.

Patents

- del Campo, F.J., **Pellitero, M.A.**, Dei, M., Guimerà-Brunet, A.; *Biosensor inalámbrico, portátil y reutilizable*, Patent application number: P201930187.

Book chapters

- Punter-Villagrasa, J., Colomer-Farrarons, J., del Campo, F.J., Miribel-Català, P.; *Electrochemical biosensors*, in **Amperometric and Impedance Monitoring Systems for Biomedical Applications**, Springer, 2017, ISBN: 978-3-319-64801-9.
- Punter-Villagrasa, J., Colomer-Farrarons, J., del Campo, F.J., Miribel-Català, P.; *Electrochemical DC techniques. Glucose monitoring and multiparametric detection*, in **Amperometric and Impedance Monitoring Systems for Biomedical Applications**, Springer, 2017, ISBN: 978-3-319-64801-9.

Annex 1: Analysis of grey scale colour profiles

In the colorimetric experiments of Chapter 3, the colour change of the electrodeposited Prussian Blue layer was analyzed, and images were taken after a fixed time of 30 seconds. Image processing software ImageJ was used to obtain colour profiles of the captured images, which allowed to determine more accurately the length of the PB strip affected by the colour change. The obtained images were transformed into a grey colour scale, and a profile of the white colour intensity along the electrochromic display was extracted, as seen in Figure 7.6. The position of the colour front was determined by the intercept of the two straight lines fitting the region where the discolouration begins and the baseline region where no discolouration is observed (Figure 7.6).

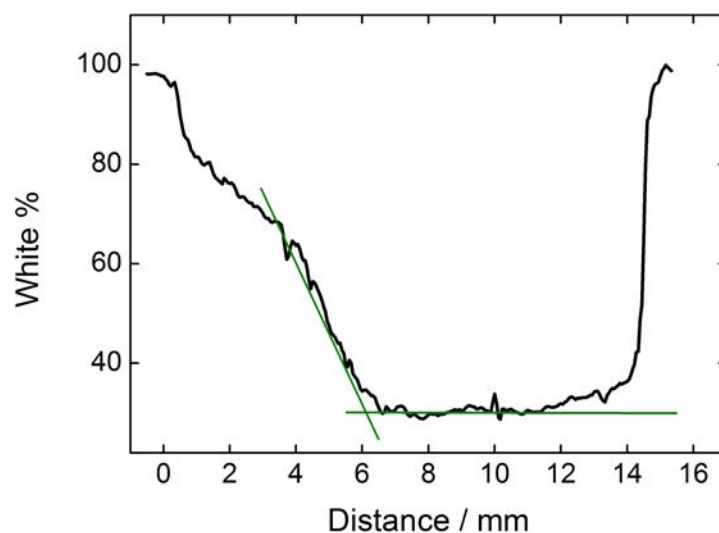


Figure 7.6: Colour profile from a captured image of the display for a constant applied current of 16 μA .

Annex 2: RGB scale analysis

According to the RGB colour model, the colours observed in the visible spectra result from the composition of the primary colours red, green, and blue.¹ In this model, any given colour can be described by the sum of three values, corresponding to the colour intensities of each primary colour (Figure 7.7A), in a scale ranging from 0 to 255. Thus, any colour is defined by the values of the RGB components separately, as depicted in Figure 7.7B.

As inferred from Figure 7.7, the switch from the blue colour of Prussian Blue to the colourless/white colour of Prussian White, occurs by a variation in the red and green components, while the blue component remains essentially unaltered.

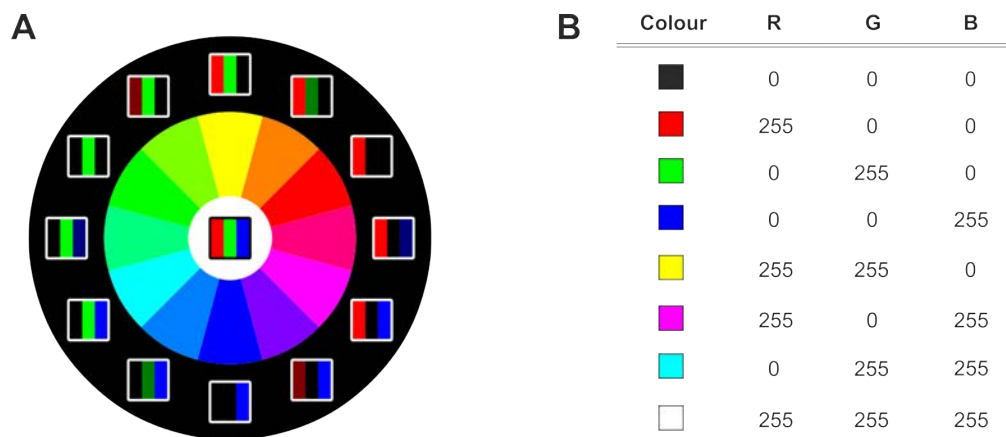


Figure 7.7: (A) RGB colour wheel showing the possible combinations of the red, green, and blue colours and the perceived colour. (B) Combinations of some RGB values and their resulting colour.

The conventional image analysis provides one measurement value in the grey scale,² as those used in Chapter 3. An increase in the sensitivity of the analysis can be achieved by separating the three RGB components of the image and analyzing only one of them. The observed blue colour of the electrochromic displays is mainly due to the blue and green components of the RGB spectrum, while the white colour of the switched display is due to all three components. This means that the analysis of the red component should bring about the highest degree of sensitivity. Indeed, this was observed when analyzing the electrochromic displays in Chapter 6. Figure 7.8 shows the grey and RGB profiles of an

image of an actual device along a straight line. In both cases, the minimum and maximum values of 0 and 255 represent the black and white colour, corresponding to the carbon electrodes and the PET substrate, respectively. By looking at the profiles in the region of the display, it can be observed a slope corresponding to the colour conversion of Prussian Blue. Since the blue component of both PB and PW remains unaltered, a plain profile is observed. A slight conversion in the green component can be seen on its profile, very similar to the conversion in the grey scale of Figure 7.8A. However, the red component is the most sensitive of the three, leading to a remarkable conversion at the display. This implies that, to improve the sensitivity of the analysis, it is highly recommended to do it based on the evolution of the red component of the colour. Nevertheless, an analysis based on the grey scale may also be suitable, as demonstrated in the grey scale profiles of Chapter 3.

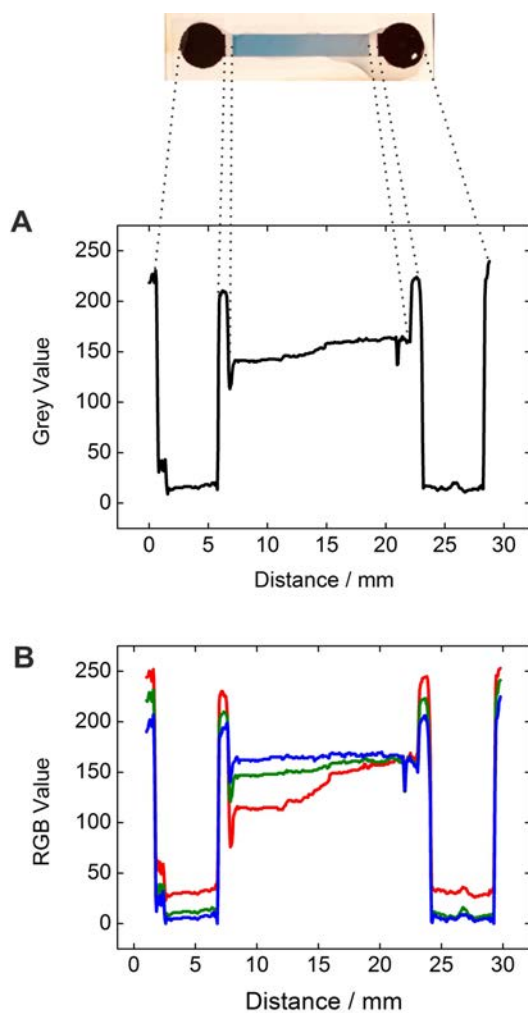


Figure 7.8: Image of an actual display during a glucose measurement. (A) Grey scale profile. (B) RGB scale profiles showing the values for the corresponding component: R (red line), G (green line), and B (blue line).

Bibliography

[1] www.colorizer.org.

[2] Prats-Montalbán, J. M.; de Juan, A.; Ferrer, A. Multivariate image analysis: A review with applications. *Chemom. Intell. Lab. Syst.* **2011**, *107*, 1–23.